THE UNIVERSITY *of* EDINBURGH

Implementation of Angular Diversity Receiver for VLC-IoT Sensor Networks

RYO HARADA

A thesis submitted for the degree of Doctor of Philosophy

The University of Edinburgh

September 2025

To my wife and my daughters,

My dearest wife, Saori Harada, always gives me unwavering support and love. I am grateful for the efforts she made for me and our precious daughters, Risa and Yuzuki. My daughters waited for me until this journey ended, despite being lonely without me as their father. They are my greatest joy and my motivation; I hope this achievement inspires them to pursue their own dreams with passion and determination. This thesis is dedicated to you with all my heart.

Abstract

The demand for wireless spectrum is increasing, leading to radio frequency (RF) congestion. As wireless technologies advance and applications such as smart cars, e-health, smart grids, and the Internet of Things (IoT) proliferate, the problem intensifies. Visible light communication (VLC) systems are suggested as a solution, offering a large unlicensed spectrum ideal for radio-sensitive environments such as hospitals and aircrafts. However, a significant challenge for VLC implementation is achieving wide communication coverage due to a limited field of view (FOV). This thesis aims to explore and develop methods to enhance communication coverage in VLC-based IoT (VLC-IoT) systems.

The thesis first analyses the performance of angular diversity receiver (ADR) configurations in indoor multi-cell VLC scenarios, focussing on square pyramid (SP), square frustum (SF), hexagonal pyramid (HP), and hexagonal frustum (HF) shapes. Through numerical and simulation analysis, performance is assessed using spatial multiplexing (SMP) and receive diversity techniques, including selection combining (SC), equal gain combining (EGC), and maximum ratio combining (MRC). The results from SMP applications indicate that the HF ADR provides the widest coverage for multi-stream transmission due to its largest number of photodiodes (PDs). However, for receive diversity, the HP and HF configurations with six sides PDs do not outperform the SP and SF types with four PDs, one on each side in terms of bit error rates (BERs) performance when using SC.

Subsequently, this thesis analyses the performance of ADR systems in single-cell VLC scenario and proposes a novel ADR system in IoT sensor networks. The numerical analysis applying the combining techniques indicates that any combination of ADR types and diversity techniques can enhance performance. Therefore, a SF ADR is implemented with the EGC due to the low complexity. The proposed ADR system enhanced received signal-to-noise ratio (SNR), improved BERs, and provided more than double the coverage of the link. Furthermore, the effectiveness of the system is demonstrated with real-time sensor transmission and a duplex VLC communication link, showcasing its advantages in practical IoT applications.

Following that, the integrated VLC and RF (VLC-RF) system using the ADR for secure industrial IoT applications is presented. The prototype with the custom-built ADR and analogue front end (AFE) is connected to the backbone network such as a wireless cloud server. As the fundamental VLC performance, SNR, secrecy capacity (SeCap) and BER coverage is measured. The result indicates that the prototype has better physical layer security (PLS) performance than the single PD receiver, and the coverage of the link is drastically expanded compared to the initial design. Furthermore, to evaluate the feasibility of the IoT application, real-time sensor network applications are demonstrated using the proposed integrated VLC-RF ADR system. These experiments, including real-time sensor transmission, image transmission, and integration of the robot arm system, indicate the benefits in a practical scenario by showing low latency.

Finally, the wavelength division multiplexing (WDM) based VLC prototype using the colour PDs is implemented. This is an additional experimental study to show the method for ADR

based multiplexing system. The BERs performance of three different wavelength channels (red, green, blue) is shown in comparison with the single PD receiver. The result shows that WDM can be possible using the colour PD and the ADR WDM system enhances SNR and communication range.

Lay Summary

The vast need for wireless spectrum has caused severe radio frequency (RF) congestion in recent years. Furthermore, it is predicted that by 2030 there will be around 500 billion Internet of Things (IoT) devices connected over the Internet, making problems worse. To address such high needs, visible light communications (VLCs) can be one of the possible solutions to alter or complement conventional wireless communications by realising light fidelity (Li-Fi) connectivity in radio-sensitive environments such as hospitals and aeroplanes. VLC systems have been considered in different applications including indoor Li-Fi systems and the IoT. However, to realise the implementation of VLC, there are still several challenges that need to be addressed to improve communication coverage due to the narrow field of view (FOV).

An angular diversity receiver (ADR) can be a promising solution to the limitation of communication coverage. The ADR has multiple photodiodes (PDs), one on each side, directed at different angles, making the synthesised FOV larger than that of the single PD. The objective of this thesis is to analyse and propose the ADR for a VLC system with wide coverage. The method is based on analytical and experimental studies for the verification of the proposed ADR system. In experimental studies, communication performances such as data rate, coverage, latency, and security are measured in industrial IoT scenarios. This thesis indicates the optimal ADR configuration and the design of the proposed ADR for implementation. This result shows the feasibility of the proposed system for real-time IoT sensor networks.

Declaration of Originality

I declare that this thesis has been composed solely by myself, that the work contained herein is my own except where explicitly stated otherwise by reference or acknowledgement, and that this work has not been submitted for any other degree or professional qualification except as specified.

Ryo Harada
Edinburgh, Scotland, The United Kingdom
September 30, 2025

Acknowledgements

This research was funded by the Acquisition, Technology and Logistics Agency (ATLA), Ministry of Defence (MOD), Japan. Without their financial support, I could never have had such an opportunity to pursue my Ph.D. degree.

I am very grateful to the ATLA personnel who helped me during my research. The personnel in the General Affairs Section of the Future Capability Development Centre (FCDC) supported me during my study. Colleagues in the Information and Communication Research Division alternated my work while I was away for this training programme. I really appreciated that the Director of FCDC, Yamaoka, referred me to this precious opportunity for the selection of candidates by the ATLA headquarter. My boss in the C4I Systems Section and the Communication Network Research Section, Ninomiya and Nakagawa, provided substantial assistance by offering extensive advice on course preparation and ensured that no problems arise during my studies. My current boss in the Communication Network Research Section, Sonoda, took care of me to finish this thesis regardless of my duty. All the support I received from them made this long and difficult journey possible.

I would like to express my sincere gratitude for the completion of this thesis, which is the culmination of my extensive postgraduate studies at the Institute for Imaging, Data, and Communications (IDCOM), School of Engineering, The University of Edinburgh. My supervisor, Professor Wasiu Popoola, guided me throughout the course of this journey. Without his reasonable feedback and advice, I could not have completed this thesis. In addition, he always asks me about not only me, but also my family. He took his time to ensure me that I would not have any problem. I would like to thank the engineering technicians in the teaching laboratory of the School of Engineering. They gave me many supports on the analogue circuits design, printed circuit board manufacturing.

I also would like to thank the members of the research group, Callum Geldard, Tilahun Gutema, Ahmet Burak Ozyurt, Jianhui Chen, Jian Shao and Minqing Yu. I had a great time with them during the Ph.D. study. Callum helped me complete the analysis part of this thesis by providing advice throughout the review process of my paper. All members supported every aspect of my accomplished work, including analysis and experimental work. Also, I never had time with sadness after work and enjoyed Edinburgh night with them, which is a great memory of my life in Edinburgh.

Contents

List of Figures

List of Tables

List of Abbreviations

5G	5th Generation
6G	6th Generation
ACK	acknowledgement
ADC	analogue-to-digital converter
ADR	angular diversity receiver
AFE	analogue front end
AGC	automatic gain control
amp	amplifier
AP	access point
APD	avalanche PD
APP	application
AWGN	additive white Gaussian noise
BBB	Beagle Bone Black
BER	bit error rate
CAP	carrier-less amplitude and phase modulation
CCI	co-channel interference
CSI	channel state information
DAC	digital-to-analogue converter
DL	downlink
DLL	data link layer
DPIM	digital pulse interval modulation
ED	eavesdropper
EGC	equal gain combining
EMI	electromagnetic interference

FEC	forward error correction
FET	field effect transistor
FOV	field of view
FPGA	field programmable gate array
FSK	frequency shift keying
FSO	free space optical communication
HF	hexagonal frustum
HP	hexagonal pyramid
HPF	high pass filter
ICI	inter-cell interference
IEEE	Institute of Electrical and Electronics Engineers
IM/DD	intensity modulation and direct detection
IoT	Internet of Things
IR	infrared
ITS	intelligent transportation systems
ITU-T	International Telecommunication Union Telecommunication Standardization Sector
LD	laser diode
LED	light emitting diode
Li-Fi	light fidelity
LOS	line-of-sight
LPF	low pass filter
LS	least squares
MAC	media access control
MC	Monte Carlo
MCU	microcontroller unit
MIMO	multiple-input multiple-output
ML	maximum likelihood

Mod	modulator
MQTT	message queue telemetry transport
MRC	maximum ratio combining
NLOS	non-line-of-sight
NRZ-OOK	non-return-to-zero on-off keying (OOK)
OFDM	orthogonal frequency division multiplexing
OOK	on-off keying
op-amp	operational amplifier
OWC	optical wireless communication
PCB	printed circuit board
PD	photodiode
PER	packet error rate
PHY	physical layer
PLS	physical layer security
QoS	quality of service
RF	radio frequency
RGB	red, green and blue
RIS	reconfigurable intelligent surface
RTT	round-trip time
Rx	receiver
SC	selection combining
SeCap	secrecy capacity
SF	square frustum
SINR	signal-to-interference-plus-noise ratio
SMD	surface mount device
SMP	spatial multiplexing
SNR	signal-to-noise ratio
SP	square pyramid

TIA	transimpedance amplifier
TP	transport
Tx	transmitter
UART	universal asynchronous receiver/transmitter
UL	uplink
UN	user node
UV	ultraviolet
VLC	visible light communication
VLC-IoT	VLC-based IoT
VLC-MIMO	VLC-based multiple-input multiple-output (MIMO)
VLC-RF	VLC and RF
WAN	wide area network
WDM	wavelength division multiplexing
WDMA	wavelength division multiple access
Wi-Fi	wireless fidelity
ZF	zero-forcing

List of Mathematical Symbols

α_{jk}	Angle between a normal vector of k, n_k
β_{ik}	Angle between vectors of k to LED$_j$ and PD$_i$
Γ	FET channel noise factor
γ	Signal-to-Interference-plus-Noise Ratio (SINR)
δ_{R}	ADR rotation angle
δ_{tilt}	Tilt angle
η	PD fixed capacitance per unit area
θ_{ij}	Incident angle
θ_{ik}	Incident angle by reflection
ρ_{k}	Reflective coefficient
σ_n^2	Noise variance
σ_{shot}^2	Variance of shot noise
$\sigma_{\mathrm{thermal}}^2$	Variance of thermal noise
ϕ_{ij}	Emission angle
$\Phi_{1/2}$	Semi-angle of LED at half power
φ_{jk}	Emission angle by reflection
Ψ	Field of View (FOV)
$\Psi_{1/2}$	Half angle of FOV
A	Active area of photodiode (PD)
A_{r}	Reflective area
B_{n}	Equivalent noise bandwidth
b_m	Possible m bit
C_{PD}	Capacitance of PD
C_{T}	Total capacitance
D	Delay
d_{ij}	Distance between LED$_j$ and PD$_i$
$\mathrm{d_H}()$	Hamming distance
$f_{-3\mathrm{dB}}$	Theoretical -3 dB bandwidth
G	Open-loop gain

g_{m}	FET transconductance
H_{l}	Channel gain of a point-to-point communication link
$\mathbf{H}$	Channel matrix
$\hat{H}$	Estimated channel matrix
I_2	Noise bandwidth factor
I_{bg}	Background noise current
K	Number of reflections
k	Reflective point
k_{B}	Boltzmann constant
m	Order of Lambertian emission
$\mathbf{N}$	Noise vector
N_0	Noise power spectral density
N_{r}	Number of PDs
N_{t}	Number of LEDs
$\mathbf{P}$	Matrix of a pilot sequence
P_j	Total optical power received
P_{o}	Normalised optical power
P_{t}	Average transmitted optical power
$Q(.)$	Gaussian Q function
q	Charge of an electron
$\mathcal{R}$	Responsivity of photodiode (PD)
R_{coverage}	Coverage rate
R_{Load}	Load resistor
s	Number of pilot bits
T	Absolute temperature
T_{s}	Symbol duration
V_{pp}	Peak-to-peak voltage
W	Weight matrix
W_j	j_{th} row of weight matrix
x	Electrical signal
$\hat{x}$	Detected signals
x_n	Time domain digital signal
X	Electrical signal vector

$\mathbf{X}_m$	Signal vector
$\boldsymbol{Y}$	Received signal vector
$\mathbf{Y}_{\mathrm{p}}$	Pilot sequences received
$\ln(\cdot)$	Natural logarithm
$\|.\|$	Norm
$[.]^T$	Transpose
$\langle . \rangle$	Dot product

Chapter 1
Introduction

Advancements in wireless technologies have resulted in a wider range of use cases such as smart cars, e-health, smart grids, and the Internet of Things (IoT). This society change requires a broad bandwidth of the radio frequency (RF) spectrum to provide wireless connectivity. The growing demand for more bandwidth in the wireless spectrum has caused RF congestion in recent years. According to a projection, around 500 billion IoT devices will be connected online by 2030 [1]. Furthermore, a recent trend will further increase the spectrum congestion [2]. Therefore, a higher frequency spectrum is considered for mobile communication systems such as 5th Generation (5G) and beyond 5G to obtain a wider bandwidth using millimetre and terahertz waves. The evolution of communication technologies enabled devices to connect to the Internet through IoT.

Visible light communication (VLC) has been considered to address the growing demand for bandwidth. It could deliver a broad unlicensed spectrum in the optical domain. VLC is particularly advantageous in environments sensitive to radio frequencies, such as hospitals and manufacturing facilities, and can also help ease the high pressure on the RF spectrum [3]. Consequently, VLC systems are expected to serve as a complement to current RF systems. In addition to communication, visible light technology can be applied to other applications, such as positioning systems or sensing [4]. Furthermore, due to its inherent security, which stems from characteristics like line-of-sight (LOS) propagation, there is growing research interest in evaluating the physical layer security (PLS) of VLC, particularly with respect to the risk of eavesdropper (ED) [5].

IoT has attracted industrial contexts that require more complex operations than consumer IoT applications. IoT systems provide various use cases as industrial IoT, including remote monitoring, item tracking, safety management, operational agility, industrial automation, predictive maintenance [6]. Challenges for the application of VLC-based IoT (VLC-IoT) in industrial environments include link distance, attenuation of signals by air particles, multipath reflections, and loss and blockage of signals [7]. Although some of them are similar in consumer IoT ap-

plications, such as smart appliances, they have a higher requirement due to harsh environments. However, there have been limited experimental studies that consider industrial IoT scenarios.

VLC has been considered for IoT applications in previous studies that include [8–12]. In VLC-IoT, bidirectional communication is established between access points (APs) and user nodes (UNs) through optical links to control IoT devices and obtain sensor data. An essential role for AP is to coordinate with the backbone network, wide area network (WAN), to store data on cloud servers [13]. RF techniques such as wireless fidelity (Wi-Fi) are typically applied to interact with the IoT cloud server on WAN and transmit the data collected from each UN through APs. The conventional RF system can also improve the robustness of VLC-IoT through hybrid connectivity [8]. In [14], the integration of VLC with RF has been experimentally investigated, highlighting the potential of VLC as a complement to RF technologies. Typically, IoT APs regularly collect and store sensor information and handle data requests from UNs. When a UN sends a request, the AP transmits sensor data, such as temperature and humidity, to the UN. To demonstrate VLC-IoT, experimental verifications of prototypes for IoT applications have previously been shown in [15, 16]. To establish an uplink (UL) and a downlink (DL) for the IoT sensor networks, both the AP and the UN must be designed as transceivers. The bidirectional VLC system in [15] utilises VLC for DL and infrared (IR) for UL to reduce interference with each other. The UN as an IoT device needs to be low-cost, low power consumption, and compact. Therefore, microcontroller units (MCUs) are usually used for implementation due to their low cost and small form factor. The communication techniques applied in MCUs must be low in complexity due to limited resources.

Although VLC has significant advantages, there are still gaps to reach practical application. Much of the related work has focused on improving the data rate of a unidirectional point-to-point VLC without considering the coverage of communication. These previous works focused on static setups because of the precise alignment. In addition, many VLC studies, based on an offline setup, have not been designed for resources-constrained platforms, such as MCUs with limited electrical and computing power. To fill the gap from previous work, experimental verification is needed in real-time and practical scenarios. However, there have been limited works that focus on availability in terms of communication coverage and real-time implementation. Furthermore, the system-level demonstration in VLC-IoT has not been thoroughly considered in the literature.

1.1 Motivation and Scope

One of the key challenges in the implementation of a VLC system is obtaining availability in mobile applications and providing wide coverage to alleviate the effect of misalignment. A viable solution to this challenge is to use a photodiode (PD) with a wide field of view (FOV) or reconfigurable intelligent surfaces (RISs). In [17], RISs can provide wide coverage by reconfiguring the incident angle with reflective elements. Although the RIS technique could help provide a broad coverage by controlling reflected light, the RIS requires instalments in the appropriate places, which makes usability limited. It is also essential that a VLC receiver itself has resiliency against misalignment. Hence, in this thesis, the achievement of wide coverage in VLC systems is focused without any support from the outside environment, such as the RIS.

As a solution to provide wide communication coverage, an angular diversity receiver (ADR), composed of multiple PDs pointing in different directions, has been proposed for VLC systems [18–27]. The ADR can be compact, making it suitable for mobile use cases through multiple-input multiple-output (MIMO) channels. The communication coverage can be broad with the ADR due to its effective wide FOV. Thus, the ADR can mitigate alignment limitations, although it still suffers LOS disconnection due to blockage. For user adoption, the impact of the deployment increases depending on the number of PDs, although the size of analogue front end (AFE) can be the same as the conventional single PD receiver. Several different ADR configurations have been considered in previous work, including pyramidal shape and frustum shape. However, to the best of the author's knowledge, the performance comparison of these ADR types with different numbers of PDs has not been considered in the literature. In addition, few studies have focused on experimental verification through prototyping beyond analytical research.

This thesis focusses on implementing a VLC prototype with the custom-built ADR. In Chapter 3, performance with different ADR types, applying spatial multiplexing (SMP) and receive diversity techniques, is compared and analysed through simulation and numerical studies in multi-cell scenarios. Chapter 4 continues the analytical work for single-cell scenarios to explore the optimum ADR type for the following prototyping, then the suitable ADR type is selected to design the VLC-IoT system for experimental verification. In addition, in Chapter 5, the prototype is expanded to a full-scale integrated VLC and RF (VLC-RF) system for secure industrial IoT applications. The additional experimental work in Chapter 6 improves the ADR system by applying the wavelength division multiplexing (WDM) technique using red, green

and blue (RGB) colour PDs. This work shows the availability of multiplexing and multi-access networks. With these achievements in each chapter, it is possible to convince the feasibility of the VLC-IoT system with the designed ADR.

1.2 Aims and Objectives

The thesis aims to analyse ADR techniques and develop the VLC prototype to enhance communication performance such as coverage. The suitable ADR technique for implementation will be analysed by theoretical analysis and simulations, and the VLC prototype with the optimum ADR will be developed through experimental means including prototyping and implementation. The VLC prototype will be evaluated using basic performance metrics such as signal-to-noise ratio (SNR), bit error rate (BER), secrecy capacity (SeCap) and coverage rate. The effectiveness of the VLC prototype will be demonstrated in practical IoT scenarios, showing latency such as response time, round-trip time (RTT) and one-way latency. To accomplish these objectives, specific goals are set as follows:

- Review the literature including analytical and empirical studies and evaluate cutting-edge VLC techniques in terms of ADR-based system implemented in IoT applications to understand the research gap towards realising the implementation in real time.
- Compare and analyse the different configurations of the ADR shape through numerical analysis and simulations. This includes investigating related techniques such as MIMO techniques, SMP, and receive diversity. By evaluating these performances of SNR and BER, the suitable ADR type is explored for the following experimental verifications.
- Design the prototype of the VLC-IoT system that includes the AFE, ADR model, and printed circuit boards (PCBs). Based on the design, the prototype is developed and implemented for MCU operation, as well as to produce programming codes. Then, experimental setups are built to measure the prototype performances of SNR, BER, and coverage rate. These results are compared to the single PD receiver to show the degree of performance enhancement.
- Expand the VLC-IoT prototype into an integrated VLC-RF system for verification of the expanded scope of the prototype. The receiver AFE design is modified to improve performance. In addition, the improved design equips the RF function for robustness

by hybrid use of VLC and RF. This RF connectivity also interacts with the WAN, the background core network. This design enables full-scale verification of the VLC system. Based on the novel design, AFEs and PCBs are developed and implemented with programming codes for the MCU, RF module, and IoT server. Then, experimental setups are built to measure fundamental performance, including PLS and system performance, such as response time. The prototype is evaluated in practical industrial IoT scenarios with measured latency.

- To further show the ADR capability of implementation with higher data rate, the proposed ADR system is applied with the WDM technique by RGB colour PD. With the prototype in the same MCU operation, it is evaluated by analysing signal-to-interference-plus-noise ratio (SINR) and BER. These results indicate the feasibility of WDM in the ADR system, and the proposed system can be applied to the multi-access network by wavelength division multiple access (WDMA).

1.3 Thesis Contributions

This thesis has made significant original contributions to the field of ADR techniques and VLC implementation through the following achievements:

1. Comparison and analysis of the performance of VLC using four ADR configurations, including pyramid and frustum types, that are commonly used in previous work. These ADR configurations have different numbers of PDs from four to seven: square pyramid (SP), square frustum (SF), hexagonal pyramid (HP), and hexagonal frustum (HF). In the SMP application, signal detection techniques are compared in terms of BER performances. The multi-stream coverage rate using maximum likelihood (ML) is analysed in the indoor MIMO scenario. The BER is investigated through simulation and analytical studies, whilst the coverage is explored with estimated channel state information (CSI). The performance difference between the zero-forcing (ZF) and ML techniques is further investigated. On the other hand, the comparison of receive diversity techniques in multi-cell scenario is achieved in terms of SINR and distribution and coverage rates. The performance of these combining techniques is investigated through analytical studies using the Monte Carlo (MC) method. Performance analysis of ADRs is presented in a multi-cell scenario. The result showed that the performance of SMP improves when an

ADR with a larger number of PDs is applied, whilst in receive diversity, the frustum-type ADR does not offer performance benefit.

2. Development of a duplex VLC prototype for the IoT application, showing a wide communication coverage using a prototyped ADR. To find an optimum ADR type in a single-cell application with multiple light emitting diode (LED) transmitters, the performance using receive diversity techniques including selection combining (SC), equal gain combining (EGC), and maximum ratio combining (MRC) is analysed through analytical metrics. The theoretical result indicated that the frustum-type ADR shows stable SNR performance and any combining technique has sufficient performance regardless of implementation complexity. Therefore, EGC is applied in the AFE design for experimental demonstration. The design is compact in size, and the prototype can be operated on a single power supply and is also provided with a wide FOV using the ADR. It suits a mobile link by incorporating an automatic gain control (AGC) in the design. Furthermore, real-time IoT sensor data transmission is demonstrated. In the result of BER against distance, 2 Mbps data transmission is possible at up to 3.2 m. Furthermore, the coverage rate showed that the ADR coverage area where communication can be supported is more than doubled. The real-time demonstration showed the feasibility of reliable duplex connectivity in VLC-aided IoT sensor networks.

3. Development of a novel integrated VLC-RF system designed for secure industrial IoT applications. The scope of the proposed system includes all stages of IoT architecture from nodes to the WAN through APs as a network gateways. The design is improved compared to the VLC prototype in the previous contribution by modifying the AFE design and adding RF connectivity for integration with the RF system. The added RF system can be used for hybrid applications for robustness and also for the full scale of VLC-IoT supported by the WAN. To demonstrate the overall performance of the proposed system, both fundamental aspects and system efficacy are analysed. In the fundamental experiment, the performance of the prototype is compared with that of a single PD receiver in terms of SNR, SeCap and BER. Then, in the system performance demonstration, the elapsed time, including response time, one-way latency, and RTT, is measured to show the feasibility of the proposed VLC-RF system as real-time industrial IoT applications. The experimental result indicates that the designed ADR transceiver can support communication with enhanced PLS of double SeCap and with more than 50 % coverage rates, covering the half of the area in the two-AP scenario. Furthermore, the demonstration

of system performance shows the feasibility of reliable duplex connectivity in VLC-RF aided IoT sensor networks by showing a millisecond order latency. In the demonstration, sensor data transmission, image data transmission, and integration of the robot arm system are verified.

4. Developing a WDM-based VLC prototype using RGB colour PDs to further explore the ADR capability. The prototype accommodates three channels of communication for WDM, assigned to each colour. The synthesised FOV by ADR of this prototype is assessed. Performance is analysed in terms of SNR, BER and SINR. Multiplexing of transmission by the different wave length is then demonstrated. In the demonstration, data from different sensors are transmitted using WDM. Through experiments, WDM using RGB colour PDs is verified under the existence of SINRs from different colours.

1.4 List of Publications and Presentations

In terms of contributions to knowledge in this thesis, the following publications in journals and conference proceedings and invited presentations have been contributed:

Journal Papers

[J1]. R. Harada, and W. O. Popoola, "Study, Design, and Implementation of VLC With Angular Diversity Receiver for IoT Systems," in IEEE Internet of Things Journal, vol. 11, no. 23, pp. 38861-38870, 1 Dec.1, 2024, doi: 10.1109/JIOT.2024.3455773.

[J2]. R. Harada, and W. O. Popoola, "Experimental Demonstration of Integrated VLC-RF System for Secure Industrial IoT Applications," in IEEE Internet of Things Journal, doi: 10.1109/JIOT.2025.3639498.

[J3]. R. Harada and W. O. Popoola, "Design of Multi-colour VLC System with Angular Diversity Receiver," in IEEE Photonics Technology Letters. **[Under Review]**

Conference Papers

[C1]. R. Harada, C.T. Geldard and W. O. Popoola, "Performance Analysis of Angular Diversity Receivers in Visible Light Communications," 2023 IEEE 34th Annual International

Symposium on Personal, Indoor and Mobile Radio Communications (PIMRC), Toronto, ON, Canada, 2023, pp. 1-6, doi: 10.1109/PIMRC56721.2023.10294068.

[C2]. R. Harada, C.T. Geldard and W. O. Popoola, "Performance Analysis of Angular Diversity Receivers in Multi-Cell VLC Systems," GLOBECOM 2023 - 2023 IEEE Global Communications Conference, Kuala Lumpur, Malaysia, 2023, pp. 4710-4715, doi: 10.1109/GLOBECOM54140.2023.10437542.

[C3]. R. Harada and W. O. Popoola, "Design and Implementation of Angular Diversity Receiver for VLC IoT Sensor Networks," 2024 IEEE Globecom Workshops (GC Wkshps), Cape Town, South Africa, 2024, pp. 1-6, doi: 10.1109/GCWkshp64532.2024.11101010.

Invited Presentations

[P1]. R. Harada, "Study abroad in the UK for research on the VLC technique with the Angular Diversity Receiver at The University of Edinburgh, UK," Experience talks about studying abroad for young researchers hosted by Acquisition, Technology & Logistics Agency (ATLA), Ministry of Defense (MOD), Shinjuku-ku, Tokyo, Japan, 2025.

[P2]. R. Harada, "Research of VLC techniques with the Angular Diversity Receiver at The University of Edinburgh, UK," OPTICS & PHOTONICS International Exhibition 2025 (OPIE'25), Yokohama, Kanagawa, Japan, 2025.

1.5 Thesis Outline

The thesis consists of seven chapters, each serving a specific purpose and contributing to the general understanding of the thesis topic. This chapter provides an introduction that consists of the motivations behind the VLC techniques and objectives. In addition, the chapter also outlines contributions to knowledge and publications from the work presented in this thesis. The rest of the thesis is organised as follows.

Chapter 2 provides background information and a review of the literature on VLC technology, including its key characteristics, benefits, and potential challenges. It also covers the AFE in the VLC transceiver and components of light sources and detectors, as well as the optical channel model of the VLC system. In addition, the chapter introduces an ADR technique that is based

on MIMO techniques. Finally, the chapter compares and discusses the state-of-the-art literature on the topic of the thesis.

Chapter 3 of this thesis presents the analysis of the performance of ADRs in multi-cell VLC-based MIMO (VLC-MIMO) networks. First, the system model for an analytical study is described. This includes channel models of LOS and NLOS and ADR configurations. Then, two SMP schemes with ZF and ML detection algorithms and three receive diversity techniques are introduced: SC, EGC, and MRC. In the result section, the simulation parameters are defined and the results are shown with comparisons of different configurations and techniques, as well as with an analysis of performance.

Chapter 4 evaluates the ADR technique for VLC in the IoT application. Firstly, the system model and related techniques in the single-cell scenario are introduced for performance analysis of various ADR types. The VLC-IoT prototype proposed using the ADR is then described. This includes the transceiver circuit design, the AFE design, the ADR model design, and the PCB design. Using these analytical models and prototypes, the results are shown.

Chapter 5 introduces the prototype for integrated VLC-RF systems for secure industrial IoT applications. The differences from the VLC-IoT proposed in **Chapter 4** are the extended concept and the prototype design for the VLC-RF hybrid system. In particular, the added RF connectivity is described and system performance is mainly demonstrated. In the results of the experiment, PLS performance superiority is verified and the coverage performance is shown compared to the result of **Chapter 4**. Demonstrations of various industrial IoT scenarios are presented with performances of latency such as response time.

Chapter 6 details the WDM implementation of the ADR-based VLC system to show ADR capability in multiplexing communication scenarios. The chapter covers the design and development of the PCB prototype with experimental results. The performance of the prototype is presented with metrics such as SNR, SINR, and BER. The demonstration of the proposed WDM application validates the feasibility of the higher data rate.

Chapter 7 summarises the main findings and important discoveries of the research presented in this thesis. Not only does it acknowledge the limitations inherent in the study, but it also proposes potential extensions for future investigation to other applications and scenarios.

Chapter 2
Background and Literature Review

2.1 Introduction

Modern communication systems are becoming increasingly important as wireless communication technologies expand to meet the demands of a rapidly evolving information society. According to statistics [28], mobile data traffic grew annually by more than 20 % on average and reached approximately 160 exabytes per month at the end of 2024. This occurred not only from the increase in the mobile subscription, but also from the average volume of data per subscription. Around 75 % of this data traffic is driven by enterprises, such as video streaming [29]. The evolution of 5th Generation (5G) technologies enabled various communication use cases using high-speed, low-latency functionalities. Quite recently, the invention of artificial intelligence technology such as Generative AI is expected to create more use cases in mobile networks through devices such as laptop, smartphones or augmented reality glasses, together with scalable multimodal Generative AI applications [30]. Generative AI applications demand high-volume traffic, resulting in higher frequency usage. In the next generation of mobile system, 6th Generation (6G), the technology would realise cyber-physical worlds based on digital twins or extended reality, including augmented reality, virtual reality, and mixed reality. In the cyber-physical world, the integration of digitally projected objects with their physical counterparts in a digital representation will allow their harmonious merging into mixed reality services, thereby augmenting the tangible world. 6G requirements are proposed as key performance indicators: extreme high data rate of more than 100 Gbps, ultra-low latency of up to 1 ms, extended coverage, and massive connectivity [31]. Therefore, higher frequency bandwidths are being considered for wireless access such as the millimetre wave and the terahertz wave.

Wireless communications, including wireless fidelity (Wi-Fi) and mobile communications, face challenges such as overcrowding of bandwidth, security issues, and increased power consumption, which could become major obstacles in the development of future communication technologies. Moreover, the demands for high-speed communication and instalments in potential

use-cases put high pressure on the available bandwidth. Against this background, visible light communication (VLC) that uses a light spectrum emerges as a viable solution. VLC attracts attention as a new means of communication, as a technology with the potential to complement or even solve the limitations of existing wireless communication technologies, offering high-speed, secure communication with low power consumption. It is expected to provide low power, fast, and secure means of communication. VLC is encompassed as a sub-technology in optical wireless communication (OWC) technology that transmits information over a free-space optical channel. Optical signals carrying information are transmitted through a light source by changing the intensity of light, and modulated light is detected directly in a photodetector of the VLC receiver.

The VLC technology traces its origins back to human eye communication in BC to the 18th century, beginning to develop in the early 20th century. Since about the 7th century BC, people have used smoke and fire as signals to transmit messages [32]. Polished metallic plates were used to send signals over long distances by reflecting sunlight [33]. Semaphores invented by Claude Chappe in 1794, were a series of towers with mounted arms that transmit information by modulated tilt angles. In 1880, the photophone was the most widely known as an early demonstration of the modern telephone invented by Alexander Graham Bell [34]. This device concentrates sunlight onto a mirror and modulates the light intensity by the vibration of the mirror caused by voice. At the receiver with more than 200 m distance, the light shines on the selenium and its resistance changes into a change in current, producing output as sound. As light emitting diode (LED) illumination technologies evolved, modern VLC research using LEDs then began. Fundamental VLC studies using LEDs to transmit data were investigated by the Nakagawa Laboratory at Keio University in Japan [35–37]. The concept of light fidelity (Li-Fi), a subset of VLC technology, was introduced by a research group in the UK, led by Haas, who coined the term Li-Fi in 2011 [38].

Along with the VLC technological advancements, standardisation activities have been carried out to encourage the realisation of VLC applications. As one of the OWC media, infrared (IR)-based communications are promoted by the Infrared Data Association, and specifications for IR mobile communications were defined in 1997 [39]. In 2003, Nakagawa founded a VLC Consortium to accelerate research and commercialisation [40]. The consortium proposed the initial standardisation for VLC in 2007 and the VLC standard was accepted by the Japan Electronics and Information Technology Industries Association [41]. VLC Associations, a successor to the

VLC Consortium, was established in 2014 to advance VLC standardisation. The VLC global standardisation process was carried out within the Institute of Electrical and Electronics Engineers (IEEE) 802.15.7 Working Group [42]. This standard includes the physical layer (PHY) and media access control (MAC) layer parameters for short-range VLC. Recent standardisation activities are still ongoing for realisation of the VLC systems. International Telecommunication Union Telecommunication Standardization Sector (ITU-T) G.9991 is a standard for high-speed indoor visible light communications, specifying the system architecture, PHY, and data link layer (DLL). The standard, also known as G.vlc, is designed on the basis of giga-bit home networking technologies, such as power line communications [43]. G.9991 has been officially published by ITU-T, with a revised version (Amendment 2) added in 2021. Products compliant with this standard, such as LED backhaul and Li-Fi systems, are available on the market. IEEE 802.15.13 was published to facilitate the industrial use of OWC in 2023 [44]. The standard is based on giga-bit home networking technology and employs dynamic time division multiple access and multiple-input multiple-output (MIMO) technologies, enabling multi-gigabit communications over a range of up to 200 m. IEEE 802.11bb, a standard for Li-Fi, was officially approved in July 2023 and is characterised by the use of infrared radiation (800-1000 nm) for data communication compatible with Wi-Fi [45].

Recent works have proposed the integrated VLC system with radio frequency (RF)-based networks in various use cases. An important thing in hybrid usage is to obtain efficient interoperability to overcome the challenge of co-existence [46]. In addition, user mobility must be considered in hybrid networks due to the different coverage characteristics of VLC and RF. VLC attracts Internet of Things (IoT) due to its features, as the growing number of IoT devices imposes new challenges on the IoT network to accommodate the different services of devices, things, and machines [47]. To satisfy strong needs to have sufficient bandwidth in industry, VLC has been considered for applications in industrial IoT [46, 47]. Industrial IoT setups demand more intricate operations compared to those of consumer IoT. Specific challenges prevalent in industrial IoT contexts encompass link distance, attenuation due to airborne particles, multipath effects, and signal degradation and blockage [7]. Although some of these challenges overlap with consumer IoT applications, the intensity is heightened within the more stringent industrial IoT environments. Research in these challenging settings also focuses on developing algorithms and models to predict the remaining useful life of devices, an essential element in the deployment of industrial IoT systems [48–50]. In addition, within industrial IoT environments, the examination of confidentiality performance is crucial to evaluate security risks

such as eavesdropper (ED) [51–55]. These investigative areas are vital for the establishment of robust and secure industrial IoT infrastructures.

This chapter presents an overview of the VLC technology, beginning with the fundamental model, applications, and advantages and disadvantages. Background information applied to the research is also described including the basic system model and components of the VLC system. The chapter concludes with a literature review of state-of-the-art works related to the thesis. This critical review clarifies the gaps by highlighting current knowledge and highlights the research motivation addressed in this thesis. The review also provides the significance of contributions presented in subsequent technical chapters of the thesis.

2.2 Overview of Visible Light Communication

VLC is in the category of OWC, a wireless communication technology that uses optical spectrum to transmit information. In OWC, there are free space optical communication (FSO) , IR , and ultraviolet (UV) communications as a subgroup category in addition to VLC. These OWC technologies are based on each spectrum in the optical band. Fig. 2.1 shows the spectrum of electromagnetic, IR , visible light, UV, X-rays, and gamma rays. VLC can be used as a communication medium due to its advantages and features. It also has limitations and challenges to provide robust and reliable communication.

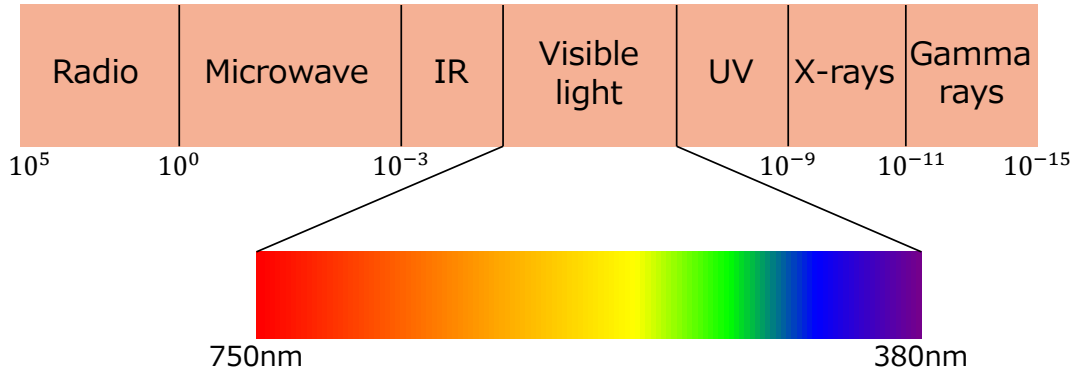

Figure 2.1: *The spectrum in the rage of radio to gamma rays, highlighting the visible light.*

2.2.1 Advantages and Challenges

There are advantages and challenges of VLC, as shown below. It is essential to implement VLC in the actual system, making use of the advantages and minimising the challenges. Although it offers benefits such as the absence of electromagnetic interference (EMI) and high security, it also faces challenges such as directivity, communication distance, and the influence of ambient light. Future technological developments are expected to overcome these challenges and expand their applications in various fields.

Advantage

- No EMI: Unlike RF communications, it can be used in locations where radio wave usage is restricted, such as hospitals and planes. It also avoids EMI with other wireless communication systems [56].

- High Security: The communication area is limited to the range in which light reaches, and it does not penetrate walls, reducing the risk of information leakage [57].

- Low cost: Existing lighting equipment can be used as a communication infrastructure, eliminating the need for new additional infrastructure. With the widespread adoption of LED lighting, relatively inexpensive system construction is possible [47].

- High-Capacity Communication: The visible light frequency band is wide, promising high-speed and large-capacity data communication compared to the RF spectrum band [56].

- Safety: Visible light is harmless to the human body, allowing safe use [2].

Challenges

- Directivity: Light has a high directivity, so communication is interrupted by obstacles, resulting in loss of the communication link. Moreover, VLC is based on line-of-sight (LOS) communication because of the directivity [56].

- Short Communication Distance: Compared to radio waves, light attenuates more easily and is not suitable for long-distance communication [58].

- Environment effect: External light sources, such as sunlight and other light sources, can become noise, affecting communication quality [59]. Outdoor use can lead to unstable communication due to weather conditions such as rain and fog.
- Challenges in Bidirectional Communication: Many current systems primarily focus on downlink (DL) communication, and achieving bidirectional communication poses challenges [60].
- Difficulty in Mobile Applications: Mobile applications cause misalignment, resulting in unreliable communication [47]. Obstacles are likely to occur between the light source and the receiver, making stable communication in mobile scenarios difficult.

2.2.2 Use cases of VLC

VLC systems can be used in various use cases and applications such as navigation, healthcare, transport, industry and smart cities.

Use Cases and Applications

- Industrial Applications:

  VLC is being considered for its role in manufacturing plants, warehouses, mines, and other harsh industrial environments [7, 61]. VLC can provide reliable low-latency communications for robots and automated systems in factories where EMI from machinery can disrupt RF signals. It also enables monitoring and control in sensitive areas, such as power plants and chemical plants, where RF radiation could be hazardous. Tracking personnel and equipment in mines and tunnels can improve safety and efficiency. Furthermore, the potential for high data rate communication in downhole monitoring in the oil and gas industry has been indicated [7]. The resilience of VLC to EMI makes it a superior measure over RF-based communication in industrial environments with high levels of electrical noise. This reliability ensures consistent and accurate data transmission for critical industrial operations, leading to enhanced efficiency and safety.

- Underwater Communication: VLC offers a promising solution for underwater communication in which radio waves are absorbed [62]. Its high data rates can enable efficient communication between underwater devices, robots, and sensors. This can be particularly useful for environmental monitoring, underwater exploration, and communication

with submerged vehicles. The promising platforms are remotely operated vehicle or autonomous underwater vehicle.

- Vehicular Communication: VLC is integral to intelligent transportation systems (ITS) by facilitating both vehicle-to-vehicle and vehicle-to-infrastructure communications [63, 64]. Utilising headlights, tail lights, traffic signals, and street lamps as VLC transmitters, vehicles can exchange information with each other and the surrounding infrastructure, thereby enhancing road safety and traffic flow. Key applications encompass pre-crash detection, collision avoidance, lane departure alerts, traffic management, and even autonomous vehicle operations. The low latency characteristic of VLC is vital for the real-time communication demands of vehicular networks [63]. In ITS, VLC augments safety and operational efficiency by complementing existing RF systems by providing redundancy and reliability, especially in environments requiring rapid, short-range communication [64]. Additionally, the widespread adoption of LED technology in vehicles and infrastructure renders VLC a potentially economical method for deploying sophisticated communication features in ITS.

- Indoor Positioning and Navigation: VLC can be used for indoor positioning systems to enhance navigation and mapping within indoor environments where GPS signals are unreliable. Indoor positioning systems based on VLC, called visible light positioning, can be applied in offices, buildings, car parks, subways, tunnels, warehouses, and airports guiding users to specific locations. LED luminaires enabled by VLC transmit unique codes or location data to mobile devices equipped with a VLC receiver. The level of precision achievable with visible light positioning is up to 10 centimetres [59]. Applications include way-finding, asset tracking in warehouses and hospitals, and navigation for robots and autonomous vehicles. The existing lighting infrastructure present in indoor environments offers a significant advantage in the deployment of visible light positioning without major hardware modifications. Furthermore, visible light positioning offers enhanced privacy and security compared to RF-based systems, as light signals are confined to a physical space. Visible light cannot penetrate walls, preventing eavesdropping or unauthorised access to location data, making it a more secure option for indoor positioning in sensitive environments.

- IoT and Smart Cities:

  VLC has the potential to contribute to smart city infrastructure and enable communica-

tion within the IoT. VLC can provide massive connectivity, high data rates, and energy efficiency in public spaces using existing LED street lights and building illumination [47]. It also enables communication between various smart city devices and sensors for applications such as smart lighting, traffic management, and environmental monitoring. Furthermore, VLC can be utilised for indoor localisation within smart buildings to enable automation and personalised services. The vast bandwidth of the visible light spectrum offers significant potential to support the massive connectivity demands of smart cities and the increasing number of IoT devices. As the number of connected devices continues to grow, VLC can provide the necessary bandwidth whilst avoiding spectrum congestion and ensuring reliable communication.

- Healthcare:

  The VLC has promising applications within hospitals and healthcare facilities. It can mitigate EMI with sensitive medical equipment such as magnetic resonance imaging [65]. In addition, it enables secure wireless data transfer of patient records and medical images and supports communication with medical devices and wearable sensors [66]. The non interfering nature of VLC is particularly valuable in healthcare settings where RF signals could potentially disrupt critical medical devices. This advantage significantly improves patient safety and the reliability of medical procedures by eliminating the risk of equipment failure associated with EMI.

2.3 VLC System Model

In this section, the typical VLC system model is described. Fig. 2.2 illustrates the typical VLC transmission model composed of a transmitter and a receiver. The typical VLC transmitter (Tx) transmits signals containing modulated data. On the receiver side, a detector received the optical signals through the VLC channel. The detected signals are reconstructed in the analogue front end (AFE) of receiver (Rx), and the signals are demodulated as output data. Each of these key components will be discussed below.

2.3.1 Transmitter

The VLC transmitter consists of a modulator (Mod), a transmitter AFE, and an emitter. In the Mod block, the data coming from devices such as computers or sensors are modulated using an

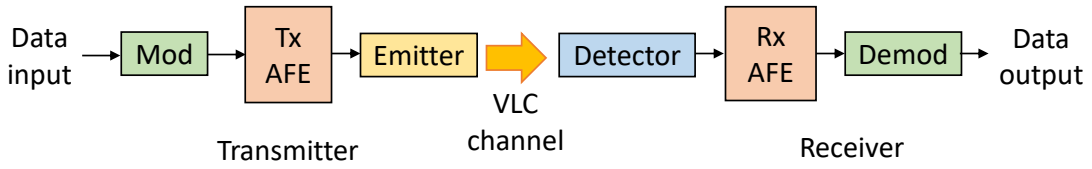

Figure 2.2: *The typical VLC transmission model.*

appropriate modulation technique. The following Tx AFE works as an emitter driver to transmit the modulated signals via the connected emitter. Each part is described in the following.

2.3.1.1 Modulation

Digital information, including stream of binary digits, enters the transmitting device. This information is modulated to change the light intensity of the LED. These modulation techniques in VLC comprise the following [57]:

On-off keying (OOK): OOK is the most straightforward strategy, where a '1' illuminates the LED and a '0' turns it off. Although it suffers from lower spectral efficiency compared to other schemes, it is easy to implement.

Pulse width modulation: This technique encodes data by changing the duration of light pulses, facilitating data transmission whilst maintaining steady illumination levels.

Pulse position modulation: This method involves encoding the data by timing a light pulse within a predefined interval, offering superior noise resistance compared to OOK.

Orthogonal frequency division multiplexing (OFDM): This scheme disperses data across several sub-carriers, designed for high-throughput and high-capacity data transfer. Given that VLC systems must be operated with real values, adaptations such as DC-biased optical OFDM or asymmetrically clipped optical OFDM are frequently used [67].

VLC-specific modulation techniques: Unique approaches such as colour shift keying, which leverage variations in LED colour, are used to encode information [57].

2.3.1.2 Transmitter's Analogue Front-End

The primary function of the AFE in the transmitter is to convert the digital output of the modulator into an analogue current that can appropriately drive the LED, allowing the emission of modulated light into the VLC channel. The structure of the AFE depends on the modulation scheme or the applications. Thus, a typical AFE consisting of a digital-to-analogue converter (DAC), filter, and LED driver is described. DAC converts the digital signal into an analogue waveform. The DAC sampling rate is a key parameter for high-speed data rates. A low pass filter (LPF) is often used to cut off high-frequency components, such as the aliasing noise contained in signals from the DAC. Therefore, the cutoff frequency of the LPF should be designed to match the communication bandwidth. Finally, a LED driver is the most critical part of the AFE. It transforms the filtered analogue signal into the current and voltage necessary to drive the LED. If needed, amplifiers are implemented with the driver to amplify the signals before driving the LED. DC bias is also an optional component to superimpose the bias voltage and support a LED characteristic that requires real-valued signals and positive light intensity. The constant DC bias also allows for both dimming control and data transmission simultaneously for illumination [68]. The high-speed response, linearity and thermal design must be taken care of for the AFE design. A wide-bandwidth component such as a high-speed operational amplifier (op-amp) has to be chosen in the AFE to rapidly modulate the LED's forward current and account for the LED's parasitic capacitance to ensure proper operation. It is vital to ensure that the modulated signals operate within the LED's linear region to prevent distortion. This is especially crucial for multilevel modulation schemes like OFDM, where nonlinearity can severely degrade signal quality. In AFE design, effective heat dissipation is necessary because a LED generates heat during operation. The high temperature affects the LED characteristics and even harms the AFE.

2.3.1.3 Emitters

The emitters convert the electrical signal into an optical output that is transmitted through an optical channel. The high-speed response is a crucial characteristic for data transmission. Therefore, typical light-emitting elements are the LED and laser diode (LD). For any emitters, it must be noted that optical signals have only positive values. So, as described above in 2.3.1.1, specific modulation schemes have been considered that address only the real value.

LED is a semiconductor device that emits light when an electric current passes through it.

An LED functions through a p-n junction, which combines 'p-type' and 'n-type' semiconductor materials. The p-type has holes as positive charge carriers, whereas the n-type is rich in electrons. When a forward bias voltage is applied, electrons and holes move towards the junction and recombine, releasing energy as photons. The colour of light emitted by an LED is determined by the energy gap of the semiconductor. An LD is also a semiconductor device similar to an LED. The key difference between an LD and an LED lies in the light emission process [69]. Whilst LEDs use spontaneous emission, LD use stimulated emission within an optical cavity to produce light. This requires a high concentration of electrons and holes and a structured optical cavity that acts as a resonator. Once photons are generated, they stimulate further emission, leading to light amplification. When the amplification exceeds losses, the lasing threshold is reached, producing a coherent, monochromatic, directional, and high-intensity laser beam. Table 2.1 shows a comparison between LED and LD. Compared to LDs, LEDs exhibit reduced directionality, making them less effective for long-range communication without additional optical components. The LED's constrained bandwidth requires sophisticated modulation techniques to achieve higher data rates. LDs are less suitable for general illumination due to their point source nature, necessitate stringent eye safety precautions at higher powers, incur higher costs, and require precise optical alignment. Each emitter has different characteristics, therefore, resulting in different suitable applications. For an indoor VLC scenario, LEDs are the typical element due to their simplicity, low cost, and safety. The indoor system does not require high output power due to the short distance and requires mobile suitability in a broad direction. On the other hand, LD is used for long-distance communication, such as FSO or satellite communications. This thesis focusses on LED-based VLC because of its advantages in indoor mobile scenarios.

2.3.2 Receiver

The VLC receiver consists of a detector, an AFE for the receiver, and a demodulator (Demod). The demodulation process reverses the modulation applied at the transmitter, restoring the original digital data. Each part of a receiver is described below.

2.3.2.1 Detectors

A detector in the VLC receiver is the light-sensitive element that converts optical signals into electrical current through the inner photoelectric effect, typically involving a p-n or PIN junc-

Table 2.1: *Comparison of Light-Emitting Elements*

Feature	LED	LD
Optical power	Low	High
Bandwidth	Narrow (up to hundreds of MHz)	Broad (GHz and above)
Directivity	Low directional	High directional
Coherence	Incoherent	Coherent
Implementation	Relatively simple	Relatively complex
Cost	Low	High
Reliability	High with long lifespan	Low, especially at high power
Safety	Relatively safe	Potential eye hazard
Applications	Li-Fi, indoor positioning	Satellite communication, FSO

tion. When photons strike the semiconductor material, electron-hole pairs are generated, separated under a reverse bias voltage, and created a photocurrent proportional to light intensity. PIN photodiodes (PDs) and avalanche PDs (APDs) are commonly used for VLC receivers. The PIN PD is the most common type of photodetector in VLC. Its structure consists of a P-type layer, an intrinsic layer, and an N-type layer. When reverse biased, it creates a wide depletion region primarily within the intrinsic layer, allowing for efficient photon absorption and electron-hole pair generation. The generated carriers are separated and collected because of an electric field, contributing to a photocurrent proportional to the light intensity. In contrast, an APD is a highly sensitive semiconductor device, featuring an internal gain mechanism to amplify the detected light signal. It operates under a high reverse bias voltage close to its breakdown threshold, generating electron-hole pairs when photons are absorbed. These carriers are accelerated by a strong electric field, initiating an avalanche multiplication process that creates additional carriers in a cascade effect. Key advantages include high sensitivity and improved signal-to-noise ratio (SNR) in low-light conditions. However, APDs that require higher operating voltages can introduce excess noise due to the random nature of the avalanche process, are sensitive to temperature variations and are more complex and expensive than standard photodetectors, such as PIN PDs [70]. Table 2.2 shows a comparison between PIN PD and APD. The internal gain, which only APD has due to avalanche multiplication, is typically more than 50 dB [71]. PIN PD has a wider dynamic range than that of APD because APD tends to be saturated due to internal gain. For an indoor VLC scenario, PIN PD is suitable for its low cost, easy implementation and sufficient performance. This thesis focusses on the PIN PD receiver

due to its advantages in indoor IoT scenarios.

Table 2.2: *Comparison of photodetectors*

Feature	PIN PD	APD
Internal Gain (dB)	1	Typically more than 50
Responsivity (A/W)	Typically 0.4 - 0.7	Several to tens of A/W
Noise	Lower	Higher
Response speed	Several MHz to GHz	Hundreds of MHz to a few GHz
Operating Voltage	Few volts	Tens to hundreds of volts
Complexity	Simpler	More complex
Cost	Lower	Higher
Dynamic Range	Wider	More limited
Temp. Stability	Good	Sensitive

2.3.2.2 Receiver's Analogue Front-End

The Rx AFE design is crucial because it determines the performance of the PHY. To achieve reliable VLC, challenges must be overcome, such as noise, non-linearity, dynamic range, power consumption, component selection, and circuit design. All components used in the AFE need to satisfy the required bandwidth and response speed. In addition, these components must operate within the dynamic range and the linearity domain in order not to be saturated. Therefore, designing an optimised AFE with optimal components is significant in achieving the required VLC performance.

The main function of the receiver AFE is to convert the weak optical current detected by a PD into a voltage signal, amplifying it whilst minimising noise, so that the processed signals can be demodulated by the subsequent demodulator. A typical Rx AFE consists of a transimpedance amplifier (TIA), amplifiers, filters, and an analogue-to-digital converter (ADC). Optical filters are often placed in front of a PD to reduce ambient light noise by blocking light outside the VLC signal's spectral band, leading to suppression of the shot noise and improvement of SNR. Generally, a PD is connected to the input of TIA to convert current into voltages with gains. The TIA converts the weak current signal from PD into a voltage signal suitable for subsequent signal processing whilst amplifying it. Designing TIA with optimal gain and bandwidth is essential because it largely determines the system's noise performance. The phase margin should

also be taken care of for operational stability. The typical TIA consists of an op-amp with a feedback resistor, which determines the bandwidth with the PD's capacitance, and the TIA's input capacitance. The TIA is sometimes followed by high pass filter (HPF) to block non-data-carrying DC bias. Then, the voltage signals are amplified by voltage amplifiers to a suitable amplitude level. This amplification stage can be multistaged to obtain a good amplification performance. To compensate for fluctuations in received power, automatic gain control (AGC) can be implemented after the amplification stage. In the AGC loop, the variable gain amplifier is used to adjust the gain to maintain the constant output range. LPF is placed before or after the amplifier stage, removing the noise and interference that exist outside the band. The processed signals go to the next stage, the demodulator, via an ADC. The ADC converts the analogue voltage processed in the AFE into digital signals. The sampling rate and resolution must be sufficient for the data rate.

2.3.3 VLC channel model

The MIMO channel model for VLC is described using theoretical equations. The system model incorporates N_{t} LEDs and N_{r} PDs within an indoor setting. Furthermore, this model is adaptable for angular diversity receiver (ADR) applications. The DL functionality is executed by N_{t} LED transmitters mounted on the ceiling of the room. A user, equipped with a PD receiver, is positioned either on a table or the floor. Each transmitter employs OOK modulation via intensity modulation and direct detection (IM/DD) with the electrical signal vector $X = [x_1, x_2, ..., x_{N_{\mathrm{t}}}]^T$, where $[.]^T$ denotes a transpose operation. These signals emitted from the LEDs are received by the receiver through the VLC-based MIMO (VLC-MIMO) channel. The received signal vector at all identical PDs is expressed as [72]

$$\mathbf{Y} = \mathcal{R}\mathbf{H}\mathbf{X} + \mathbf{N} \tag{2.1}$$

where $\mathcal{R}$ is the responsivity of PDs; $\mathbf{N}$, the vector $N_{\mathrm{r}} \times 1$, is a vector of real-valued additive white Gaussian noise (AWGN) with zero mean and variance σ_n^2, and $\mathbf{H}$ is the channel matrix $N_{\mathrm{r}} \times N_{\mathrm{t}}$. This expression can be formulated as follows [73].

$$\mathbf{H} = \begin{bmatrix} h_{11} & \dots & h_{1N\mathrm{t}} \\ \vdots & \ddots & \vdots \\ h_{N\mathrm{r}1} & \dots & h_{N\mathrm{r}N\mathrm{t}} \end{bmatrix} \tag{2.2}$$

where h_{ij} indicates the channel gain of i_{th} PD (PD$_i$) from j_{th} LED (LED$_j$).

The geometry of the link between the PD$_i$ and the LED$_j$ is shown in Fig. 2.3. The channel gain h_{ij} incorporates both the LOS and non-line-of-sight (NLOS) elements, arising from wall reflections. The total channel gain, h_{ij}^{Los} and h_{ij}^{Nlos}, is represented as [21, 23]:

$$h_{ij} = h_{ij}^{\mathrm{Los}} + h_{ij}^{\mathrm{Nlos}} \tag{2.3}$$

$$h_{ij}^{\mathrm{Los}} = \begin{cases} \frac{(m+1)A}{2\pi d_{ij}^2} \cos^m \varphi_{ij} \cos\theta_{ij}, & \theta_{ij} \le \Psi_{1/2} \\ 0, & \theta_{ij} > \Psi_{1/2} \end{cases} \tag{2.4}$$

$$h_{ij}^{\mathrm{Nlos}} = \begin{cases} \sum_{k=1}^{K} \frac{(m+1)AA_{\mathrm{r}}\rho_{\mathrm{k}}}{2\pi d_{jk}^2 d_{ik}^2} \cos^m \varphi_{jk} \\ \cos\alpha_{jk} \cos\beta_{ik} \cos\theta_{ik}, & \theta_{ik} \le \Psi_{1/2} \\ 0, & \theta_{ik} > \Psi_{1/2} \end{cases} \tag{2.5}$$

where $m = -\ln 2 / \ln\cos\Phi_{1/2}$ is the order of Lambertian emission in relation to the semi-angle of the LED at half power $\Phi_{1/2}$ and A denotes the active area of the PD. As shown in Fig. 2.3, d_{ij} indicates the distance between LED$_j$ and PD$_i$, and ϕ_{ij} is the emission angle between a

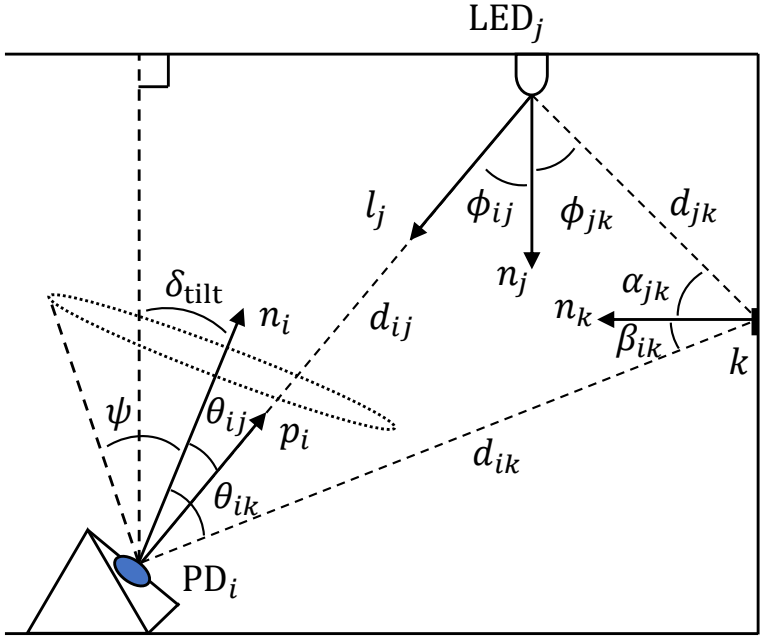

Figure 2.3: *The geometry between LED$_j$ and PD$_i$.*

vector directing from LED$_j$ to PD$_i$ and a normal vector of LED$_j$ n_j. θ_{ij} means the incident angle between a vector directing from LED$_j$ to PD$_i$ and a normal vector of PD$_i$ n_i; $\Psi_{1/2}$ is the half angle of the field of view (FOV) of the PD. For the NLOS component of h_{ij}, described in (2.5), K is the number of reflections and A_{r} is the reflective area. ρ_{k} is the reflective coefficient. d_{jk} and d_{ik} are the distance between the LED$_j$, the PD$_i$ and the reflective point k. φ_{jk} is the emission angle between a vector directing from LED$_j$ to the reflective point k and n_j; α_{jk} and β_{ik} are angles between a normal vector of k, n_k and vectors of k to LED$_j$ and PD$_i$, respectively; θ_{ik} is the incident angle between a vector directing from PD$_i$ to k and n_i.

2.4 Literature Review and Research Gaps

2.4.1 ADR based VLC System

There is a substantial body of research investigating the use of VLC techniques for indoor wireless communication systems, as highlighted in numerous studies [18–24, 74, 75]. Research into practical indoor VLC systems focus on multi-cell configurations, which are capable of providing extensive coverage, as considered in [20, 22, 74]. These analyses reveal that inter-cell interference (ICI) adversely impacts performance in indoor multi-cell environments, where its influence is most pronounced at cell boundaries due to overlapping illumination from multiple light sources converging on the receiver. Moreover, the FOV of a PD within a VLC receiver is a crucial parameter for achieving comprehensive coverage whilst maintaining an adequate signal-to-interference-plus-noise ratio (SINR) for VLC links [74].

The exploration of MIMO techniques within VLC frameworks has been discussed [18, 21, 76]. In the VLC-MIMO system, multiple transmitters and receivers are applied between transceivers to increase performance. In [76], three MIMO algorithms were evaluated for indoor VLC environments, and they are repetition coding; spatial multiplexing (SMP); and spatial modulation. It was observed that both repetition coding and spatial modulation contribute to system stability, whereas SMP facilitates higher data transmission rates. However, the effectiveness of SMP is compromised by co-channel interference (CCI), which consists of signals coming from adjacent transmitters that share the identical frequency spectrum.

An ADR, comprising multiple PDs orientated in different directions, has been introduced for VLC-MIMO systems to improve their performance [18–27, 77–79]. These ADRs are notably compact, making them suitable for mobile applications, and the related techniques are

based on MIMO techniques. The ADR system effectively reduces channel correlation and CCI [19]. Several different ADR configurations have been explored in these previous investigations, such as the pyramid shape and the frustum shape. In [21, 23], a pyramidal configuration with four PDs was examined. The study in [23] contrasted the pyramid type ADR with the hemisphere configuration, both with identical count of PDs, revealing that their performance is analogous due to the equal number of PDs. Research on frustum-shaped ADRs, featuring between three and six PDs have been investigated in [22], where SINR fluctuations of these configurations were analysed, indicating that increasing the number of PDs reduces these fluctuations. In [19,24,26], frustum-shaped ADRs with seven PDs have been evaluated for different applications. Specifically, [19] implemented SMP to boost capacity, whilst [24] utilised multi-LED transmit diversity as a single-cell in the ADR based VLC system to significantly extend coverage. In [26], the ADR was employed to enhance tracking and precision performance.

In the context of multi-cell VLC systems, the application of receive diversity techniques to ADRs has been explored [20,22,25]. The study in [22] made a comparison of SINR fluctuation performance across equal gain combining (EGC), selection combining (SC), and maximum ratio combining (MRC), though only the SC method was evaluated in relation to SINR distribution. The investigation detailed in [20] examined the distribution of user data rates for these diversity schemes employing a pyramid-type ADR, demonstrating the superiority of the MRC scheme in improving elevated data rates under the conditions considered. An optimisation approach regarding the receiver FOV and the angle of inclination in [25], where the adoption of the SC technique was used to determine the optimal channel in a multi-cell VLC environment.

A review of the existing literature reveals a lack of studies that perform a comparative analysis of different types of ADR. To establish the practical viability of ADR based VLC system, it is crucial to investigate the performance of various ADR configurations across different scenarios, particularly when applying techniques such as SMP and receive diversity. This allows the unique characteristics of each ADR type to be clearly identified. To address this research gap, Chapter 3 of this thesis models four different types of ADR and evaluates their performance when both SMP and receive diversity are applied. Through simulation and theoretical analysis, the performances such as bit error rate (BER) is evaluated and then the coverage performance of the system, a known challenge in VLC, is analysed.

2.4.2 Implementation of VLC-IoT System

State-of-the-art VLC-based IoT (VLC-IoT) systems and previous experimental ADR studies are discussed. Table 2.3 shows a concise comparison of the real-time VLC-IoT systems cited in the literature. The commonly used modulation techniques are OOK or pulse position modulation, selected for their straightforward implementation, achieving data rates from a few kbps to several Mbps. The study [80] explored carrier-less amplitude and phase modulation (CAP), albeit utilising an experimental setup based on resource-constrained microprocessors. In contrast, other studies have used standard hardware platforms like microcontroller units (MCUs), Beagle Bone Black (BBB), and field programmable gate arrays (FPGAs). Studies such as [9, 81–84] employed condenser lenses, focussing on static implementations such as multi-hop or repeater scenarios; these are inappropriate for mobile applications due to the restricted FOV inherent to lens systems. Bidirectional communication capabilities were employed for internode links in [16, 85], whilst [81–83, 86] presented relay communications featuring bidirectional links. Specifically, [84] supported dual link (uplink (UL) / DL) bidirectional connectivity, although the narrowing effect of condenser lenses on the FOV limits adaptability to dynamic environments. Implementing bidirectional and relay capabilities requires employing higher protocol layers beyond the PHY level, including MAC, transport (TP), and application (APP) layers. For IoT applications, the selection of power sources must be tailored to balance complexity with form factor. Designing AFEs with dual power supplies, often using dual-power op-amps for bipolar signal symmetry, is perceptibly more intricate. For example, the dual power supply structure in [9] requires an additional power management unit, increasing the AFE footprint, whilst in [84], dual AC-DC converters occupy a substantial receiver space. Previous works have never investigated the communication coverage area in VLC systems and dynamic scenarios with mobile user nodes. Chapter 4 makes novel contributions by detailing the development of a compact AFE operating on a single power supply, innovating a wide FOV by ADR, and ensuring the viability of mobile links by integrating AGC into the design.

Table 2.4 provides a summary of experimental studies concerning ADR prototype. Reference [23] employed a multiplexing technique with a four-PD ADR, evaluating channel capacity through an offline setup by unidirectional VLC link. In [26], improvements in pointing and tracking performance were achieved for underwater VLC applications. The lens array of their design resulted in an oversized ADR prototype, rendering it inadequate for wide-area applications because of the lenses' narrow FOV. The investigation in [90] focused on vehicular VLC

Table 2.3: *Comparison of real-time VLC-IoT Systems*

Reference	Receiver	Mod	Range	Data Rate	Lens	Connectivity	Power supply	Platform	Layer	Feature
[9]	Single PD	OOK	7 m	115.2 kbps	Lens	Unidirectional	Dual	MCU	PHY	Low complexity
[16]	Multiple PDs	OOK	6 m	100 kbps	No lens	Bidirectional	N/A	BBB	PHY, TP	Full-duplex
[87]	Single PD	PPM	0.5 m	20 kbps	No lens	Unidirectional	Dual	FPGA	PHY, APP	Text transmission
[81]	Single PD	OOK	13.5 m	115.2 kbps	Convex lens	Bidirectional	N/A	MCU	PHY, APP	Multihop
[82]	Single PD	PPM	12 m	2.5 ksps	Convex lens	Bidirectional	N/A	MCU	PHY, APP	Multihop
[83]	Single PD	OOK	5.5 m	55.6 kbps	Convex lens	Bidirectional	Single	MCU	PHY, APP	Repeater
[84]	Single PD	OOK	1.2 m	4 Mbps	lens	Bidirectional	Dual	UART IC	PHY, MAC	Video transmission
[86]	Multiple PDs	OOK	1 m	1 kbps	No lens	Bidirectional	N/A	MCU	PHY	Multihop
[88]	Single PD	OOK	1.1 m	56 kbps	No lens	Unidirectional	N/A	MCU	PHY	Low complexity
[80]	Single PD	CAP	N/A	N/A	N/A	Unidirectional	Dual	Offline	PHY	Low cost
[85]	Single PD	N/A	19 m	400 kbps	N/A	Bidirectional	N/A	BBB	PHY, APP	Open source
[89]	Single PD	OOK	1 m	44 kbps	N/A	Unidirectional	N/A	UART IC	PHY, APP	Low cost
Chapter 4	ADR	OOK	1.6 m	2 Mbps	No lens	Bidirectional	Single	MCU	PHY, APP	Wide coverage

applications using a three-PD ADR, measuring the rate of packet delivery in static settings. The prototype consisted of boxed PDs with built-in amplifiers, which led to a bulky configuration. These studies exhibit different objectives, yet no practical research has studied the benefits of the extensive coverage of ADR. The contributions detailed in Chapter 4, in contrast with the previous work in Table 2.4, involve developing a compact square frustum (SF)-type ADR prototype, constructing an AFE compatible with the ADR, demonstrating enhanced coverage performance, and presenting a bidirectional real-time IoT system.

Table 2.4: *Comparison of the ADR experimental research*

Reference	ADR	ADR size	Connectivity	Application
[23]	4 PDs	Large	Unidirectional	Multiplexing
[26]	7 PDs	Large	N/A	Underwater VLC
[90]	3 PDs	Large	Unidirectional	Vehicular VLC
Chapter 4	5 PDs	Compact	Bidirectional	Wide coverage IoT

2.4.3 Implementation of Integrated VLC-RF System

Comprehensive analyses of integrated VLC and RF (VLC-RF) and industrial IoT systems are examined. Table 2.5 compiles a review of existing VLC-RF and industrial IoT systems as reported in the literature. Common VLC modulation methods such as OOK, digital pulse interval modulation (DPIM), and frequency shift keying (FSK) are preferred for hardware platforms with limited resources like MCUs, BBB, and Raspberry Pi, due to their simplicity, offering data rates from a few kbps to several Mbps. In contrast, [14] employs OFDM in resource-intensive setups, such as FPGA, to enable high data rates. Studies in [81, 93, 98, 101, 102] using lenses predominantly considered static environments, making them inappropriate for dynamic applications due to the restricted FOV induced by the lenses. Bidirectional communication was implemented for internode connections in [14, 81] and for vehicular connections in [92, 102]. Conversely, many former studies advocate unidirectional VLC stemming from hybrid implementations with RF systems. However, bidirectional communication is required to improve system resilience by enabling duplex communications in the absence of RF. In VLC-RF experimental investigations, Wi-Fi is predominantly employed for establishing RF connectivity, utilising various interfaces such as modules, cards / dongles and routers. Alternative RF systems, like RF modules and message queue telemetry transport (MQTT), were used in [91, 103].

Table 2.5: *Comparison of the experimental studies of VLC-RF / industrial IoT Systems.*

Ref.	Modulation	Distance	VLC Data Rate	Lens	connectivity	RF system	Platform	Latency	Power consumption	Security
[14]	OFDM	2 m	8 Mbps	No lens	Bidirection	Wi-Fi card	FPGA	N/A	N/A	N/A
[91]	OOK	N/A	N/A	N/A	Unidirection	RF module	MCU	N/A	N/A	N/A
[92]	DPIM	5 m	250 kbps	N/A	Bidirection	Wi-Fi module	MCU	1.92 ms	✓	✓
[93]	OOK	1.2 m	1.5 Mbps	Lenses	Unidirection	Wi-Fi dongle	BBB	N/A	N/A	N/A
[94]	N/A	1.5 m	80 Mbps	N/A	Unidirection	Wi-Fi router	Offline	tens of ms	N/A	N/A
[95]	OOK	N/A	2 Mbps	No lens	Unidirection	Wi-Fi card	FPGA	N/A	N/A	N/A
[96]	OOK	N/A	0.48 kbps	N/A	Unidirection	MQTT	Raspberry Pi	10–20 ms	✓	N/A
[97]	N/A	1.5 m	6 Mbps	N/A	Unidirection	Wi-Fi	MCU	a few ms	N/A	N/A
[98]	N/A	50 m	50 kbps	Lens	Unidirection	Wi-Fi	MCU	N/A	N/A	N/A
[99]	N/A	N/A	N/A	N/A	Unidirection	Wi-Fi	N/A	N/A	No	N/A
[100]	N/A	1.8 m	N/A	N/A	Unidirection	No	Offline	N/A	No	N/A
[101]	BFSK	5 m	10 kbps	Collimator	Unidirection	No	MCU	N/A	N/A	N/A
[102]	OOK	27 m	57 kBaud	Lens	Bidirection	No	MCU	2.5 ms RTT	N/A	N/A
[81]	OOK	13.5 m	115.2 kbps	Lens	Bidirection	No	MCU	$\geq$1.87 ms Relay	✓	N/A
Chapter 5	OOK	1.6 m	2 Mbps	No lens	Bidirection	Wi-Fi module	MCU	$\geq$0.45 ms RTT	✓	✓

Achieving functional IoT applications through VLC-RF involves implementing layers beyond the PHY. Despite the significance of latency evaluation in industrial IoT, this parameter has been mostly overlooked in past studies. Interference-focused delay analysis in [92] indicated a latency peak of 1.92 ms. The work in [94] conducted a assessment of round-trip time (RTT) in both VLC and Wi-Fi systems, demonstrating that VLC exhibits enhanced rapidity compared to Wi-Fi. [96] exhibited VLC latency between 10 and 20 ms, whilst [97] noted several-millisecond response times. As reported by [102], ITS-oriented VLC achieved a minimal RTT of 2.5 ms. An indoor multi-hop VLC system was developed in [81], achieving a latency of 1.87 ms at a data rate of 115.2 kbps without relays, escalating to 3.4 ms with a relay, indicating a correlation between delay and hops. These studies cover diverse objectives, such as optimising real-time processes. Prototypes in energy-restricted industrial IoT environments demand minimal power use, yet the energy efficiency of the system remains scarcely assessed. [92] estimated power draw from component datasheets, excluding complete system verification. [96] noted 70 W consumption with LED transmitters, whereas [81] documented a mere 0.33 W per VLC node. Concerning security, a vital aspect in industrial IoT, [96] deployed a user identification feature to counteract ED, although much of the literature relies on the supposed intrinsic security of VLC without extensive testing of its physical layer security (PLS).

Chapter 5 advances the field by introducing a secure integrated VLC-RF system tailored for industrial IoT, which supports extensive coverage via Wi-Fi and ADR-based VLC with the low latency and superior secrecy capacity (SeCap) offered by VLC. The chapter evaluates enhanced coverage and latency, providing empirical validation in real-time industrial IoT contexts such as image transmission and robotic arm connectivity. The innovation of the system has been experimentally confirmed, although within a standard indoor setting, that lacks significant aerosol presence and intense ambient lighting.

2.5 Summary

This section presented the overview of VLC technology, the basic VLC system model, and a review of the literature on VLC. The VLC overview section provided a historical background on the field of VLC, following discussion of current research trends and standardisation efforts. It also outlined the characteristics of the optical band used by VLC and summarised the key advantages and challenges of the technology. For the advantage, EMI is absent in the VLC, which also provides enhanced security. However, it faces challenges, including directivity of the beam,

communication range, and susceptibility to ambient light interference. Potential applications where VLC's unique characteristics distinct from RF are particularly useful, such as navigation, healthcare, transport, industry, and IoT and smart cities, are then described. The fundamental components of a VLC system were then explained, starting with the transmission model. This is followed by a breakdown of each key element, including modulation/demodulation techniques, the AFE, and the optical emitter and detector components. A mathematical model of the VLC-MIMO channel was also presented, which is applied in analytical studies in this thesis. Finally, a review of the recent literature was presented, organised into three key categories: theoretical research on ADR-based VLC systems, the implementation of VLC-IoT systems, and integrated VLC-RF systems/industrial IoT systems. From this review, the respective research gaps were identified and the contributions corresponding to each subsequent chapter of this thesis were outlined.

Chapter 3
Comparative Analysis of Angular Diversity Receivers in VLC System

3.1 Introduction

Visible light communication (VLC) techniques have been explored for use in indoor communication systems [18–24, 74, 75, 104–107]. In [108–116], the examination of viable indoor VLC systems has led to discussions of multi-cell configurations. The works in [20, 22, 74] aim to ensure extensive coverage. Collectively, these studies identify inter-cell interference (ICI) as a significant factor that impairs the effectiveness of indoor multi-cell VLC environments. The field of view (FOV) of a photodiode (PD) in a VLC receiver is a key parameter to provide a wide coverage with a sufficient signal-to-interference-plus-noise ratio (SINR) for a VLC link [74]. Therefore, as one of the candidates to solve the VLC issue, angular diversity receiver (ADR) is applied to VLC systems to improve communication performance, such as coverage performance, interference mitigation [117–121].

Before experimental research, analytical work should be performed to obtain theoretical knowledge of the performance of ADR in VLC. Several different ADR configurations have been considered in previous work, including pyramidal shape and frustum shape. Therefore, a performance comparison of these ADR types is performed with different numbers of PDs. In this chapter, different ADR configurations are compared through simulation and numerical analysis for different indoor downlink scenarios; they are: square pyramid (SP), square frustum (SF), hexagonal pyramid (HP), and hexagonal frustum (HF). Furthermore, two spatial multiplexing (SMP) techniques are applied with detection algorithms of zero-forcing (ZF) and maximum likelihood (ML) and three receive diversity techniques: selection combining (SC), equal gain combining (EGC), and maximum ratio combining (MRC). The coverage rates of the modelled ADR configurations using these techniques are evaluated.

The remainder of this chapter is organised as follows: physical layer (PHY) techniques and ADR configurations are discussed in Section 3.2 and Section 3.3; simulation results are pre-

sented in Section 3.4; and conclusions are drawn in Section 3.5.

3.2 Physical Layer Techniques

The VLC system incorporating a multiple-input multiple-output (MIMO) channel with N_{t} light emitting diode (LED) transmitters is examined, as depicted in Fig. 3.1. This particular model is frequently referenced in the literature, including studies [18,19,21–24]. The system model previously described in Chapter 2.3.3 is employed, with SMP techniques and diversity techniques elucidated.

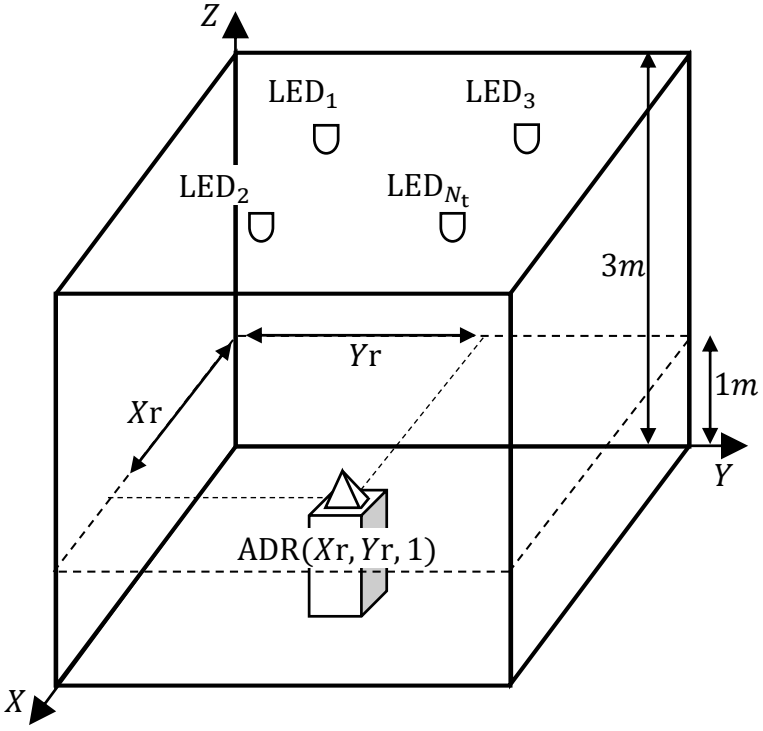

Figure 3.1: *Downlink VLC based on MIMO system model.*

3.2.1 Spatial Multiplexing

In MIMO systems, SMP methods are adopted to improve performances such as channel capacity [122–129]. When it comes to the ADR system applying SMP, PDs recognise data from each LED transmitter via the VLC-based MIMO (VLC-MIMO) channel, and the signal is demodulated to eliminate interference at the receiver using signal detection techniques. Implementing SMP necessitates more than two ($N_{\mathrm{t}} > 2$) LED transmitters to yield multiple data streams,

hence SMP is unsuitable for single-cell scenarios. ZF and ML detection algorithms are also discussed with the least squares (LS) channel estimation technique. Furthermore, the analytical bit error rate (BER) expressions are introduced.

3.2.1.1 Channel Estimation with Least Squares Approach

Within the scope of SMP, estimation of the channel matrix, denoted as H in (2.2), is carried out using a methodology based on training sequences. This requires the addition of a preamble preceding the data sequence emitted by each independent LED. Conversely, in ADR, the channel state information (CSI) is estimated by comparing a predetermined pilot sequence with the signals received. Utilising the LS method, the estimated channel matrix, $\hat{H}$, can be expressed as documented in [130]:

$$\hat{\mathbf{H}} = \underset{\mathbf{H}}{\operatorname{argmin}} \|\mathbf{Y}_{\mathrm{p}} - \mathbf{HP}\|^2 = (\mathbf{P}^T\mathbf{P})^{-1}\mathbf{P}^T\mathbf{Y}_{\mathrm{p}} \tag{3.1}$$

where $\mathbf{P}$ is the matrix $N_{\mathrm{t}} \times s$ with the sequence of s pilot bits transmitted from each transmitter and $\mathbf{Y}_{\mathrm{p}}$ is the pilot sequences received at all PDs and $\|.\|$ denotes the norm.

3.2.1.2 Signal Detection with Zero-forcing Approach

Upon estimating the CSI, the intended data stream can be decoded from all PDs. Given the presence of multiple transmitters, the signal received at each PD experiences interference from signals emitted by adjacent LEDs. This interference needs to be eliminated to accurately decode the intended signal. The ZF method is utilised across all ADR types using an estimated channel matrix. The detected signals are presented as follows [131]:

$$\hat{x} = WY \tag{3.2}$$

where the weight matrix W is the pseudo-inverse of the estimated channel matrix, $\hat{H}$, given by:

$$W = (\hat{H}^T\hat{H})^{-1}\hat{H}^T \tag{3.3}$$

It is important to recognise that this could lead to increased noise. Despite this, the method remains low complexity, without necessitating knowledge of noise variance. In this context,

the BER associated with on-off keying (OOK) modulation is expressed as follows [71]:

$$\mathrm{BER}_{\mathrm{OOK}} = Q\left(\mathcal{R}P_{\mathrm{t}}H_{\mathrm{l}}\sqrt{\frac{T_{\mathrm{s}}}{N_0}}\right) \tag{3.4}$$

where $Q(.)$ is the Gaussian Q function and P_{t} is the transmitted optical power. H_{l} is the channel gain of a point-to-point communication link. T_{s} represents the duration of the symbol in seconds and N_0 denotes the density of the power spectrum that can be obtained from the variance of the noise divided by the bandwidth of the noise B_{n} as $\sigma_{\mathrm{n}}^2/B_{\mathrm{n}}$. This formulation can be extended to the MIMO systems by incorporating the channel matrix according to equations (3.1) through (3.3). The analytical expression for BER with ZF is determined as follows:

$$\mathrm{BER}_{\mathrm{ZF}(j)} = Q\left(\frac{\mathcal{R}P_{\mathrm{t}}}{N_{\mathrm{t}}\|W_j\|}\sqrt{\frac{T_{\mathrm{s}}}{N_0}}\right) \qquad j = 1, 2, ..., N_{\mathrm{t}}. \tag{3.5}$$

where W_j is the j_{th} row of the pseudo-inverse of the channel matrix $\hat{H}$. The emitted power of each LED is considered to be uniform. To compensate for the increase in transmitted power that results from the deployment of multiple light sources, P_{t} is normalised with respect to N_{t}.

3.2.1.3 Signal Detection with Maximum-likelihood Approach

The ML detection technique is also considered an alternative to ZF. In the ML technique, the Euclidean distance is calculated between the received signal vector, $\mathbf{Y}$ and all possible received signals, $\mathbf{HX}$. The transmitted signal vector is detected by finding the minimum distance as [132]:

$$\hat{\mathbf{X}}_{\mathrm{ML}} = \underset{\mathbf{X}}{\mathrm{argmin}}\|\mathbf{Y} - \mathbf{HX}\|^2 \tag{3.6}$$

The BER of the ML receiver can be obtained from pairwise error probability, which is the error probability between a transmitted signal vector $\mathbf{X}_{m1}$ and a received signal vector $\mathbf{X}_{m2}$. Thus, pairwise error probability ($\mathbf{X}_{m1} \rightarrow \mathbf{X}_{m2}$), given the knowledge of the j_{th} column of the channel matrix $\mathbf{H}_j$ can be derived as [133]:

$$\begin{aligned} \mathrm{PEP}_{\mathrm{ML}(j)} &= \mathrm{PEP}(\mathbf{X}_{m1} \rightarrow \mathbf{X}_{m2} | \mathbf{H}_j) \\ &= Q\left(\frac{\Re}{2}\sqrt{\frac{T_\mathrm{s}}{N_0}\|\mathbf{H}_j(\mathbf{X}_{m1} - \mathbf{X}_{m2})\|^2}\right) \\ & j = 1, 2, ..., N_\mathrm{t}. \end{aligned} \tag{3.7}$$

where $Q(.)$ is the Gaussian Q-function. T_s is the duration of the symbol in seconds and N_0 is the density of the power spectrum. The analytical BER of SMP using ML can be approximated by the union-bound method using the pairwise error probability as:

$$\begin{aligned} \mathrm{BER}_{\mathrm{ML}(j)} \approx \frac{1}{2}\sum_{m1=1}^{M}\sum_{m2=1}^{M} \mathrm{d}_\mathrm{H}(b_{m1}, b_{m2})\mathrm{PEP}_{\mathrm{ML}(j)} \\ j = 1, 2, ..., N_\mathrm{t}. \end{aligned} \tag{3.8}$$

where the modulation order, M = 2 for OOK. $\mathrm{d}_\mathrm{H}()$ is the Hamming distance and b_m represents the possible M bit assignments of the signal vector $\mathbf{X}_m$.

3.2.2 Receive Diversity Techniques

Receive diversity techniques are applied to improve communication reliability [107, 134, 135]. In the multi-cell scenario considered in this chapter, each LED transmitter transmits signals to users in the LED cell, and signals from neighbouring cells constitute ICI when the coverage between cells overlaps each other, as illustrated in Fig. 3.2. The approaches of SC, EGC, and

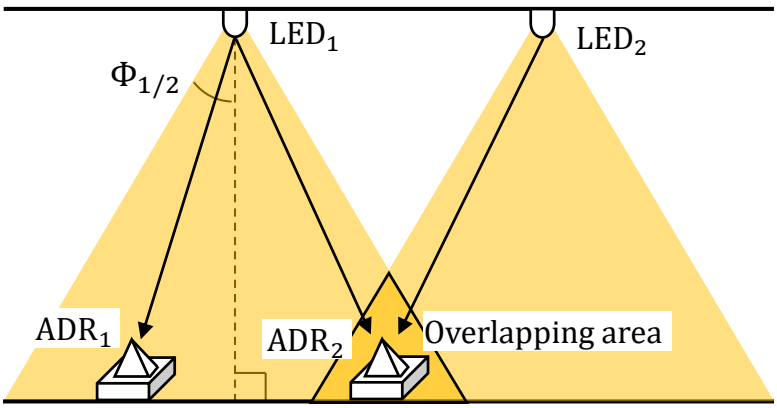

Figure 3.2: *Coverage area with two LED transmitters.*

MRC applied to the multi-cell scenario are concisely introduced and encapsulated in Table 3.1. Additionally, the BER formulation for these combining methods is included.

Table 3.1: *SINR in multi-cell scenario under SC, EGC and MRC.*

Techniques	SINR in a multi-cell
SC	$\gamma_{\mathrm{SC},j}^{\mathrm{Multi}} = \max_j(\mathrm{SINR}_{ij})$
EGC	$\gamma_{\mathrm{EGC},j}^{\mathrm{Multi}} = \frac{\sum_{i=1}^{N_\mathrm{r}}(\mathcal{R}h_{ij}P_\mathrm{o})^2}{\sum_{i=1}^{N_\mathrm{r}}(\sigma_{n,i}^2+\sum_{j'=1,j'\neq j}^{Nt}(\mathcal{R}h_{ij'}P_\mathrm{o})^2)}$
MRC	$\gamma_{\mathrm{MRC},j}^{\mathrm{Multi}} = \frac{\sum_{i=1}^{N_\mathrm{r}}(\mathcal{R}w_{ij}h_{ij}P_\mathrm{o})^2}{\sum_{i=1}^{N_\mathrm{r}}(w_{ij}^2\sigma_{n,i}^2+\sum_{j'=1,j'\neq j}^{Nt}(\mathcal{R}w_{ij'}h_{ij'}P_\mathrm{o})^2)}$

3.2.2.1 Selection Combining

In SC, the PD$_i$ with the highest SINR amongst the SINRs of all PDs is selected. Thus, the output SINR of SC for the multi-cell scenario, $\gamma_{\mathrm{SC},j}^{\mathrm{Multi}}$, is given as [20, 22]:

$$\gamma_{\mathrm{SC},j}^{\mathrm{Multi}} = \max_j(\mathrm{SINR}_{ij}) \tag{3.9}$$

$$\mathrm{SINR}_{ij} = \frac{(\mathcal{R}h_{ij}P_\mathrm{o})^2}{\sigma_{n,i}^2 + \sum_{j'=1,j'\neq j}^{Nt}(\mathcal{R}h_{ij'}P_\mathrm{o})^2} \tag{3.10}$$

where $\sum_{j'=1,j'\neq j}^{Nt}(\mathcal{R}h_{ij'}P_\mathrm{o})^2$ is the electrical power of ICI of all LEDs in interfering cells, $P_\mathrm{o} = P_\mathrm{t}/N_\mathrm{t}$ is the normalised optical power transmitted by the LED$_j$, and $\sigma_{n,i}^2$ is the variance of the noise in the PD$_i$. This is made up of the variance of the shot noise $\sigma_{\mathrm{shot},i}^2$ and the thermal noise $\sigma_{\mathrm{thermal},i}^2$ that are given by [24]:

$$\begin{cases} \sigma_{\mathrm{shot},i}^2 = 2q(\mathcal{R}P_j + I_\mathrm{bg}I_2B_\mathrm{n}) \\ \sigma_{\mathrm{thermal},i}^2 = 8\pi k_\mathrm{B}T\eta AB_\mathrm{n}^2(\frac{I_2}{G} + \frac{2\pi\Gamma}{g_\mathrm{m}}\eta AI_3B_\mathrm{n}) \end{cases} \tag{3.11}$$

where q is the charge of an electron and P_j =$P_\mathrm{o}\sum_{j=1}^{N_\mathrm{t}}h_{ij}$ is the total optical power received from all LED transmitters. I_bg is the background noise current; I_2 is the noise bandwidth factor; and B_n is the equivalent noise bandwidth. For the thermal noise parameters, k_B is the Boltzmann constant and T is the absolute temperature. η is PD fixed capacitance per unit area; G is the open-loop gain; Γ is the field effect transistor (FET) channel noise factor; g_m is the

FET trans conductance; I_3 = 0.0868. In this analytical investigation, the parameters are set as follows [71, 75]: $q = 1.6e^{-19}$ C, $I_{\mathrm{bg}} = 5100$ μA, $I_2 = 0.562$, $T = 298$ K, $\eta = 112$ pF/cm^2, $G = 10$, $\Gamma = 1.5$, $g_{\mathrm{m}} = 30$ mS.

3.2.2.2 Equal Gain Combining

The EGC method integrates signals from all PDs, assigning them an equal weight. The output SINR for the multi-cell scenario by EGC, $\gamma_{\mathrm{EGC},j}^{\mathrm{Multi}}$ is [20]:

$$\gamma_{\mathrm{EGC},j}^{\mathrm{Multi}} = \frac{\sum_{i=1}^{N_{\mathrm{r}}} (\mathcal{R} h_{ij} P_{\mathrm{o}})^2}{\sum_{i=1}^{N_{\mathrm{r}}} (\sigma_{n,i}^2 + \sum_{j'=1, j' \neq j}^{Nt} (\mathcal{R} h_{ij'} P_{\mathrm{o}})^2)} \tag{3.12}$$

3.2.2.3 Maximum-Ratio Combining

The MRC method employs weights directly proportional to the received signal to calibrate the output of each PD. The output SINR of MRC for the multi-cell scenario $\gamma_{\mathrm{MRC},j}^{\mathrm{Multi}}$ becomes [20]:

$$\gamma_{\mathrm{MRC},j}^{\mathrm{Multi}} = \frac{\sum_{i=1}^{N_{\mathrm{r}}} (\mathcal{R} w_{ij} h_{ij} P_{\mathrm{o}})^2}{\sum_{i=1}^{N_{\mathrm{r}}} (w_{ij}^2 \sigma_{n,i}^2 + \sum_{j'=1, j' \neq j}^{Nt} (\mathcal{R} w_{ij'} h_{ij'} P_{\mathrm{o}})^2)} \tag{3.13}$$

where w_{ij} is the weight calculated by transposing the gain of the correspondence channel, h'_{ij} as in [24].

3.2.2.4 Analytical BER Equation

In a VLC-MIMO system, the BER for the OOK modulation technique can be determined by the output SINR through the application of three different receive diversity techniques as indicated by [136]:

$$\mathrm{BER}_{\mathrm{OOK}} = Q\left(\sqrt{\gamma}\right) \tag{3.14}$$

where $Q(a) = \frac{1}{\sqrt{2\pi}} \int_a^{\infty} \exp(-\frac{t^2}{2})\, dt$ is the Gaussian Q-function. γ is the output SINR of the VLC system with each receive diversity technique.

3.3 Angular Diversity Receiver

In this section, the configurations for ADR considered in the analytical framework of this chapter are described within a three-dimensional coordinate system. The four types of ADR that are analysed are identified as SP, SF, HP, and HF, depending on the number and arrangement of PDs, as illustrated in Fig. 3.3. These ADR shapes with different number of PDs are examined because they are typically considered in the literature reviewed in 2.4.1. The greater number of PDs in an ADR makes implementation difficult due to circuit size, complexity and cost. The positions of PDs located on the top and side of ADR are shown in Fig. 3.4. Each PD is situated on every side of the ADR at a distance $r = 3$ cm from the centre of the X-Y plane, and at an elevation of $r/2$. In the case of the frustum ADRs, an additional top PD is placed r above the centre of the ADR, orientated directly upward. The azimuth angle for PD_i is determined by [21]:

$$\delta^{i}_{\mathrm{PD}} = \begin{cases} \frac{2(i-1)\pi}{N_{\mathrm{r}}} + \delta_{\mathrm{R}}, & \text{for} \quad \mathrm{SP},\ \mathrm{HP} \\ \frac{2(i-1)\pi}{N_{\mathrm{r}}-1} + \delta_{\mathrm{R}}, & \text{for} \quad \mathrm{SF},\ \mathrm{HF} \end{cases} \tag{3.15}$$

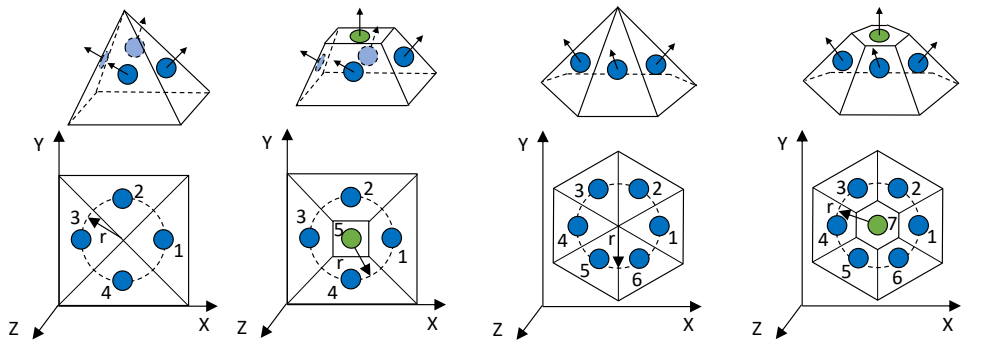

Figure 3.3: *The ADR configurations considered in this analytical study.*

where δ_{R} is the ADR rotation angle in the X-Y plane. Therefore, the position coordinates of PD_i can be represented by:

$$\begin{bmatrix} x^i_{\mathrm{PD}} \\ y^i_{\mathrm{PD}} \\ z^i_{\mathrm{PD}} \end{bmatrix} = \begin{cases} X_{\mathrm{r}} + r\cos\delta^i_{\mathrm{PD}} \\ Y_{\mathrm{r}} + r\sin\delta^i_{\mathrm{PD}} \quad \text{for side PD} \\ 1 + \frac{r}{2} \end{cases}$$
$$\begin{bmatrix} x^i_{\mathrm{PD}} \\ y^i_{\mathrm{PD}} \\ z^i_{\mathrm{PD}} \end{bmatrix} = \begin{cases} X_{\mathrm{r}} \\ Y_{\mathrm{r}} \quad \text{for top PD} \\ 1 + r \end{cases} \tag{3.16}$$

In (2.4), the distance d_{ij} is derived from the relative geometric positions of LED_j and PD_i, as illustrated in Fig. 2.3, and is determined by:

$$d_{ij} = \sqrt{(x^i_{\mathrm{PD}} - x^j_{\mathrm{LED}})^2 + (y^i_{\mathrm{PD}} - y^j_{\mathrm{LED}})^2 + (z^i_{\mathrm{PD}} - z^j_{\mathrm{LED}})^2} \tag{3.17}$$

The angle between LED_j and PD_i and the normal vectors, θ_{ij} and φ_{ij} depicted in Fig. 2.3 are derived from the inverse of $\cos\theta_{ij}$ and $\cos\varphi_{ij}$, which are calculated from the dot product of the vector p_i and n_i and the vector l_j and n_j shown as [22]:

$$\cos\theta_{ij} = \frac{\langle p_i, n_i\rangle}{\|p_i\|\|n_i\|}, \qquad \cos\varphi_{ij} = \frac{\langle l_j, n_j\rangle}{\|l_j\|\|n_j\|} \tag{3.18}$$

where p_i, l_i and n_j are the PD_i vector relative to the LED_j, the LED_j vector relative to the PD_i

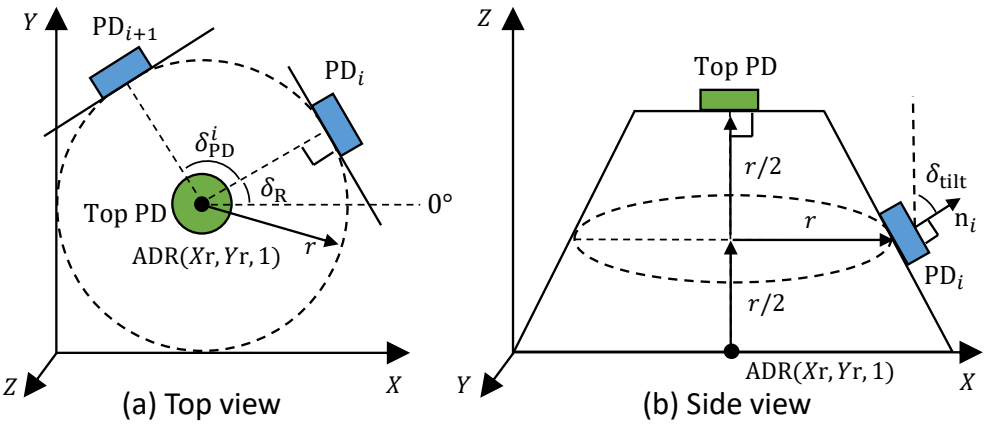

Figure 3.4: *Coordinates of the PDs in the ADR (a) top view and (b) side view.*

and the LED$_j$ normal vector, respectively. $\langle . \rangle$ denotes the dot product. Normal vector of PD$_i$ in three-dimensions can be obtained using PD$_i$ azimuth angle δ^i_{PD} and tilt angle δ^i_{tilt} as [24]:

$$n_i = \begin{bmatrix} \cos\left(\delta^i_{\mathrm{PD}}\right) \sin\left(\delta^i_{\mathrm{tilt}}\right) \\ \sin\left(\delta^i_{\mathrm{PD}}\right) \sin\left(\delta^i_{\mathrm{tilt}}\right) \\ \cos\left(\delta^i_{\mathrm{tilt}}\right) \end{bmatrix} \tag{3.19}$$

Therefore, by applying (3.15)-(3.19), the line-of-sight (LOS) channel gain h_{ij}^{Los} in (2.4) can be modelled. Similarly, the parameters for the non-line-of-sight (NLOS) channel gain h_{ij}^{Nlos} in (2.5) can be derived following the same methodology.

3.4 Results and Discussion

The VLC-MIMO system's performance is analysed based on the link geometry discussed above, with parameters detailed in Table 3.2. Commercially available LEDs typically operate within bandwidths in the MHz range [71], leading to the selection of a symbol duration, T_{s}, of 1 μs, alongside a corresponding noise bandwidth, B_{n}, of 1 MHz. The tilt angle of the PD, denoted as δ_{tilt} and depicted in Fig. 3.4b, influences ADR performance. Optimal performance is achieved when the channel gain from the desired LED is maximised whilst minimising co-channel interference (CCI). This optimal tilt angle determination is discussed in Section 3.4.1. Furthermore, the ADR rotation angle is pivotal for performance, as it alters the channel gain in (2.4) and (2.5). In the SMP application, performance evaluation for each ADR is conducted at specific rotation angles to observe CCI effects. In addition, the received signal-to-noise ratio (SNR) assesses the SMP techniques' effectiveness, considering the geometry of the link. Receive diversity techniques are evaluated through the Monte Carlo (MC) method to determine the average performance of δ_{R}. In every computation, the ADR rotation angle δ_{R} is drawn from uniformly distributed pseudo-random integers within the range of 0° to 360°, as referenced in [22]. The position of a single reflective point is randomly determined near the centre of each wall using a truncated normal distribution.

Table 3.2: *SIMULATION PARAMETERS*

Room parameters	Values [References]
Room dimensions (L_x, L_y, L_z)	(4 m, 4 m, 3 m) [18]
Number of LEDs N_{t}	4 [18, 19, 21–24]
LEDs coordinates (X_i, Y_i)	(1, 1), (1, 3), (3, 1), (3, 3) [23]
Reflective area A_{r}	1 cm^2 [19, 21]
Reflective coefficient ρ_{k}	0.8 [19, 21]
LED transmitter parameters	**Values [References]**
LEDs height	3 m [18, 19, 22, 24]
LEDs elevation angle	180° [21]
LEDs semi half angle $\Phi_{1/2}$	45° [21]
Average transmitted power P_{t}	1 W [19]
ADR receiver parameters	**Values [References]**
ADR height Z_{r}	1 m [19]
Area of PD A	1 cm^2 [18, 24]
Number of PDs N_{r}	$4, 5, 6, 7$
PDs responsivity $\mathcal{R}$	1 A/W [71]
PDs half angle FOV Ψ	30° [19, 24]
ADR elevation angle	0° [18, 19, 21–24]

3.4.1 Optimal Tilt Angle

In order to analyse the optimal tilt angle, the square and hexagonal geometries of the four ADRs being examined are treated independently due to their geometric differences. The tilt angle, denoted as δ_{tilt}, of the PD influences the ADR's performance. The performance is subject to tilt angle since even small angular deviations significantly change the incident angle on PD, leading to noticeable variations in channel gain. The ideal tilt angle is achieved when the channel gain from the desired LED, h_{iDj}, is maximised, whilst simultaneously minimising CCI, thereby enhancing error performance. As depicted in Fig. 3.5, the vertical layout of the room geometry is illustrated. The distinct ADR types result in varied link geometries within the system. The optimal angle can shift as the ADR moves; nonetheless, the optimal angle is determined at the central position since the ADR under study cannot be reconfigured.

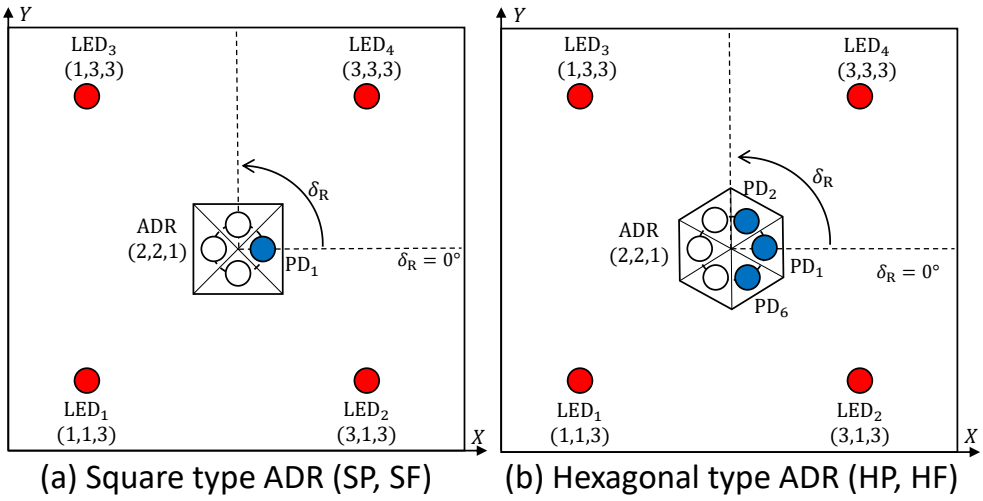

Figure 3.5: *A vertical view of the room geometry of the square type (a) and hexagonal type (b) ADR.*

3.4.1.1 Square type ADR (SP, SF)

In Fig. 3.5a, PD_1 is observed to rotate from 0° to 90°, during which CCI may emerge for certain values of δ_{R}. Identifying the optimal tilt angle becomes crucial to minimise CCI amongst adjacent LEDs across the range of δ_{R}. The optimal tilt angle, designated as $\delta_{\text{tilt}}^{\text{optimal}}$ for PD_i, is determined by maximising the channel gain from the desired LED, h_{iDj}, as follows:

$$\delta_{\text{tilt}}^{\text{optimal}} = \{ \max_{\delta_{\text{tilt}}, \delta_{\text{R}}} (h_{iDj}),\ \min_{\delta_{\text{R}}} \sum_{\delta_{\text{R}}=0^\circ}^{90^\circ} \sum_{k \neq D_j}^{N_{\text{t}}-1} h_{ik} \} \tag{3.20}$$

Using (3.20), the optimal tilt angle that optimises the SINR in this scenario is determined to be 45°. Fig. 3.6 illustrates the maximum channel gain, h_{1Dj}, for PD_1, alongside the combined CCI components across a range of δ_{R} from 0° to 90°. It is evident that the optimal angle derived from (3.20) does not coincide with the zenith of h_{1Dj}, occurring instead where h_{1Dj} is maximised and condition $\sum_{\delta_{\text{R}}=0^\circ}^{90^\circ} \sum_{k \neq D_j}^{N_{\text{t}}-1} h_{ik} = 0$ is satisfied. When aiming to minimise CCI, the optimal tilt is 45°, as this results in a nullified CCI sum, which is graphically supported by the plot in Fig. 3.6. The discrepancy in h_{1Dj} between 45° and the peak h_{1Dj} at 35° is just 2.3% or 0.1 dB. Therefore, the optimal tilt can minimise the impact of CCI with only 0.1 dB reduction in SNR. Given the symmetrical design of the considered ADRs, the optimal tilt angle derived for PD_1 is applicable to all side-mounted PDs.

3.4.1.2 Hexagonal type ADR (HP, HF)

As illustrated in Fig. 3.5b, the optimal $\delta_{\text{tilt}}^{\text{optimal}}$ for the HP and HF ADRs does not require an identical constraint to mitigate the impact of CCI. This category of ADR has more than three degrees of freedom ($N_{\text{r}} - N_{\text{t}} + 1$) due to a higher number of side-mounted PDs in comparison to the LEDs. Consequently, the optimal tilt angle for a hexagonal ADR is dependent solely on channel gain, allowing the simplification of (3.20) to:

$$\delta_{\text{tilt}}^{\text{optimal}} = \max_{\delta_{\text{tilt}}, \delta_{\text{R}}} (h_{iDj}) \tag{3.21}$$

Here, in the case of hexagonal-shaped ADRs, the optimal tilt angle $\delta_{\text{tilt}}^{\text{optimal}}$ is determined to be 35° applying (3.21), which aligns with the maximum value of h_{1Dj} as depicted in Fig. 3.6.

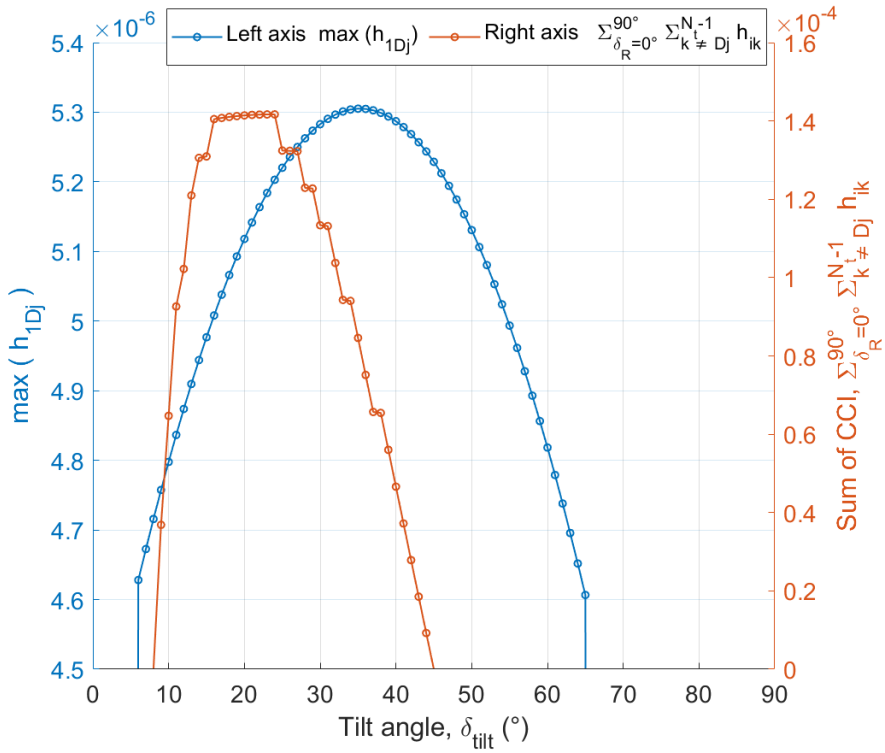

Figure 3.6: *max(h_{1Dj}) and sum of CCI* $\sum_{\delta_{\text{R}}=0^\circ}^{90^\circ} \sum_{k \neq D_j}^{N_{\text{t}}-1} h_{ik}$.

3.4.2 Performance Comparison using SMP Techniques

3.4.2.1 BER vs Rotation Angle

The BER performance of each ADR type is analysed against the ADR rotation angle. In this investigation, the evaluation is conducted using ML detection approach. Fig. 3.7 illustrates the BER against δ_{R} of the LED_1 (1, 1, 3) and the LED_2 (3, 1, 3) in the central position of the room. In the calculation, 10^8 bits are transmitted from each LED with a SNR of 116 dB and the BER is assessed in the range of δ_{R} from $0°$ to $90°$. Here, SNR is given by $(P_{\mathrm{t}}R)^2/\sigma_{\mathrm{n}}^2$, calculated based on channel gain and a noise equivalent power of 1 fW/$\sqrt{\mathrm{Hz}}$ for receivers. The SNR excludes channel gain to enable a fair comparison under identical conditions, since the channel gains of each link differ due to varying angles. The simulation curves are illustrated to align closely with the analytical ones. Due to symmetry in the room layout and ADRs, at the centre position, the BER curves for the other pair of LEDs and PDs at the central position are identical. It is observed that the performance of SP and SF surpasses the forward error correction (FEC) threshold of 3×10^{-3} for $\delta_{\mathrm{R}} < 1°$ and $\delta_{\mathrm{R}} > 89°$. The elevated BER beyond these intervals is due to CCI. The HP and HF provide better BER performance because they maintain BER below the FEC limit. At the centre position, the PD on the top of the frustum-type ADR does not operate because it cannot detect any signals arriving from outside its FOV.

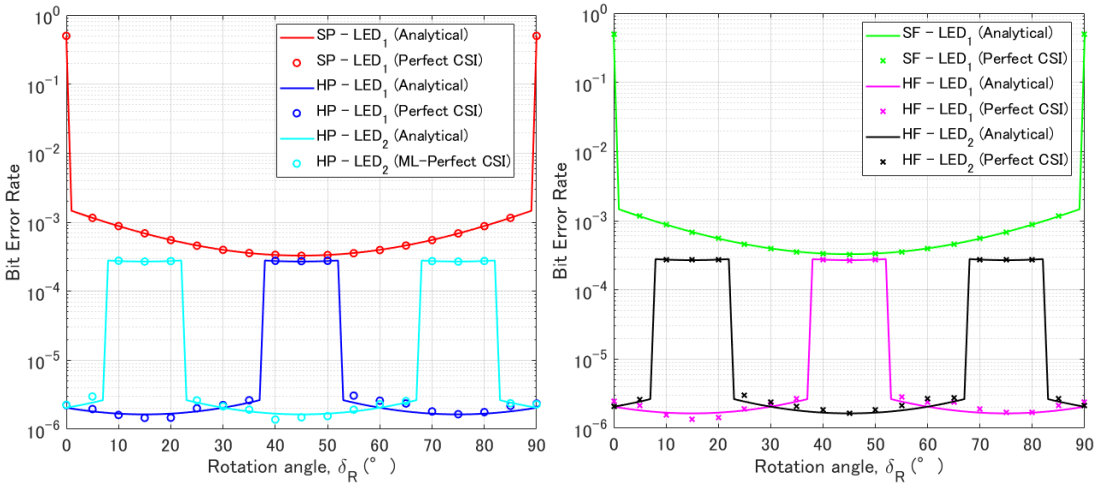

(a) *Pyramid type* **(b)** *Frustum type*

Figure 3.7: *BER vs rotation angle of ADR types at SNR 116 dB with ML detection.*

3.4.2.2 BER Performance vs SNR

The BER performance associated with various decoding techniques and ADR types is examined in relation to SNR when positioned centrally and underneath a cell equipped with a LED transmitter. This comparison involves simulations based on the transmission of 10^7 bits, using both perfect and estimated CSI. Performance differences of the decoding techniques between the ZF and ML methods are also analysed. In Fig. 3.8, BER against SNR for LED_1 is shown at a rotation angle of $\delta_{\text{R}} = 30°$, with the HF ADR located at (2, 2, 1). The BER obtained with perfect CSI using ML requires approximately 1 dB less SNR compared to ZF to achieve the desired BER of the FEC limit. Additionally, a penalty SNR of 2-3 dB is observed using the estimated CSI compared to perfect CSI. Fig. 3.9 presents the BER curves of individual streams versus SNR below LED_1 using estimated CSI. At the location (1, 1, 1), the SP with ZF is limited to receiving one stream from LED_3, whilst SP with ML can detect streams from LED_2, LED_3, and LED_4 due to the enhanced robustness of ML in CCI settings. SF ADR with ZF can support two streams, whilst SF ADR using ML detects all four streams. The HP ADR with ZF and ML supports the same number of streams. The BER of LED_3 with ZF is in agreement with

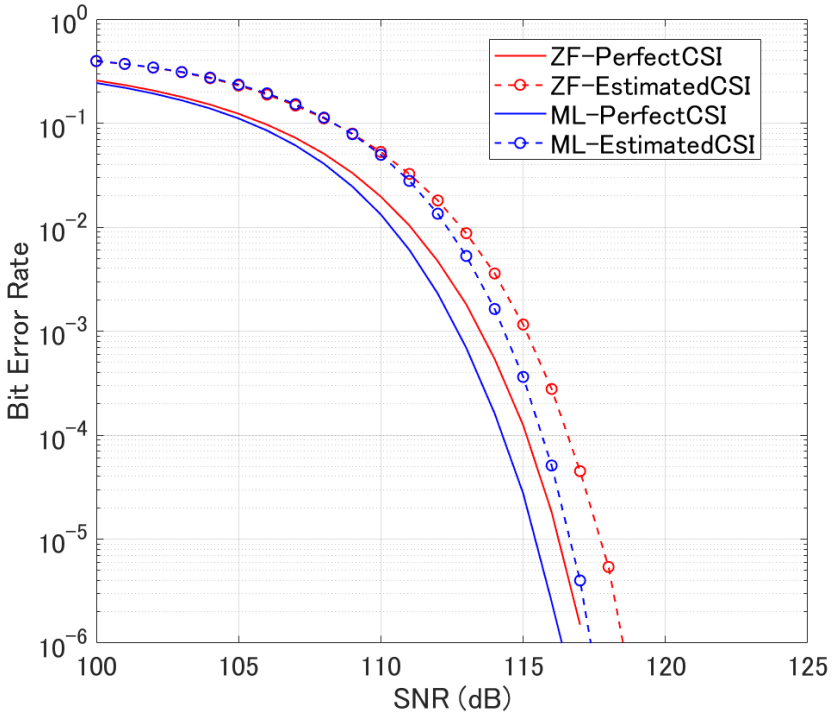

Figure 3.8: *BER vs SNR of LED_1 with rotation angle $\boldsymbol{\delta_{\text{R}} = 30°}$ of the HF ADR in the centre of the room.*

that of ML because this stream is not influenced by CCI, whilst the BER curves for LED_2 and LED_4 with ZF require an additional SNR of 3-4 dB. Lastly, HF ADR can support data streams from all four LEDs regardless of detection techniques. The SNR requirement to achieve a BER of 3×10^{-3} using ZF is 111 dB for LED_1 compared to 133 dB for LED_4 with the biggest difference of 22 dB. On the other hand, the difference in the required SNR using ML is 21 dB with the SNR of 109 dB for LED_1 and 130 dB for LED_4.

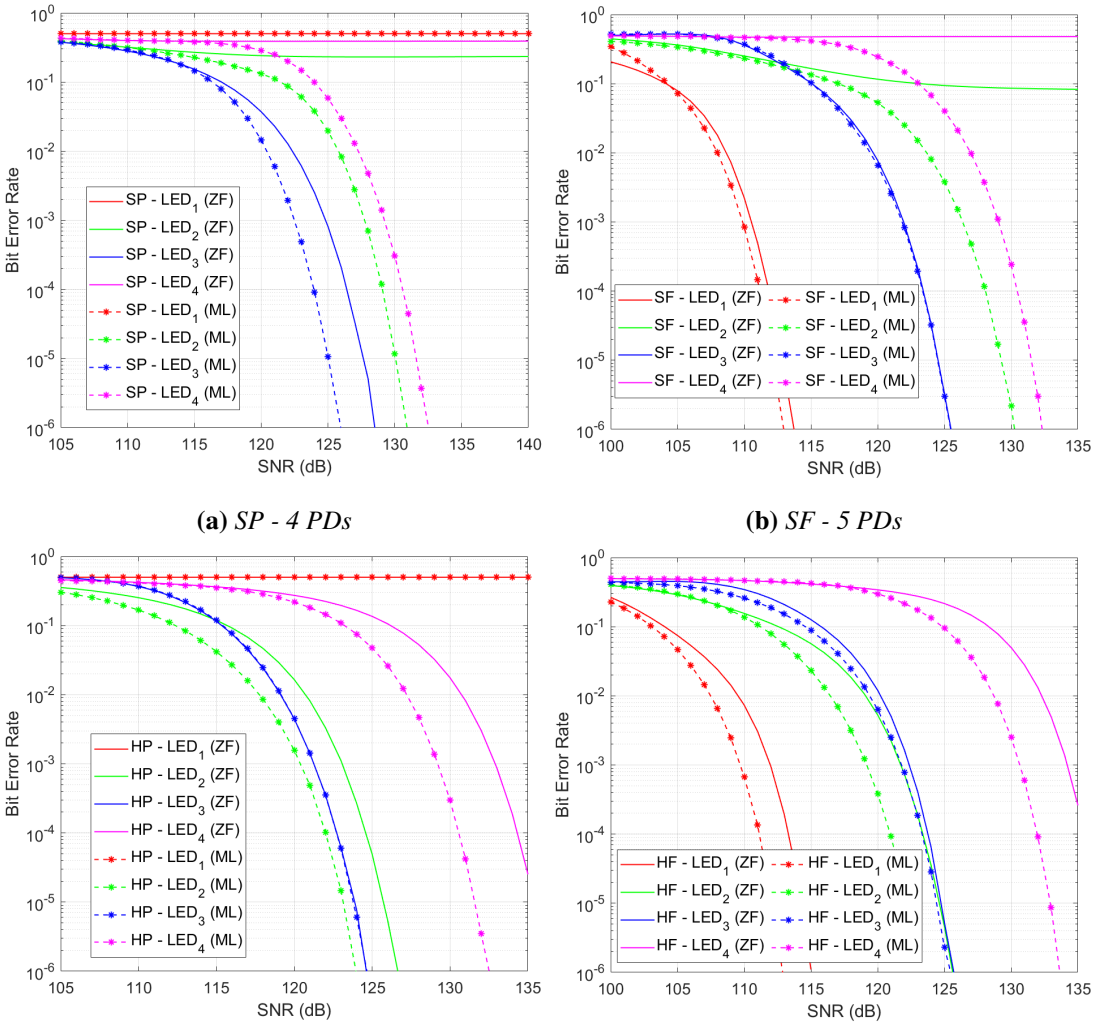

(a) *SP - 4 PDs* **(b)** *SF - 5 PDs*

(c) *HP - 6 PDs* **(d)** *HF - 7 PDs*

Figure 3.9: *BER vs SNR of each ADR type below LED_1 (1, 1, 1) with rotation angle $\delta_{\mathbf{R}} = \mathbf{30}^{\circ}$, (a) SP- 4 PDs, (b) SF- 5 PDs, (c) HP - 6 PDs and (d) HF - 7 PDs.*

3.4.2.3 Multi-stream Coverage Rate

The performance of different ADRs is evaluated based on their ability to support multi-stream coverage. This study examines performance fluctuation at multiple rotation angles. These ADRs are positioned in the X-Y plane at an altitude of 1 m. To determine the coverage rate for each stream, the BER with ML approach is calculated using the estimated CSI at the locations of the ADRs. The coverage rate is subsequently defined as

$$R_{\text{coverage}} = \frac{N_{\text{p}}}{N_{\text{total}}} \times 100 \quad [\%] \tag{3.22}$$

where N_{p} is the number of points at which a target BER of 3×10^{-3} can be achieved and N_{total} is the total number of points considered. The case study room is divided using a 5 cm

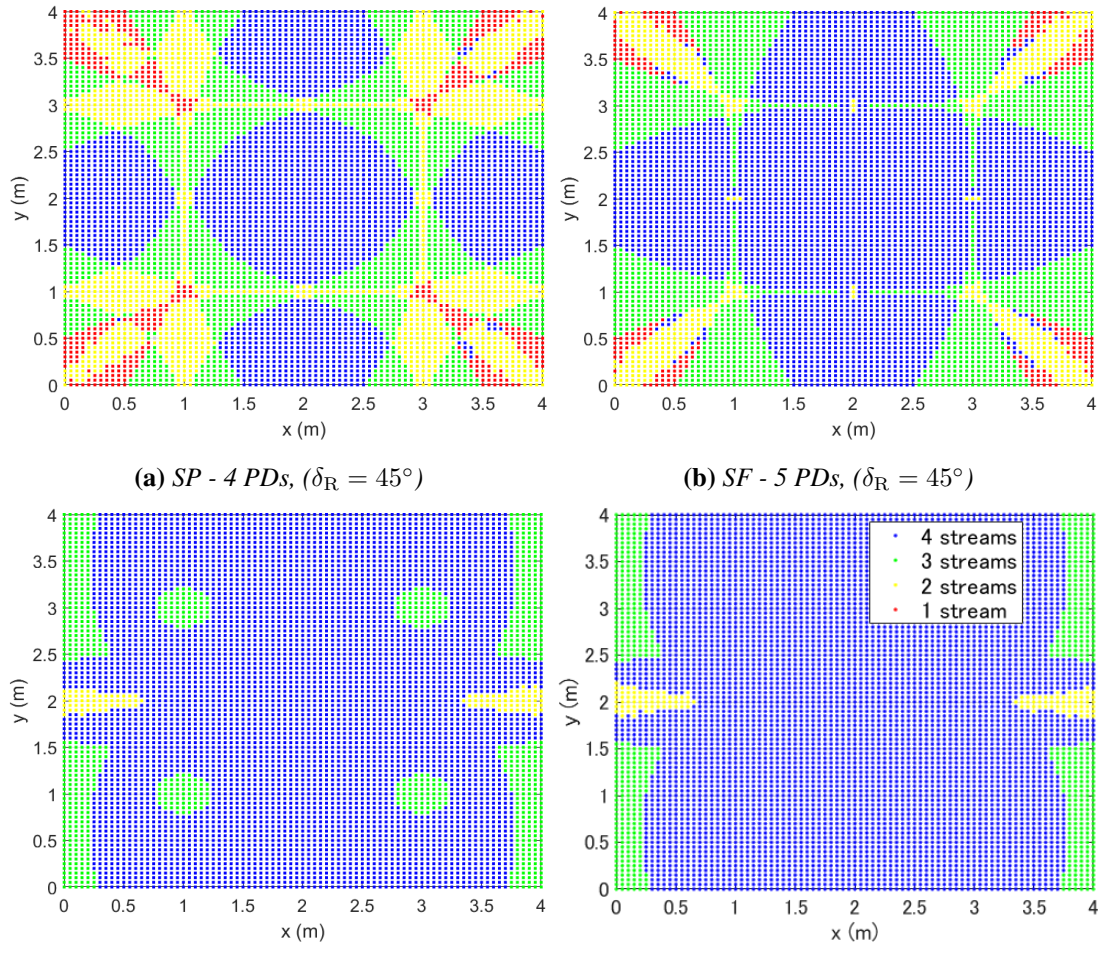

(a) *SP - 4 PDs, ($\delta_{\text{R}} = 45°$)*

(b) *SF - 5 PDs, ($\delta_{\text{R}} = 45°$)*

(c) *HP - 6 PDs, ($\delta_{\text{R}} = 0°$)*

(d) *HF - 7 PDs, $\delta_{\text{R}} = 0°$)*

Figure 3.10: *Coverage of each stream connected to the ADR.*

grid, resulting in $N_{\text{total}} = 6561$, composed of evenly distributed points on the X-Y plane. Fig. 3.10 illustrates the coverage of the number of streams supported by the ADR at each point in the grid, based on the noise variance derived from (3.11). The colour of each point on the grid denotes the number of streams accommodated within the target BER: a blue point signifies 4 supported streams; green, 3 supported streams; yellow, 2 supported streams; red, 1 supported stream; grey, 0 supported streams. As the number of PDs rises, areas supporting four streams expand. The HF type in Fig. 3.10d has the largest coverage area of four streams.

Table 3.3 presents the coverage rates for each type of ADR at different rotation angles as percentages. It can be seen that a greater number of PDs within an ADR results in higher coverage rates in four streams, whilst the frustum type maintains consistent performance at any angle. The HF ADR achieves approximately 88% with four streams at rotation angles δ_{R} of 0°, 15° and 30°. The HP also exhibits a stable coverage of around 84% with all streams. The hexagonal ADR is capable of supporting more than two streams at any position. In contrast, the coverage rates for the SP and SF fluctuate at the rotation angles δ_{R} of 0°, 15°, 30° and 45°. Specifically, at δ_{R} of 0°, the SP and SF cannot support any stream with a rate of 0. 08%. The SP ADR's rate of supporting four streams ranges from 29.20% to 46.84%, whilst the SF's rate varies from 49.76% to 66.90%.

Table 3.3: *Multi-stream coverage rates [%] of each ADR type at several rotation angles.*

ADR type	SP (4PDs)				SF (5PDs)				HP (6PDs)				HF (7PDs)			
δ_{R}	0°	15°	30°	45°	0°	15°	30°	45°	0°	15°	30°		0°	15°	30°	
Grey : 0 streams	0.08	0	0	0	0.08	0	0	0	0	0	0		0	0	0	
Red : 1 stream	0.26	0.23	0.96	2.16	0.24	0.18	0.90	0.66	0	0	0		0	0	0	
Yellow : 2 streams	31.52	15.62	5.80	21.26	5.35	4.47	0.55	4.16	1.72	0.61	1.77		1.86	0.59	1.87	
Green : 3 streams	33.76	54.95	61.70	29.74	44.57	35.79	32.50	28.29	15.00	13.78	15.00		11.03	10.49	11.03	
Blue : 4 streams	34.39	29.20	31.55	46.84	49.76	59.56	66.06	66.90	83.28	85.61	83.23		87.11	88.92	87.09	

3.4.3 Performance Comparison using Receive Diversity Techniques

In this comparison, the SINR distributions of each ADR type employing receive diversity techniques are investigated within a multi-cell environment. The case study room is segmented into a grid composed of uniformly spaced points, at 10 cm intervals on the X-Y plane. Performance is evaluated at each point of the grid at a height of 1 m. At every location, SINR is calculated using the three diversity combining methodologies described in expressions (3.9) - (3.13). The results are derived from a MC simulation, executed $N = 5000$ times to determine the average performance. The distribution is analysed with a box chart, highlighting statistical features; each chart is constructed from the SINR values across all grid positions. In addition, mean and variance statistics are displayed. The coverage performance is subsequently evaluated using the analytical BER equation in (3.14).

3.4.3.1 SINR Distribution in Multi-cell Scenario

ADR performances in the multi-cell scenario are presented. In the multi-cell scenario, the signals from neighbouring cells can be ICI as calculated in (3.9), (3.12) and (3.13). Fig. 3.11 shows the box chart of the SINR values of each type of ADR with the average and variance of the SINR values. In each box chart, the box shows the lower and upper quartiles with a blue line indicating the median value. Also, whiskers extend from outside the box towards the minimum and maximum value. An outlier is plotted if the value is more than 1.5 times the distance between the top and bottom of the box, the interquartile range, away from the top or bottom of the box. Amongst these three combining techniques, SF and HF show the best performance because the mean SINR is the highest at around 35 dB and the quartile range is the smallest from 35 to 38 dB although the number of outliers is largest. These two ADRs using SC have almost the same performance in the box chart, mean and variance values, meaning that two additional PDs on the side of HF have no performance benefits. The performance of SP and HP using SC is worse than that of frustum-type ADRs with a reduction of around 9 dB in the mean SINR value because these ADRs do not have PD on the top. It can also be seen that the median value is 2 dB higher than the mean value when SC is applied. Looking at the EGC technique, any type of ADR has the lowest mean SINR and a median value ranging from 6 to 8 dB. Although their variance is comparatively low with less than 25, the highest SINR of each ADR is less than 17 dB. Therefore, it can be said that the SINR values using EGC are distributed around the lowest mean value. Considering the MRC technique, the mean SINR

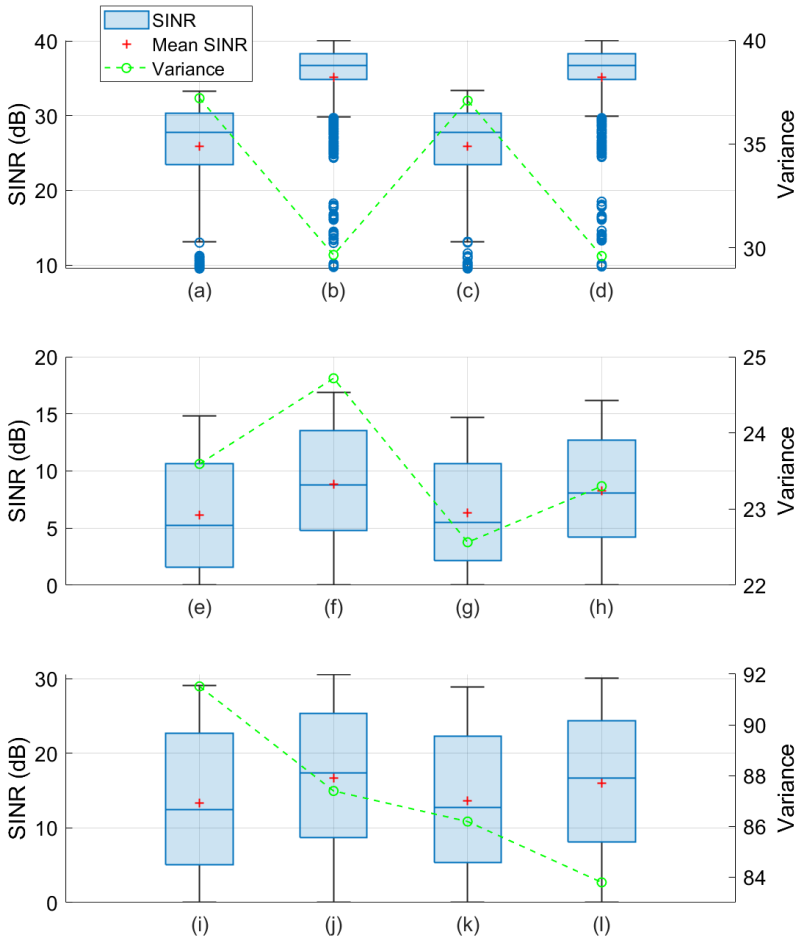

Figure 3.11: *SINR box chart, mean and variance in the multi-cell scenario: (a) SP with SC, (b) SF with SC, (c) HP with SC, (d) HF with SC, (e) SP with EGC, (f) SF with EGC, (g) HP with EGC, (h) HF with EGC, (i) SP with MRC, (j) SF with MRC, (k) HP with MRC, (l) HF with MRC.*

and median value almost doubled compared to the EGC technique due to SINR improvement from approximately 15 dB to 30 dB. Therefore, the variance becomes the largest amongst these three techniques within the range of 84 to 92. In EGC and MRC it is seen that any ADR may suffer from ICI because the lowest SINR is 0 dB. Fig. 3.12 shows the SINR distribution of the SP and SF type in the multi-cell scenario using SC, EGC and MRC techniques. It has already been shown that the hexagonal type has no benefit compared to the square type ADR, as there is no additional diversity gain in this configuration. Using the SC technique, a stable SINR is maintained even if the ADR is in the middle of the cells. This is because it can obtain the highest SINR from signals in any cell, as in (3.9), and SC is less affected by ICI. The SINR

value of SP and SF with SC reaches a maximum under LED cells. This then decreases to 10 dB towards the edges of the room. It can be shown that the SINR of EGC and MRC degrades to 0 dB by ICI near the middle of the cell regardless of the ADR types because the ADR can receive signals from neighbouring cells. Considering the pyramid-type ADR, the SINR directly beneath an LED, using EGC and MRC also decreases to 0 dB as the PD orientation means they cannot align the LOS of the LED cell.

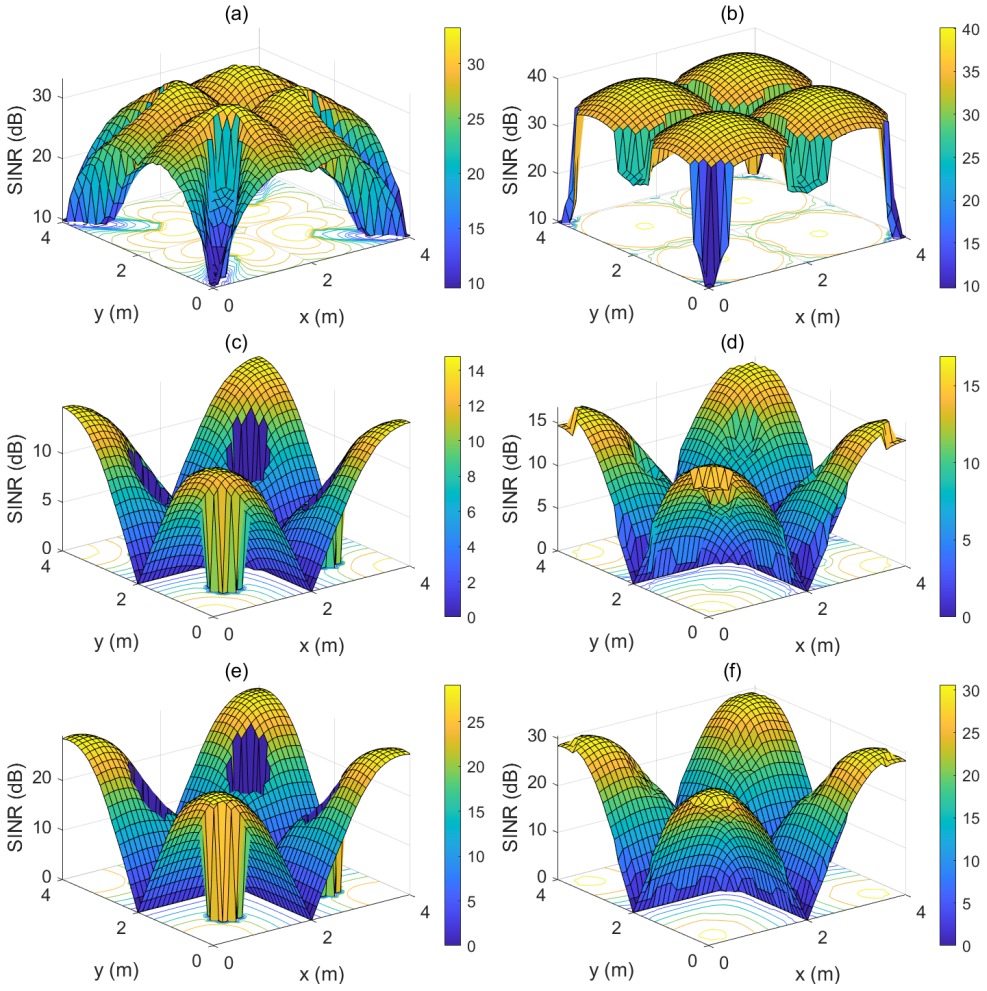

Figure 3.12: *SINR distribution in the multi-cell scenario: (a) SP with SC, (b) SF with SC, (c) SP with EGC, (d) SF with EGC, (e) SP with MRC, (f) SF with MRC.*

3.4.3.2 Coverage Rates Comparison

The coverage rates of the multi-cell scenario are compared using the same method as described in the SMP results section above 3.4.2.3. The coverage rate defined in (3.22) is considered

with $N_{\text{total}} = 1681$ for this comparison. Table 3.4 shows the coverage rates of all ADR types considered using three combining techniques for the multi-cell scenario. The ADR coverage rate for SC is shown to be 100%, which shows the rates calculated using a threshold of 1×10^{-6} in addition to the FEC limit. The SF-shaped ADR using SC has the widest coverage with 98.39% for 1×10^{-6}. It can be seen that the coverage rates of the hexagonal-type ADR do not improve compared to that of the square-type ADR because additional PDs contribute to an increase in noise rather than an increase in signal power. For EGC and MRC, the coverage rates are much worse than those of SC due to ICI. The highest coverage rates of EGC and MRC reach around 50% and 75%, respectively, when SF is applied. The results indicate that the higher number of PDs in the ADR system does not necessarily mean better performance in receive diversity applications. SC technique is the most promising in multi-cell scenarios due to the less influence of ICI. In the presence of ICI, both EGC and MRC fail to eliminate the interference component, leading to a degradation in the SINR and consequently affecting the BER. It can therefore be concluded that for the ADR performance of receive diversity in a multi-cell system, MRC, which is generally considered optimal, is not the most suitable candidate.

Table 3.4: *Coverage rates [%] of each ADR type using combining techniques: SC, EGC and MRC.*

Multi-cell	SP (4PDs)	SF (5PDs)	HP (6PDs)	HF (7PDs)
SC (FEC)	100	100	100	100
SC (10^{-6})	92.86	98.39	93.16	98.27
EGC	32.36	49.97	32.84	44.50
MRC	61.15	74.96	63.06	74.24

3.5 Summary

In this chapter, the ADR performance for the VLC-MIMO downlink systems in multi-cell scenarios was evaluated by simulation and analytical studies. Four different ADRs, SP, SF, HP and HF, were investigated for performance comparison. Two SMP schemes including ZF and ML, and three receive diversity techniques: SC, EGC and MRC were compared. SMP techniques were applied for capacity enhancement by handling multiple data streams, whilst receive diversity techniques were used for high communication reliability. Regarding SMP comparison,

the BER and coverage rates showed the best when the HF ADR, which has the largest number of PDs with seven, was applied due to diversity gain. In addition, SF and HF provide stable coverage rates at variable rotation angles. In terms of receive diversity techniques, the SINR distribution of the hexagonal-type ADR using SC showed the best because it is not affected by ICI. It was also shown that HP and HF ADRs, which have six PDs on the sides, did not provide any performance benefit compared to SP and SF types with four PDs on the sides. In contrast, EGC and MRC showed poorer performance as a result of increased noise levels by ICI.

In general, this chapter provides valuable insight into coverage performance in multi-cell VLC networks. The results obtained from various scenarios of an ADR system that uses SMP and receive diversity schemes can offer practical guidance for the application of ADR in VLC. Consequently, the theoretical verification presented in this chapter not only provides a solution to the coverage issue in VLC, but also serves as significant data when evaluating combinations of ADR and its related technologies.

Chapter 4
Design and Implementation of Angular Diversity Receiver for VLC-IoT System

4.1 Introduction

Although much of the research in visible light communication (VLC) for Internet of Things (IoT) explores the application of advanced technologies to improve performance, including data rate and reliability [137–140], these studies are predominantly based on theoretical validation or offline experiments. To validate the practical viability of VLC, it is essential to conduct demonstrations with fully integrated hardware systems. The limited number of previous literature on the practical implementation of VLC has focused on a variety of use cases, including IoT [85, 141, 142]. A successful demonstration requires a design that considers not only communication performance but also crucial factors such as size, cost, and power consumption, which in turn dictates the selection of the implementation hardware.

This chapter presents a single-cell VLC-based IoT (VLC-IoT) system using angular diversity receiver (ADR) through analytical and experimental studies. The purpose of the analytical study is to select the optimal type of ADR for the following experimental study. Performance using the same combining techniques as in Chapter 3 is analysed in a single-cell repetition coding scenario with multiple light emitting diode (LED) transmitters. The prototype design is tailored to IoT applications with constraints such as hardware resources, cost and size. Therefore, the target data rate is several Mbps using the commercial off the shelf components including LEDs and photodiodes (PDs). To provide a comprehensive performance comparison of a single-cell scenario, the ADR configurations that are modelled in Chapter 3 are considered. By selecting the optimal ADR type on the basis of the analytical results, a novel duplex VLC-IoT prototype is presented, showing a wide communication coverage using a prototyped ADR. The combining technique, equal gain combining (EGC), is applied to achieve a higher signal-to-noise ratio (SNR) with low complexity of implementation. Furthermore, real-time IoT sensor

data transmission is demonstrated.

The remainder of this chapter is organised as follows. The system model of a single-cell scenario and the proposed structure of the ADR system are discussed in Section 4.2 and Section 4.3; numerical and experimental results are presented in Section 4.4; and conclusions are drawn in Section 4.5.

4.2 A single-cell system model and related techniques

For analytical study, the system model of a single-cell scenario with N_{t} LED transmitters is considered using the same model in Chapter 3 as illustrated in Fig. 3.1. ADR configurations applied in this single-cell performance analysis are the same ADR models as described in Section 3.3.

4.2.1 Receive Diversity Techniques in a single-cell

The application of receive diversity techniques can enhance the SNR in single-cell configurations [134, 135], where all multiple LED transmitters convey identical data to users through the use of repetition coding. Signals can be combined when the ADR is within the collective coverage of the LED footprint, as shown in Fig. 3.2. Selection combining (SC), EGC, and maximum ratio combining (MRC) techniques are concisely introduced and presented in Table 4.1.

Table 4.1: *SNR in a single-cell scenario under SC, EGC and MRC.*

Techniques	SNR in a single-cell
SC	$\gamma_{\mathrm{SC}}^{\mathrm{Single}} = \max_i(\mathrm{SNR}_i)$
EGC	$\gamma_{\mathrm{EGC}}^{\mathrm{Single}} = \frac{\sum_{j=1}^{N_{\mathrm{t}}}\sum_{i=1}^{N_{\mathrm{r}}}(\mathcal{R}h_{ij}P_{\mathrm{o}})^2}{\sum_{i=1}^{N_{\mathrm{r}}}\sigma_{n,i}^2}$
MRC	$\gamma_{\mathrm{MRC}}^{\mathrm{Single}} = \frac{\sum_{j=1}^{N_{\mathrm{t}}}\sum_{i=1}^{N_{\mathrm{r}}}(\mathcal{R}w_{ij}h_{ij}P_{\mathrm{o}})^2}{\sum_{i=1}^{N_{\mathrm{r}}}w_{ij}^2\sigma_{n,i}^2}$

In the SC technique, the i_{th} PD, PD_i, with the highest SNR is chosen. The SNR output for the single-cell scenario, $\gamma_{\mathrm{SC}}^{\mathrm{Single}}$, can be derived using SNR_i, SNR in PD_i, as:

$$\gamma_{\mathrm{SC}}^{\mathrm{Single}} = \max_i(\mathrm{SNR}_i) \tag{4.1}$$

$$\mathrm{SNR}_i = \frac{\sum_{j=1}^{N_\mathrm{t}} (\mathcal{R} h_{ij} P_\mathrm{o})^2}{\sigma_{n,i}^2} \tag{4.2}$$

where $P_\mathrm{o} = P_\mathrm{t}/N_\mathrm{t}$ is the normalised optical power transmitted by the LED$_j$, and $\sigma_{n,i}^2$ is the noise variance in PD$_i$. This includes the variance of the shot noise $\sigma_{\mathrm{shot},i}^2$ and the thermal noise $\sigma_{\mathrm{thermal},i}^2$, which are explained in the previous section 3.2.2.1. Whilst the EGC method combines signals received from all PDs with equal weight, the MRC approach applies weights proportional to the received signal to adjust the output of each PD. The weight w_{ij} is derived from the transpose of the channel gain, denoted h'_{ij}, according to [24]. Consequently, the output SNR for EGC, $\gamma_{\mathrm{EGC}}^{\mathrm{Single}}$, and MRC, $\gamma_{\mathrm{MRC}}^{\mathrm{Single}}$, can be expressed as follows:

$$\gamma_{\mathrm{EGC}}^{\mathrm{Single}} = \frac{\sum_{j=1}^{N_\mathrm{t}} \sum_{i=1}^{N_\mathrm{r}} (\mathcal{R} h_{ij} P_\mathrm{o})^2}{\sum_{i=1}^{N_\mathrm{r}} \sigma_{n,i}^2} \tag{4.3}$$

$$\gamma_{\mathrm{MRC}}^{\mathrm{Single}} = \frac{\sum_{j=1}^{N_\mathrm{t}} \sum_{i=1}^{N_\mathrm{r}} (\mathcal{R} w_{ij} h_{ij} P_\mathrm{o})^2}{\sum_{i=1}^{N_\mathrm{r}} w_{ij}^2 \sigma_{n,i}^2} \tag{4.4}$$

4.3 Proposed ADR system structure

The concept of the bidirectional ADR system considered in this study is illustrated in Fig. 4.1. This system comprises access points (APs) positioned on the ceiling and user nodes (UNs) situated on the floor or tables. It establishes a bidirectional connection involving downlink (DL) via VLC and uplink (UL) through infrared (IR). As detailed in Section 4.2, these two APs function collectively as a single-cell. Consequently, any UN located within the overlapping region effectively integrates signals from these APs.

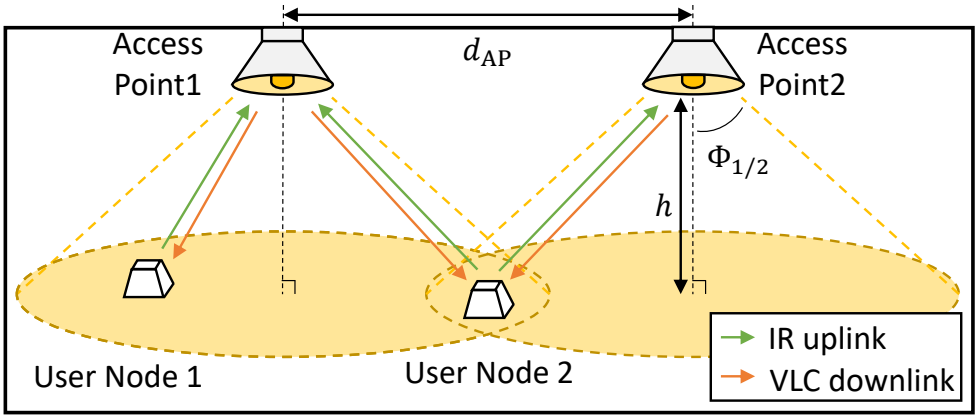

Figure 4.1: *Bidirectional ADR system concept with two APs as a single-cell.*

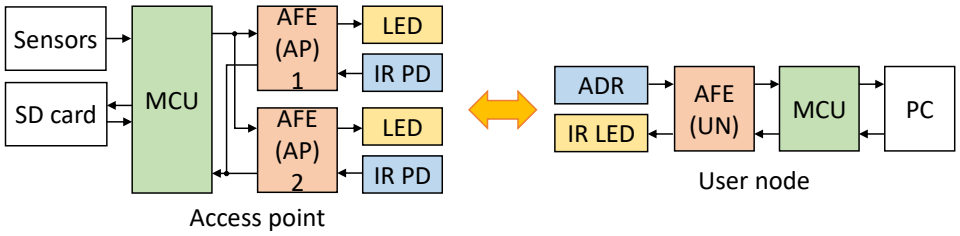

Figure 4.2: *Block diagram of the proposed system.*

The block diagram showing the design of the proposed transceiver is presented in Fig. 4.2. The transceivers of both the AP and UN configurations consist of an microcontroller unit (MCU), an analogue front end (AFE), white/IR LED, and ADR/IR PD. The MCU of the AP is outfitted with sensors that monitor light intensity, temperature, and humidity. The AP MCU processes these sensor data for DL transmission, as well as the information received from the UN. In addition, the AP includes a microSD card capable of storing sensor data. The AP is furnished with two transceivers, featuring an IR PD and a high-power white LED with a reflector, allowing it to additionally serve as a source of light in the room. Meanwhile, the UN MCU has the capability to send commands to the AP and to acquire sensor data.

For intercommunication, the AP and UN employ the straightforward on-off keying (OOK) modulation technique. The MCU implements the universal asynchronous receiver/transmitter (UART) communication protocol. This protocol for serial communication uses the non-return-to-zero OOK (NRZ-OOK) format and enables full duplex communication, with data rates modifiable up to two Mbps. Such communication speeds sufficiently meet the needs of VLC sensor networks, as the typical bandwidth of commercially available LEDs is in the MHz range [71]. Thus, the AFE transceiver in this chapter is built to support the UART protocol.

4.3.1 The Analogue Front End

This section describes the design of the AFE transceiver for both the AP and UN. The AFE is specially designed to maintain simplicity in implementing the ADR system. Fig. 4.3 illustrates the block diagram of the ADR transmitter AFE. The circuit's primary role is to drive the IR LED in the UN, whilst the AP drives the white LED. In the DL channel that uses visible light, the MCU UART pinout provides a signal to a circuit that acts as a voltage-controlled current source. This current directs the operation of the LED. For UL facilitated by an IR LED, the UN AFE incorporates an inverter circuit. This circuit ensures the IR LED deactivates when UN

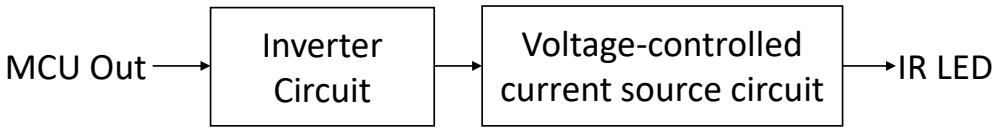

Figure 4.3: *Block diagram of ADR's transmitter AFE.*

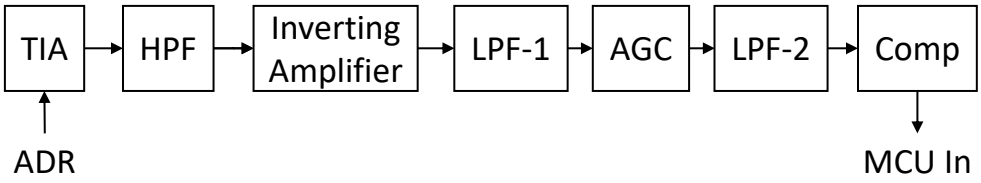

Figure 4.4: *Block diagram of ADR's receiver AFE.*

transmission is idle. In contrast, the inverter circuit is excluded in the AFE in the AP and the white LED remains continuously illuminated to denote its dual function as both an illumination and communication hub. Fig. 4.4 shows the block diagram of the ADR's receiver AFE, which includes a transimpedance amplifier (TIA), an inverting amplifier, automatic gain control (AGC), and a comparator. The low pass filter (LPF)/high pass filter (HPF) is configured as a passive first-order resistor-capacitor filter. Further discussion of TIA in the context of the ADR design will be presented in Section 4.3.2. In the UN AFE, the subsequent inverting amplifier amplifies the voltage signal, whilst in the AP AFE, an non-inverting amplifier is employed to boost the signal due to the inversion of signals by the inverter circuit in the transmitter of the UN AFE. At the AGC stage, the signals are amplified with variable gains to stabilise their amplitude, ensuring steady performance even in the presence of fluctuations caused by UN movements. After AGC, a comparator converts the signals to digital Low/High states. The resultant 1-bit digitised signals are then routed to the MCU. The receiver AFE specifications are listed in Table 4.2. All components involved in the AFE design are chosen for optimal performance and these are commercially available at affordable prices.

4.3.2 The ADR Design

This section outlines the ADR structure developed for experimental investigation. According to the results of the analytical study detailed in Section 4.4.1.2, square frustum (SF) and hexagonal frustum (HF) do not show differences; Therefore, considering the performance and implementation complexity, a SF-type ADR with five PDs is implemented. Fig. 4.5 illustrates the designed ADR structure with dimensions in millimetres. This is a custom-built design that in-

Table 4.2: *AFE Receiver specifications.*

AFE Block	Gain	Bandwidth
TIA (OPA380)	15 kΩ	3.07 MHz
Passive HPF	-	1.06 kHz
Amplifier (OPA830)	21.6 dB	5.09 MHz
Passive LPF	-	2.2 MHz
AGC (AD605)	-14 to +82.8 dB	8 MHz

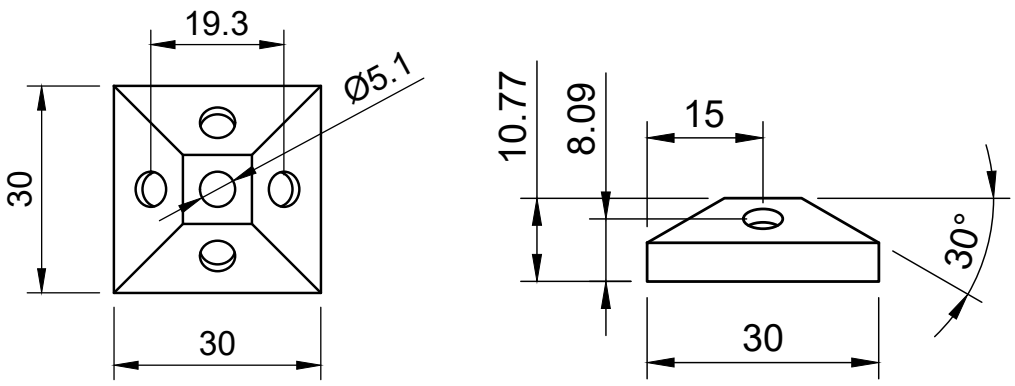

(a) *Top view* **(b)** *Side view*

Figure 4.5: *ADR structure design.*

corporates commercially available PD, specifically BPV10, which offers a field of view (FOV) of $40°$. The dimensions of the ADR are 30 mm in width and length, and 10.77 mm in height. The side PDs are tilted at an angle of $30°$ to ensure overlapping coverage with adjacent PDs.

Fig. 4.6 illustrates the electrical link between the ADR and the TIA. In the arrangement, the PDs are placed in parallel and connected to the TIA. This configuration functions as EGC, which combines the signals from all PDs. The analytical results in 4.4.1.2 show that EGC provides reasonable performance compared to other combining techniques. Therefore, EGC is adopted due to its simplicity of implementation. The theoretical -3 dB bandwidth of TIA is derived as follows [143]:

$$f_{-3\mathrm{dB}} = \sqrt{\frac{\mathrm{GBP}}{2\pi(C_{\mathrm{T}})R_1}} \qquad [\mathrm{Hz}] \tag{4.5}$$

where GBP represents the gain bandwidth product of the operational amplifier (op-amp) used and C_{T} denotes the total capacitance at the inverting terminal of op-amp including the capac-

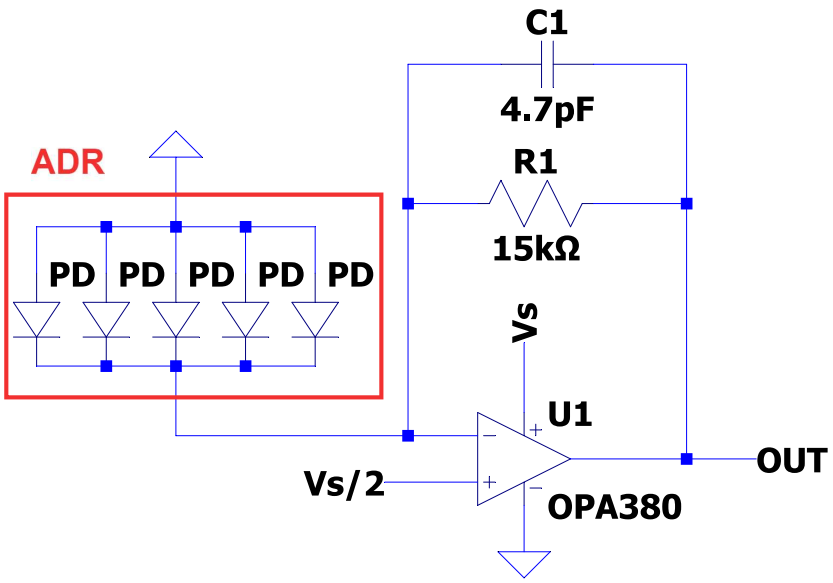

Figure 4.6: *ADR and TIA part in the AFE.*

itance of PD, C_{PD}, as well as the feedback capacitance, C_1. Feedback capacitance serves the purpose of enhancing stability by compensating for phase shifts at higher frequencies to improve stability by creating a pole in the noise gain function, is described as [144]:

$$C_1 = \sqrt{\frac{C_{\mathrm{T}}}{2\pi R_1(\mathrm{GBP})}} \qquad [\mathrm{F}] \tag{4.6}$$

Using (4.5) and (4.6), R_1 and C_1 are derived to be $f_{-3\mathrm{dB}}$ of 3 MHz, which is appropriate for the UART protocol.

4.3.3 Prototype design

Using the previously described AFE and ADR, the AP and UN are prototyped on printed circuit boards (PCBs). The UN has two PCB layers, one each for the AFE and ADR/IR LED mount as shown in Fig. 4.7. The AFE PCB is directly connected to the MCU, providing a 5 V power supply for the receiver and 9 V for the transmitter. The power supply to the MCU comes from a 9 V DC adapter. Figs. 4.8a and 4.8b show the prototypes of the AP processor and the AP AFE. The processor unit is equipped with sensor modules and a microSD card. The AP AFE is connected to the AP processor via SMA connections. The AP AFE unit has a white LED with a reflector and IR PD, facing directly downward. The AP AFE transmits signals from the AP

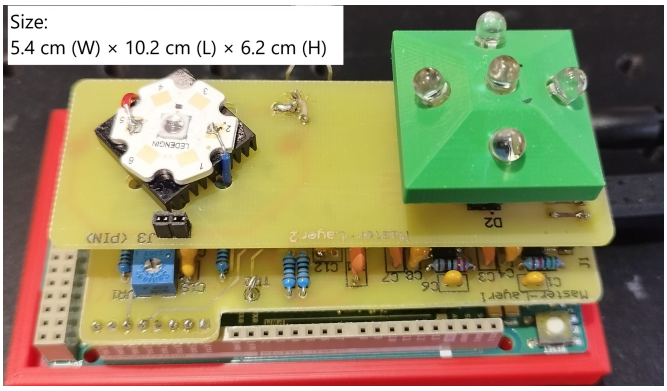

Figure 4.7: *ADR user node prototype.*

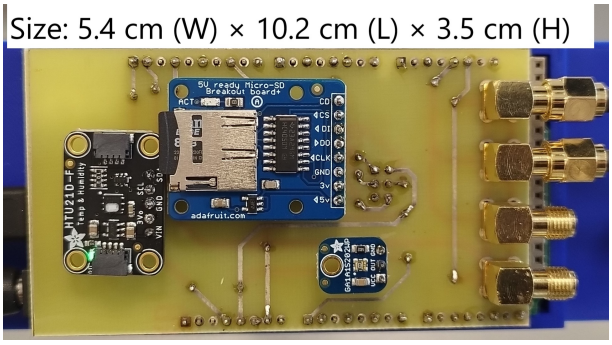

(a) *processor unit*

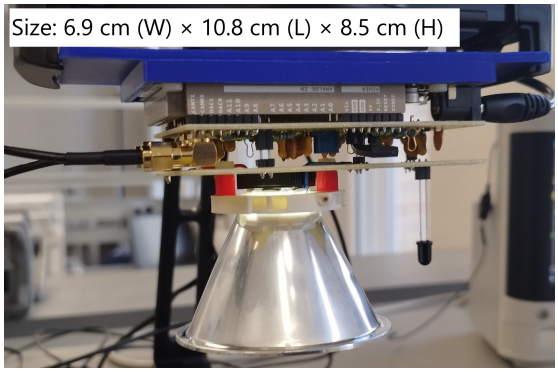

(b) *AFE unit*

Figure 4.8: *AP Prototype.*

processor and receives signals from the ADR UN.

Power consumption is measured to show the amount of electrical power the prototype needs. In Table 4.3, the power usage of the ADR, AP processor, and AP AFE is recorded as 1.46, 0.53, and 3.85 W, respectively, in idle state. When assessing power consumption in the active state

during which the prototype transmits data, the consumption remains comparable, due to the brief transmission duration facilitated by the small packet configuration of the UART protocol.

Table 4.3: *Power consumption of the prototype in Watt.*

State	ADR	AP (Processor)	AP (AFE)
Idle	1.46	0.53	3.85
Active	1.49	0.54	3.84

4.4 NUMERICAL/EXPERIMENTAL Results

The VLC-based multiple-input multiple-output (MIMO) (VLC-MIMO) system performance is evaluated using the system model previously described in Section 4.2 and the parameters used for the analytical studies are shown in Table 4.4. By applying the optimisation technique for the PD tilt angle as detailed in (3.21), the optimal tilt angle is determined to be 35° when the ADR coordinates are in the centre of the room, specifically at (2, 2, 1). Another crucial performance factor is the rotation angle of the ADR, δ_{R}, since this angle affects the channel gain according to (2.4) and (2.5). To assess average performance at different values of δ_{R}, the Monte Carlo (MC) method is employed. Each calculation generates δ_{R} as a uniformly distributed pseudorandom integer ranging from 0° to 360°, following the procedure outlined in [22]. Additionally, the coordinates of a single reflected point are randomly assigned near the centre of each wall using a truncated normal distribution.

Following the results of the theoretical validation, experimental evaluations are performed using a prototype developed by choosing the optimal combination of ADR type and receive diversity technology. In these experimental verifications, the performance of the proposed VLC-IoT system is evaluated. ADR performance is assessed at various positions within the X-Y plane, examining SNR and bit error rate (BER) across the coverage region. To demonstrate enhancement in ADR performance, the coverage performance with a single PD receiver is also assessed. Furthermore, real-time sensor data transmission is shown to establish its viability for IoT applications. During the experiment, data collected from the sensor module is transmitted through the VLC DL. The sensor data received are compared with the data stored on the microSD card. A demonstration of the prototype is available in the accompanying video cited in [145].

Table 4.4: *SIMULATION PARAMETERS.*

Room parameters	Values [References]
Room dimensions (L_x, L_y, L_z)	(4 m, 4 m, 3 m) [18]
Number of LEDs N_{t}	4 [18, 19, 21–24]
LEDs coordinates (X_i, Y_i)	(1, 1), (1, 3), (3, 1), (3, 3) [23]
Reflective area A_{r}	1 cm^2 [19, 21]
Reflective coefficient ρ_{k}	0.8 [19, 21]
LED transmitter parameters	Values [References]
LEDs height	3 m [18, 19, 22, 24]
LEDs elevation angle	180° [21]
LEDs semi half angle $\Phi_{1/2}$	15°, 45° [18, 21, 76]
Average transmitted power P_{t}	1 W [19]
Receiver parameters	Values [References]
ADR coordinates	(X_{r}, Y_{r}, Z_{r}) [19]
Area of PD A	1 cm^2 [18, 24]
Number of PDs N_{r}	$4, 5, 6, 7$
PDs responsivity $\mathcal{R}$	1 A/W [71]
PDs FOV Ψ	45°, 60° [18, 19, 24]
ADR elevation angle	0° [18, 19, 21–24]
PD tilt angle δ_{tilt}	35°

4.4.1 Monte-Carlo based Performance Evaluation

The SNR distributions of a conventional single PD receiver and various ADR types are examined to illustrate the differences in analytical performance between these receivers. The case study room is segmented into a grid consisting of points evenly spaced at 10 cm intervals across the X-Y plane. At each designated point, the SNR is determined utilising a MC simulation, which is executed $N = 5000$ times. The distribution is scrutinised using a box chart to highlight statistical attributes. Each box chart is constructed using the SNR values from all grid points. Additionally, the SNR mean and variance values of SNR are presented.

4.4.1.1 Performance of A Single PD Receiver

The SNR distribution of a single PD receiver, orientated vertically at an elevation angle of $0°$, is shown using a variable semi-half angle LED along with the FOV of the PD. The SNR for a single PD receiver can be determined by simplifying (4.2) to:

$$\mathrm{SNR} = \frac{\sum_{j=1}^{N_t} (\Re h_{1j} P_o)^2}{\sigma_n^2} \tag{4.7}$$

Fig. 4.9 shows the distribution and box chart of the SNR for the single PD receiver under three configurations: (a) $\Phi_{1/2} = 45°$ and $\Psi = 60°$, (b) $\Phi_{1/2} = 45°$ and $\Psi = 45°$, (c) $\Phi_{1/2} = 15°$ and $\Psi = 60°$ at variable coordinates of (X_r, Y_r, 1). In distribution (b), a narrower FOV gives a smaller area under the LED cells with an SNR of more than 30 dB compared to distribution (a). When the half-angle difference of the LEDs is compared between the distributions (a) and (c), the narrower angle results in an enhanced SNR beneath the LED transmitter and the SNR

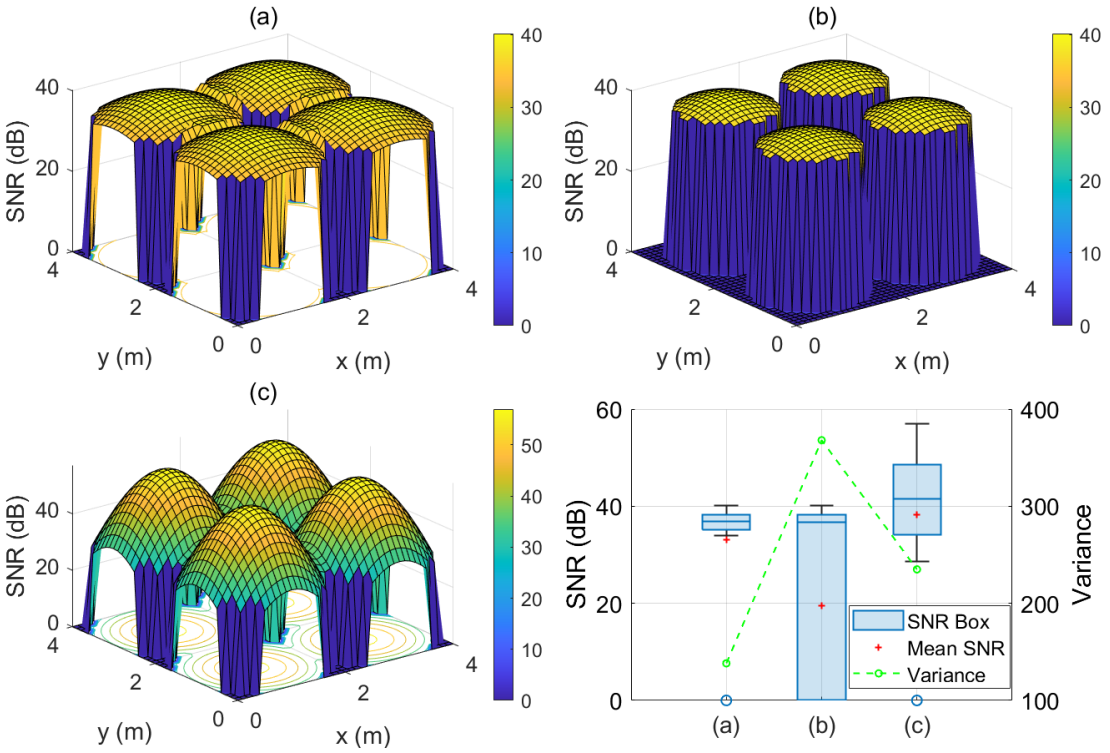

Figure 4.9: *SNR distribution and SNR box chart, mean and variance of the single PD receiver at the coordinates of (X_r, Y_r, 1): (a) $\Phi_{1/2} = 45°$ and $\Psi = 60°$, (b) $\Phi_{1/2} = 45°$ and $\Psi = 45°$, (c) $\Phi_{1/2} = 15°$ and $\Psi = 60°$.*

decreases rapidly away from the normal direction of the LED. The SNR box chart in Fig. 4.9 reveals that amongst these, distribution (a) exhibits the least variance, whilst distribution (b) has the lowest mean SNR. Distribution (c), despite having the elevated SNR, shows greater variance relative to distribution (a), attributed to the elevated Lambertian emission order.

Concerning the influence of height, the performance is characterised in the position (X_r, Y_r, 0). Fig. 4.10 illustrates the distribution along with the box plot for $\Phi_{1/2} = 45°$ and $\Psi = 45°$. This distribution resembles the distribution (a) $\Phi_{1/2} = 45°$ and $\Psi = 60°$ in Fig. 4.9 although the mean SNR is lower due to the longer distance. At higher heights, a narrower FOV leads to a wider SNR distribution. The mean SNR is approximately 30 dB, with a variance of 43, which is smaller than that of the distribution (a) depicted in Fig. 4.9.

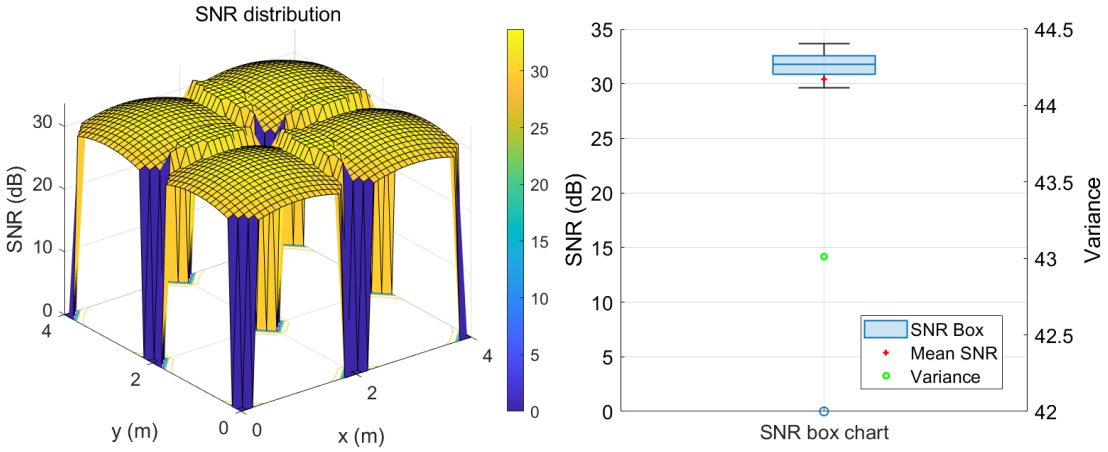

Figure 4.10: *SNR distribution and SNR box chart, mean and variance of the single PD receiver at the coordinates of (X_r, Y_r, 0) at $\Phi_{1/2} = 45°$ and $\Psi = 45°$.*

4.4.1.2 Comparison of ADR Configurations

The evaluation of each ADR type is conducted at variable coordinates (X_r, Y_r, 1), specifically at $\Phi_{1/2} = 45°$ and $\Psi = 60°$. Fig. 4.11 illustrates the SNR values through a box chart, including the mean and variance for each ADR in conjunction with various combining techniques. In all of these three combining techniques, the mean SNR values exceed 30 dB, regardless of the ADR configuration. In addition, the variance in SNR ranges from 2.6 to 6.5. Models such as square pyramid (SP) and hexagonal pyramid (HP) (alternatively SF and HF), specified in Section 3.3, have almost the same performance in terms of box-chart representation, mean, and variance values, indicating that there is no significant advantage in using a frustum-type

ADR. Notably, SF and HF achieve the highest mean SNR for the SC methodology at 36.5 dB. However, when paired with MRC, these ADRs demonstrate reduced variance compared to their use with SC. Using MRC, the frustum-type ADR exhibits a box plot that evenly spans from the median to the upper and lower quartiles, with whiskers uniformly extending, and there are no outliers.

The SNR distribution of the SP and SF ADR categories is depicted in Fig. 4.12. The SNR for the SP under any LED cell is less than that of the SF, owing to the absence of a PD on top of

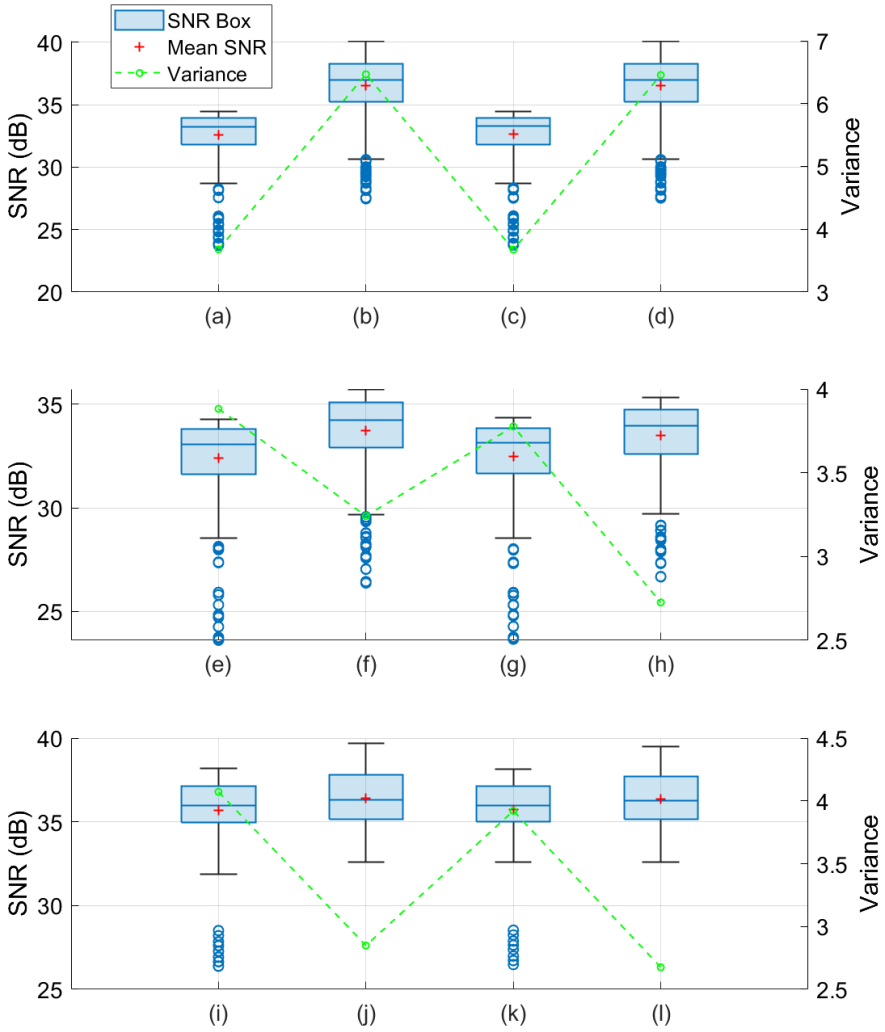

Figure 4.11: *SNR box chart, mean and variance in the single-cell scenario: (a) SP with SC, (b) SF with SC, (c) HP with SC, (d) HF with SC, (e) SP with EGC, (f) SF with EGC, (g) HP with EGC, (h) HF with EGC, (i) SP with MRC, (j) SF with MRC, (k) HP with MRC, (l) HF with MRC.*

ADR. Amongst the three combining techniques, the SF employing either SC or MRC exhibits about 40 dB. Notably, the minimum SNR for the SF with MRC is 5 dB superior compared to SC. Evaluating these SNR distributions reveals that frustum-type ADR ensures a consistent SNR distribution with any combining approach, as it allows integration of all signals from LED transmitters acting as a single-cell. Thus, the selection of combining techniques in the system should be guided by both ease of implementation and performance.

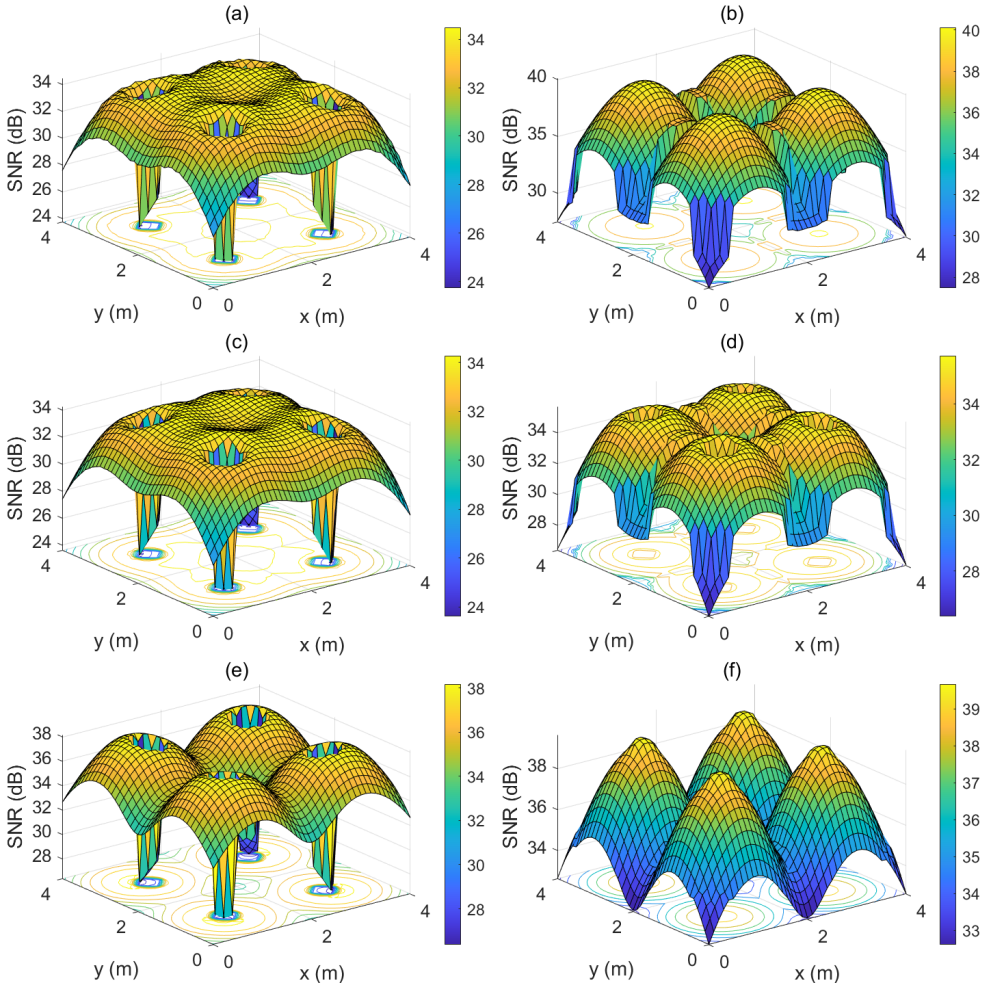

Figure 4.12: *SNR distribution in the single-cell scenario: (a) SP with SC, (b) SF with SC, (c) SP with EGC, (d) SF with EGC, (e) SP with MRC, (f) SF with MRC.*

4.4.2 Experimental Performance Evaluation

The implemented prototype VLC-IoT system with the designed ADR is examined. The EGC technique is chosen for its simplicity of implementation and sufficient performance enhance-

ment, which is shown in the results of the analytical study in the previous section 4.4.1.2. Fundamental performance, including BER against distance, SNR, and BER coverage, is measured to show an improvement of communication performance compared to the single PD receiver.

4.4.3 BER vs Distance Measurements

The BER performance as a function of distance is assessed to demonstrate reliability of communication. The AP sends a randomly generated binary sequence comprising 10^5 bits, organised in an array. These random bits are incorporated into the data frame of a UART packet, which is then received by the ADR and stored in an array of identical size to the original bit streams. This allows BER calculations by comparing the received bits with the originally generated bits. The LED operates with a driving current of 320 mA and a forward voltage of 3.12 V. BER assessment is measured by contrasting the received data with the transmitted bit sequence. In Fig. 4.13, the relationship between BER, illuminance, and distance is illustrated. In particular, at data rates of 1 Mbps and 2 Mbps, error-free transmission is maintained up to 4.2 m and 3.2 m, respectively. The BER reaches the forward error correction (FEC) threshold of 3×10^{-3} at 4.3 m for 1 Mbps and 3.6 m for 2 Mbps. The measured illuminance is approximately 500 lux at 1 m, decreasing gradually to below 50 lux at a distance of 4.5 m. When the transmitter is

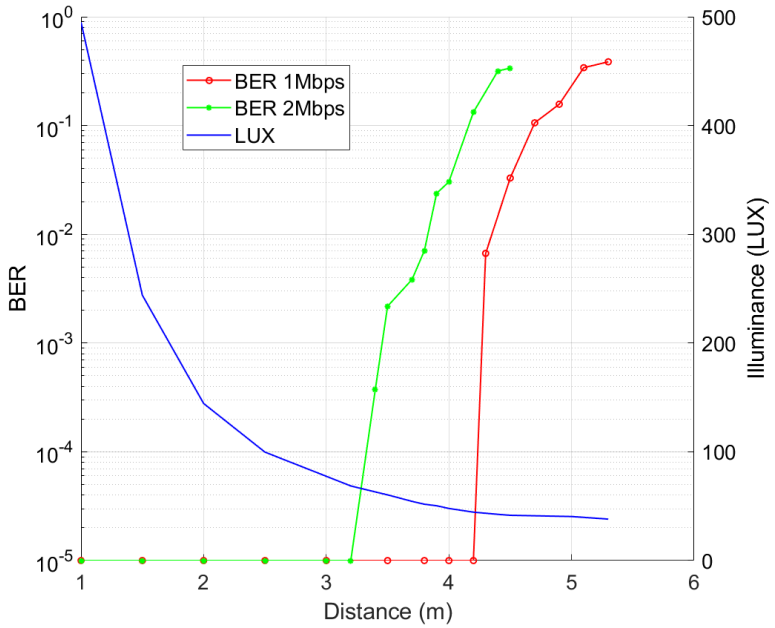

Figure 4.13: *The DL BER performance at different distances and illuminance levels.*

inactive, the ambient light level at the ADR receiver registers at 18.4 lux.

4.4.3.1 Received SNR Distribution

The SNR distribution is evaluated using the experimental setup depicted in Fig. 4.14. The setup includes a height, h, of 1.6 m, a semi-half angle of the reflector, $\Phi_{1/2}$, of 12.5°, and a separation between the APs, d_{AP}, of 1 m, as shown in Fig. 4.1. To determine the electrical SNR at the receiver, measurements are taken from the output of the inverting amplifier in the receiver's AFE, prior to the AGC, at each point on a 12.7 cm XY grid. This grid features a total of 121 points arranged in an 11 by 11 square within the X-Y plane. During this assessment, each AP emits a sinusoidal signal with a 3 V peak voltage at a frequency of 1 MHz, alongside an LED drive current of 220 mA. An oscilloscope is used to measure the peak-to-peak voltage, V_{pp}, at the UN amplifier output along with noise voltage levels. The signal power received can be derived from the following:

$$P_{\mathrm{signal}} = \frac{V_{\mathrm{RMS}}^2}{R_{\mathrm{Load}}} = \frac{V_{\mathrm{pp}}^2}{8R_{\mathrm{Load}}} \tag{4.8}$$

where R_{Load} is considered to be 50 Ω. The noise variance, determined from noise voltages measured at five different grid locations with 62500 samples for each is 7.24×10^{-5} and 5.02×10^{-5} for the ADR and the single PD receiver, respectively.

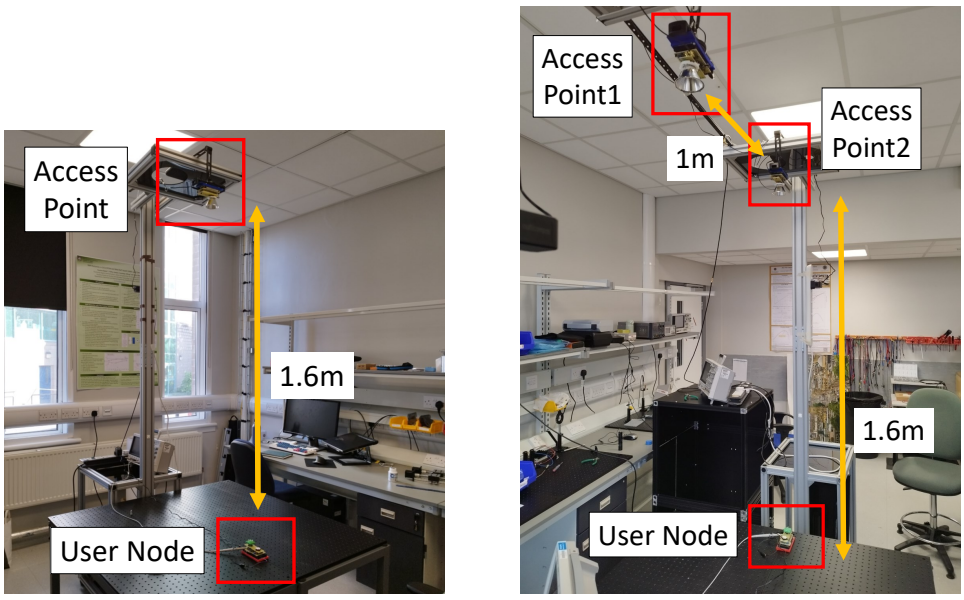

(a) *1 AP* **(b)** *2 APs*

Figure 4.14: *Measurement setup.*

The SNR distribution in two scenarios, involving an AP and 2 APs, is shown in Fig. 4.15 for both the ADR and the single PD receiver, respectively estimated from (4.8) with the measured noise variance. It is evident that the SNR of the ADR UN attains 17 dB directly underneath both the single AP and 2 APs scenarios. Looking at Fig. 4.15a, the ADR SNR diminishes progressively to 8 dB towards the boundary of the AP cell. The SNR of a single PD in Fig. 4.15b is noted to be around 7 dB less than that of ADR decreasing to 1 dB at the edge of the cell. The SNR fluctuation of ADR is 9.82 dB, which is less than the 10.94 dB variation observed for the single PD. In the 2 APs scenario, as shown in Fig. 4.15c, the ADR SNR reduces gradually to under 12 dB nearing the limit of the AP reach. For a single PD in Fig. 4.15d, the SNR of is 4 dB lower than that of ADR within these APs contexts, then decreasing to just under 10 dB at the edge of each AP coverage. Typically, the use of ADR facilitates a higher SNR attributable to the presence of multiple PDs. The ambient light level across the grid, measured by a light metre,

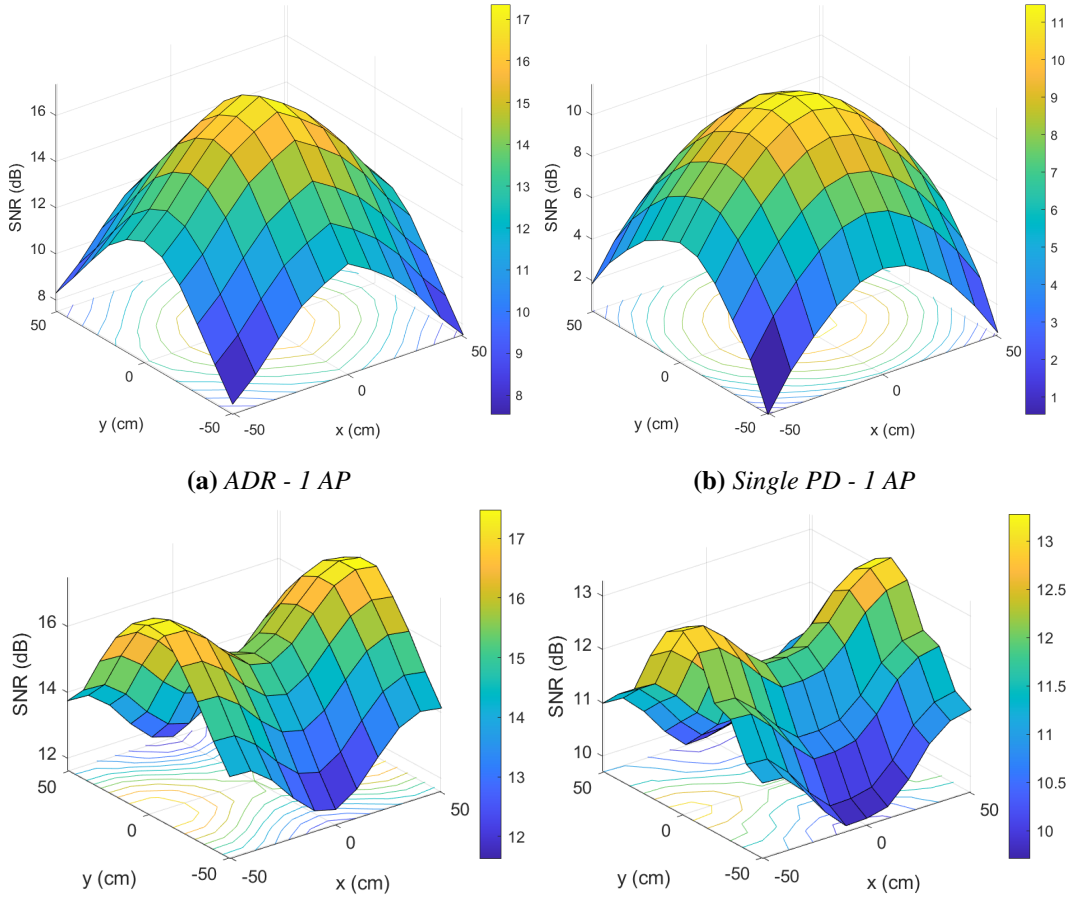

(a) *ADR - 1 AP*

(b) *Single PD - 1 AP*

(c) *ADR - 2 APs*

(d) *Single PD - 2 APs*

Figure 4.15: *Received SNR distribution over the coverage area.*

ranges from 261 to 712 lux, with an average value of 478 lux, which is standard for indoor illumination. This measurement highlights the dual functionality of the AP as an illumination source and a data hub.

4.4.3.2 BER Distribution and Coverage Rate

BER distributions are evaluated to demonstrate the coverage areas. The coverage rate is determined by comparing the BER with the FEC threshold. BER values are acquired using the same methodology as the BER vs distance assessments, recorded at each location on the same X-Y grid as the SNR distribution using the experimental setup as in Fig. 4.14. The BER distribution at 2 Mbps is illustrated in Fig. 4.16, employing the ADR and a single PD receiver. It is evident that the ADR has a larger error-free coverage area compared to the single PD. The BERs for both the ADR and the single PD experience degradation toward the edge of the cell due to de-

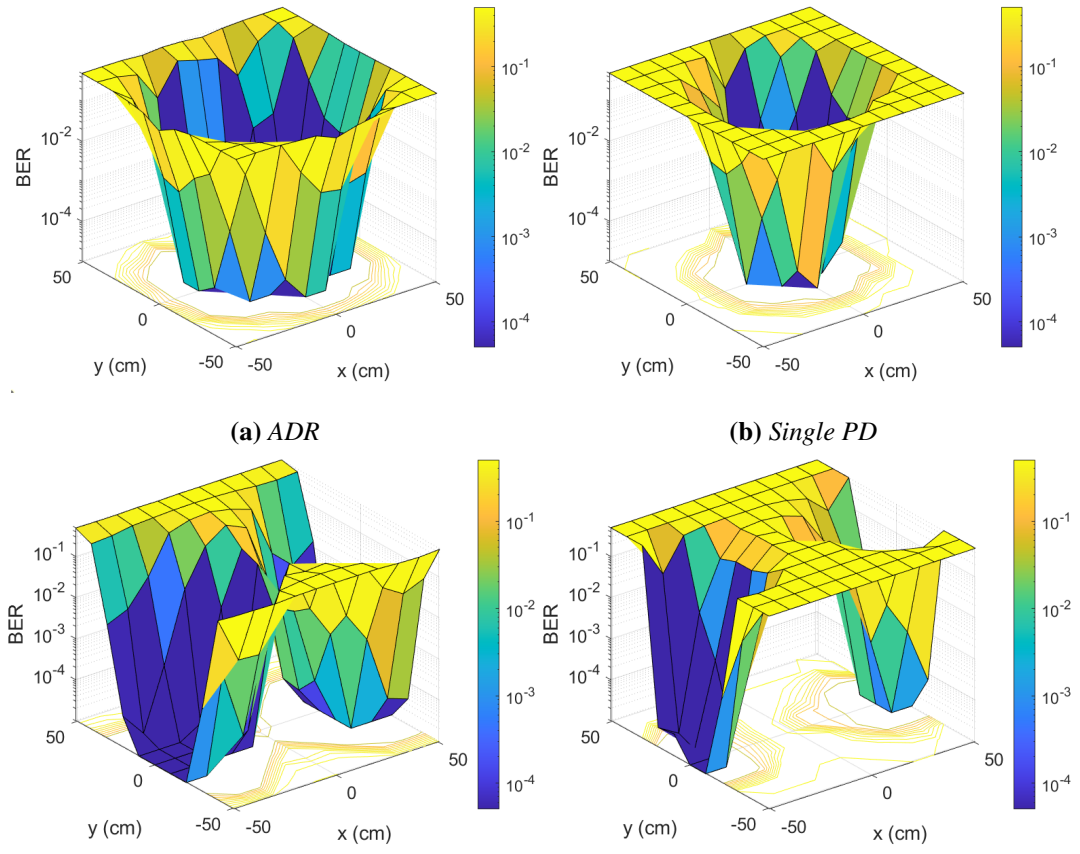

(a) *ADR* **(b)** *Single PD*

(c) *ADR* **(d)** *Single PD*

Figure 4.16: *BER distribution over the coverage area.*

creased received power. A point is considered to be under the coverage of the VLC link when its BER is below the FEC limit of 3×10^{-3}. Subsequently, the coverage rate is calculated using the equation previously defined in 3.4.2.3 as

$$R_{\text{coverage}} = \frac{N_{\text{p}}}{N_{\text{total}}} \times 100 \quad [\%] \tag{3.22}$$

Table 4.5 presents the number of covered points and the coverage rates for the ADR and the single PD in the 1 AP/2 APs scenarios. In the single-AP, the ADR successfully covers 44 points out of 121, compared to 21 points covered by a single PD. This corresponds to an ADR coverage rate of 36.36%, which more than doubles the rate of a single PD, recorded at 17.36%. Similarly, in the 2 APs scenario, the ADR covers 45 of 121 points, whereas the single PD again covers 21 points. Here, the ADR achieves a coverage rate of 37.19%, effectively doubling the single PD's rate of 17.36%. These findings indicate that the proposed ADR configuration significantly extends coverage, enabling robust communication. It should be noted that the improvement in performance is attributed to the increased number of PDs relative to a single PD, whilst maintaining the same scale and cost for the AFE. Hence, the proposed ADR offers an expansive communication coverage, effectively reducing the negative effects of misalignment.

Table 4.5: *Coverage rate (%) of ADR and the single PD.*

Scenario	Receiver	Covered points	Coverage rate (%)
1	ADR	44	36.36
AP	Single PD	21	17.36
2	ADR	45	37.19
APs	Single PD	21	17.36

4.4.4 Real-Time Sensor Data Transmission

To demonstrate the feasibility of the ADR system under practical conditions, a full-duplex sensor data transmission is conducted in real-time. Within this system, the ADR UN sends a request to an AP for sensor data, and the AP responds by transmitting the requested data back to the ADR UN. Fig. 4.17 and Algorithm 1 illustrate the flow chart of the AP and UN, as well as the algorithm for data storage in the AP. As depicted in Fig. 4.17a, the AP initiates a data storage function, which interrupts the system to acquire sensor data from the module,

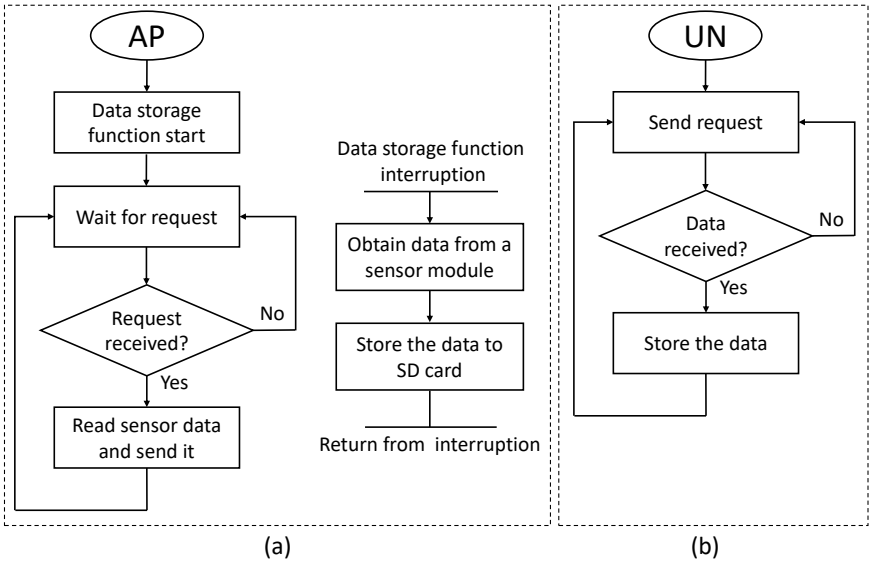

Figure 4.17: *The process flowchart. (a) Access Point and (b) User Node.*

Algorithm 1 Data storage function in AP.

1: Define an array size N_s, the number of data logs N_l
2: Initialise counter C and set interruption timer
3: **if** Interruption happens **then**
4: Obtain data and save it on the current data log
5: Update $C \leftarrow C + 1$
6: **if** C is N_s **then**
7: Delete data in the oldest data log
8: Update the current data log $\leftarrow$ the oldest data log
9: Reset C
10: **end if**
11: **end if**

subsequently saving it to a microSD card according to Algorithm 1. The algorithm ensures that data logs are maintained to prevent interference with both transmission and storage processes. Following the initiation of this function, the AP stands by for a request from the UN. Upon receiving such a request, the AP transmits the most recent data log in response.

In this study, data from three sensors that measure light, temperature, and humidity are communicated. The packet error rate (PER) and response time metrics are provided to evaluate the transmission of sensor data in real time. Given that the MCU supports 256 bytes within

its UART buffer, a maximum of 200 bytes can be used for payload in the packet structure, as illustrated in Fig. 4.18. The lux data are sent as a raw value sourced from the MCU's analogue-to-digital converter (ADC), which consumes 3 bytes as an integer type. Consequently, the payload can accommodate up to 50 lux readings, including a 1-byte delimiter. In contrast, temperature and humidity readings are 5 bytes each in float type, allowing up to 33 entries per packet. In general, it is observed that an increase in the data length of the packet is correlated with a higher probability of packet errors.

Header 4 bytes	Payload Maximum 200 bytes	Trailer 3 bytes

Figure 4.18: *Packet design for DL data.*

Fig. 4.19 illustrates the transmission of sensor data at a rate of 1 Mbps, comparing the saved sensor data and the received data. When a request is issued by the UN, the AP transmits the stored data. These received data are stored in an array to facilitate comparison with the originally saved data. Two received data scenarios are depicted: one in which the data flow is briefly interrupted and the other in which it is uninterrupted. The saved sensor log consists of

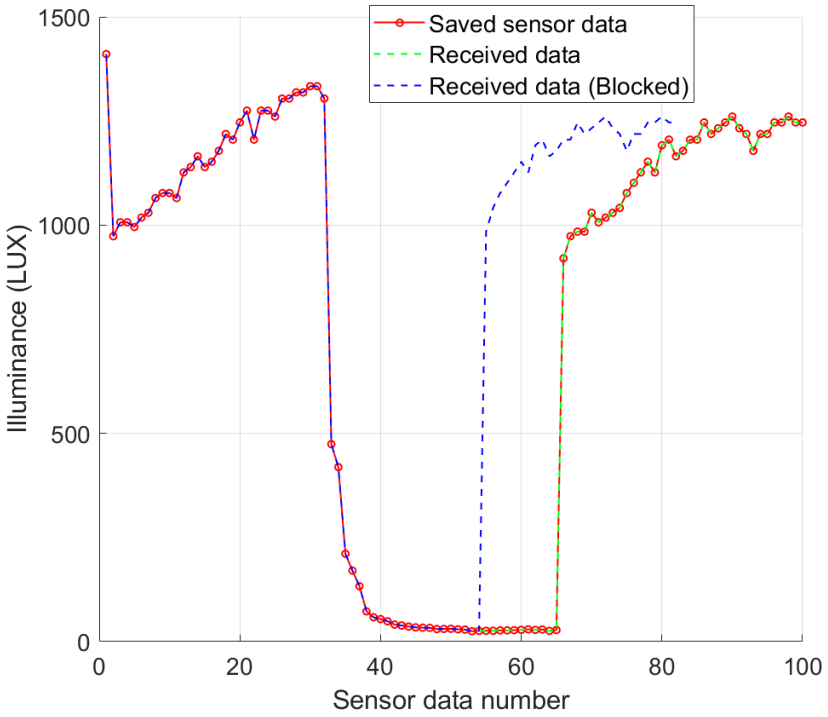

Figure 4.19: *Light sensor data transmission.*

100 samples that capture illuminance values in an indoor environment. Error-free transmission is observed under unblocked conditions, whilst link obstruction leads to data loss, with some portions missing from the received data, resulting in a trace of less than 100 samples. Measurements carried out in ten trials show that UN experiences an average wait time of 8.70 ms for a response from AP, which replies to the request after an average of 6.27 ms.

Fig. 4.20 illustrates the association between PER, the response time, and the quantity of data per packet showing the PER and the response times for three sets of sensor data collected in an indoor room. The PER and the response time are measured with different numbers of data per packet, with 1000 packets transmitted at a rate of 1 Mbps. The received data are stored in an array to facilitate comparison with the data saved in AP. The stored data quantities for light, temperature and humidity comprise 50000 samples with average values of 622, 26.07°C, and 42.52%, respectively. Packets containing data payload errors are counted as packet errors. The occurrence of packet errors increases with the data quantity per packet, recorded as 50 errors for the lux value and 30 for temperature and humidity values, due to the heightened error probability alongside increasing payload length. In this condition, the system can support packet error free up to 40 data per packet for lux data and 20 data per packet for temperature and

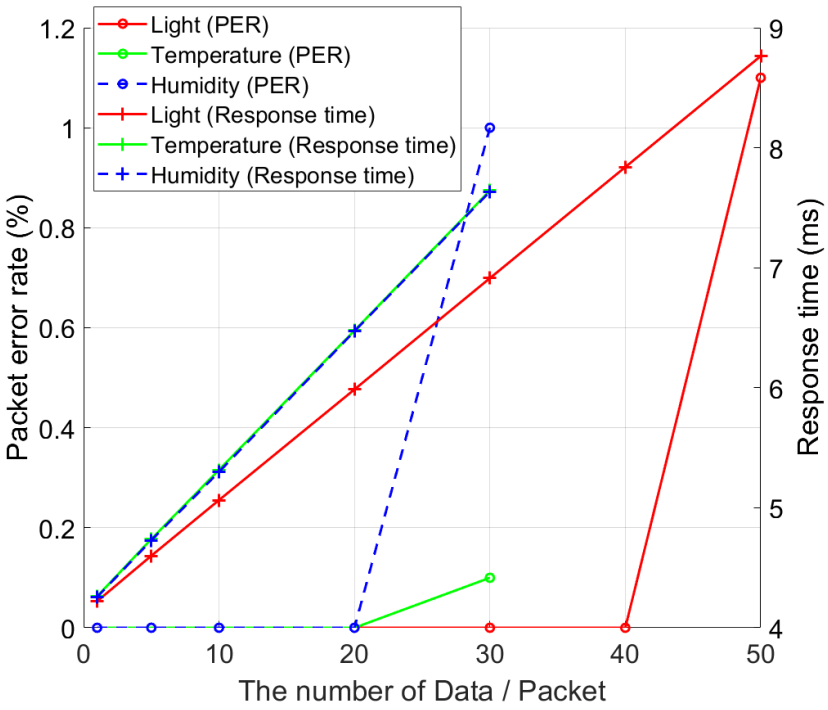

Figure 4.20: *PER and response time of three different sensor data.*

humidity data. The packet error is considered a consistent error because it occurs only when the packet size exceeds the specified length. The response time, which represents the duration for AP to reply to UN's request, linearly increases from approximately 4 ms with increased data quantities, as AP requires extended durations to retrieve sensor data from the SD card. The response time increment for temperature and humidity exceeds that for light intensity due to the larger data size.

4.5 Summary

In this chapter, the performance of the ADR system was analysed through a numerical study, and then a real-time VLC system using ADR was demonstrated for single-cell IoT sensor networks. The prototype consisting of the designed AFE and the custom-built ADR demonstrated enhanced communication performance compared to a single PD receiver.

The analytical study compared the SNR distributions of single PD receivers and various types of ADRs in an indoor environment. A grid-based simulation assessed the SNR at different points and was analysed with box charts to depict statistical characteristics such as mean and variance. It can be concluded that a PD receiver with a limited FOV enhances SNR directly beneath an LED transmitter, yet the SNR rapidly decreases outside the LED's normal line. In contrast, an expanded FOV provided a larger area of elevated SNR but with reduced peak levels. ADRs, including SP, HP, SF, and HF, exhibited comparable performance in terms of SNR distribution and variance. Frustum-type ADR did not provide significant benefits over others. The SF-type ADR with SC and MRC combining techniques achieves higher mean SNR values, around 40 dB, but MRC showed a lower SNR variance compared to SC. In general, the choice of ADR and combining technique should consider the balance between ease of implementation and performance stability, as frustum-type ADRs ensure a more stable SNR distribution despite different combining techniques.

In the experimental study, a prototype of the VLC-IoT system was implemented, featuring a designed ADR to improve communication performance. Based on the analytical results, the SF-type ADR with EGC was chosen for the prototype design. Key measurements revealed that the ADR supports error-free communication at 1 Mbps up to 4.2 m and at 2 Mbps up to 3.2 m. The ADR showed superior SNR, maintaining a higher value in the single and dual AP scenarios. The coverage rate indicated that the ADR coverage area where communication can

be supported is more than doubled. Furthermore, real-time demonstration showed the feasibility of reliable duplex connectivity in VLC-aided IoT sensor networks, and full-duplex sensor transmission was also demonstrated to be feasible with real-time data exchange, although limitations arose with increased packet sizes, leading to higher error rates and response times. The experimental results measured response times averaging 8.70 ms for UN requests and 6.27 ms for AP responses. The advantages of the ADR system in wider coverage and efficient data communication were confirmed, whilst highlighting challenges related to packet size and data error in practical applications.

Chapter 5
Integrated VLC-RF System with ADR for Secure Industrial IoT Applications

5.1 Introduction

Research on visible light communication (VLC) extends beyond its potential as a simple replacement for radio frequency (RF); studies are also being conducted to validate the feasibility of systems that integrate VLC with existing RF technology [146–150]. These works focus on network integration such as resource allocation optimisation, network management and energy efficiency optimisation. Furthermore, the practical implementation of VLC will require connection to a backbone network, such as a wide area network (WAN) [151–155], which means that this integration must also be the focus of research. To truly demonstrate the practical viability of a hybrid VLC and RF (VLC-RF) system, it is essential to design a prototype, build it into a single cohesive system, and perform the verification in real time.

This chapter proposes a novel integrated VLC-RF system using an angular diversity receiver (ADR) for industrial Internet of Things (IoT) sensor networks. The prototype, including the transceiver's analogue front end (AFE), is designed for microcontroller unit (MCU) operation and is implemented for experimental demonstrations. The scope of the proposed system includes all stages of IoT architecture from nodes to the WAN through access points (APs) as a network gateways. This chapter is an expansion of the previous chapter 4, which proposed the VLC prototype using the custom-built ADR. The target data rate is the same as in the previous chapter 4 with several Mbps using commercially available components. Furthermore, this previous work is extended by modifying the AFE design and adding RF connectivity for an integrated VLC-RF system. The added RF system can be used for hybrid applications for robustness and can also show the full scale of VLC-based IoT (VLC-IoT) supported by the WAN. To demonstrate overall performance, both fundamental aspects and system efficacy are analysed. In the fundamental experiment, the performance of the prototype is compared with that of a single photodiode (PD) receiver in terms of bit error rate (BER) coverage. With the proposed system, the BER coverage is improved with a coverage rate of 50%. The prototype also

shows a better physical layer security (PLS) performance with double secrecy capacity (SeCap) compared to the single PD receiver. Then, in the system performance demonstration, experiments of real-time sensor transmission, image transmission, and integration of the robot arm system indicate benefits in a practical scenario by showing millisecond-order latency through VLC, such as response time, round-trip time (RTT), and one-way latency.

The remainder of this chapter is organised as follows. The structure of the system of the proposed integrated VLC-RF system is discussed in Section 5.2; numerical and experimental results are presented in Section 5.3; and conclusions are drawn in Section 5.4.

5.2 Integrated VLC-RF system structure

The structure of the integrated VLC-RF system discussed in this chapter is described. The system concept is shown in Fig. 5.1, which is structured upon a triple-tier IoT framework linking user nodes (UNs) with a cloud server employed as a WAN via AP gateways. Throughout the network, both uplink (UL) and downlink (DL) are facilitated by APs and UNs, acting as transceivers. This system's architecture incorporates APs mounted on the ceiling and UNs positioned on floors or tables. Bidirectional communication is achieved by the VLC for the downlink and infrared (IR) for the uplink to reduce interference. These dual APs work as a single-cell, interfacing with the wireless fidelity (Wi-Fi) network cloud through RF communication. Consequently, any UN located in the overlap region can merge signals from the two APs through signal combining. Fig. 5.2 presents the block diagram of the proposed system. To address the UN criteria of being cost-effective, energy-efficient and compact, the MCU is utilised

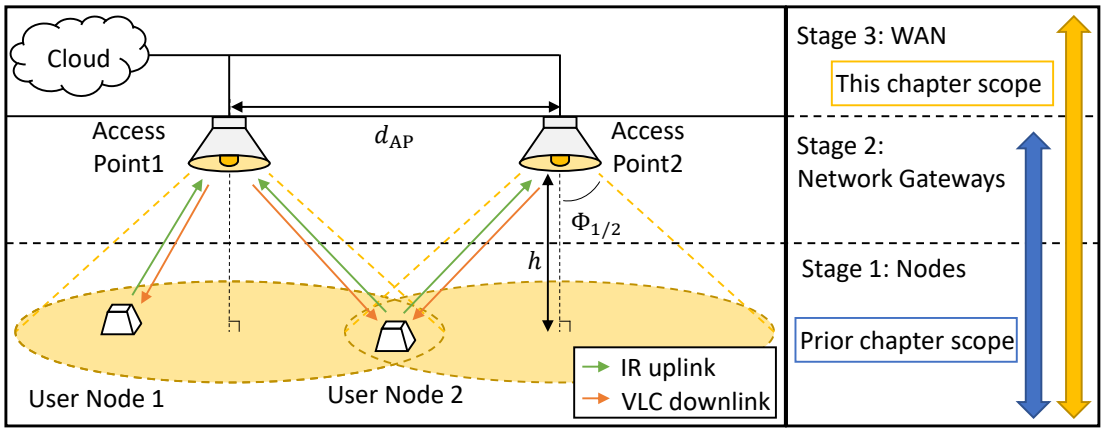

Figure 5.1: *Bidirectional ADR system concept with two APs as a single-cell.*

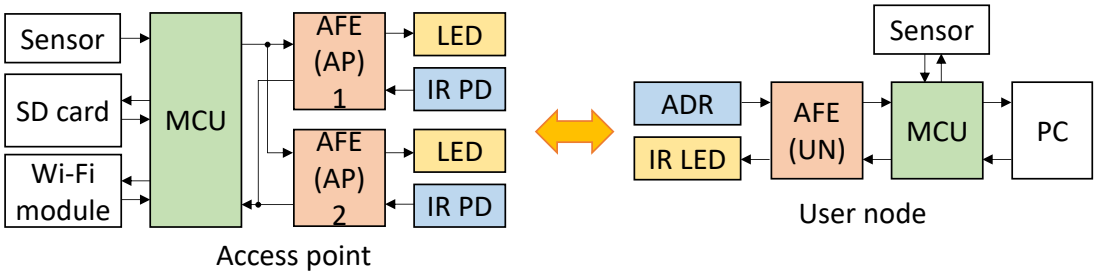

Figure 5.2: *Block diagram of the proposed system.*

due to its cost-effectiveness and small-scale nature. Each AP and UN transceiver comprises an MCU, an AFE, white/IR light emitting diodes (LEDs), and ADR/IR PDs. Sensors are incorporated within the AP MCU to gauge ambient light, temperature, and humidity. These sensor readings are storable on a microSD card and transferable to the cloud. In addition to processing data from the UN, the AP also possesses a Wi-Fi module for RF-based network connectivity. Equipped with a high-luminance white LED with a reflector, along with an IR PD, the AP can also work as a room illumination. The UN MCU, fitted with a sensor, performs tasks such as transmitting command data to the AP and acquiring sensor data. Due to the MCU's limited resources, the communication protocol must be uncomplicated, hence non-return-to-zero on-off keying (OOK) (NRZ-OOK) is implemented using the universal asynchronous receiver/transmitter (UART) protocol.

5.2.1 The Analog Front End

This section describes the design of the AFE receiver for the prototype. The AFE is custom-built to maintain simplicity for the realisation of the VLC-RF system with ADR. Although the transmitter design remains unchanged from the previous chapter 4.3.1, improvements have been made to the receiver design. The ADR follows the same design principles, based on equal gain combining (EGC). Figs. 5.3 and 5.4 represent the block diagram of the AFE and the receiver circuit design for ADR, respectively. Certain components of the design are drawn from 4.3.1,

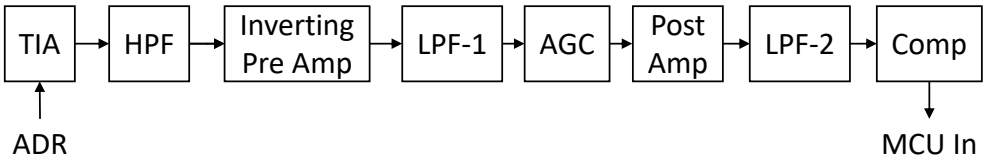

Figure 5.3: *Block diagram of ADR's receiver AFE.*

including a transimpedance amplifier (TIA), an inverting amplifier, an automatic gain control (AGC), and a comparator. The primary modification to the previous design is the inclusion of an additional post-amplifier, located before the comparator. This post amplifier (amp) boosts the signal from AGC, adjusting its output from the scale of hundreds of millivolts to a level that matches the input requirements of the comparator. Consequently, the comparator functions optimally within its designated input range, converting signals into low/high digital outputs. As shown in Fig. 5.4, the receiver incorporates six integrated circuits: a TIA (model OPA380), a pre-amp (model OPA830), an AGC (model AD605) with feedback control managed by an integrating circuit (model OPA810), a post-amp (model OPA354) and a comparator (model AD8611). The current signal detected in the ADR is routed to the inverting input of TIA through J1, where it is converted into a voltage signal. The gain of TIA is set by R_1 valued at 15 kΩ. The -3 dB bandwidth can be determined using the equation outlined in Section 4.3.2:

$$f_{-3\mathrm{dB}} = \sqrt{\frac{\mathrm{GBP}}{2\pi(C_\mathrm{T})R_1}} \qquad [\mathrm{Hz}] \tag{4.5}$$

where GBP is the gain bandwidth product of the operational amplifier (op-amp) and C_T is the total capacitance at the inverting terminal of the op-amp, which includes the PD capacitance, C_PD, and the feedback capacitance, C_1. According to (4.5), the derived values for R_1 and C_T result in a $f_{-3\mathrm{dB}}$ approximating 3 MHz, satisfying the requirements of the UART protocol. The converted voltage signal is then inverted and amplified by a subsequent pre-amp, providing a gain of 21.6 dB as determined by the ratio $-\frac{R5}{R4}$. These amplified signals are appropriately fed into the AGC at the appropriate input level; the AGC uses feedback consisting of an integrating circuit to adjust the gain and keep the amplitude of the output signal constant. The variable gain of the AGC is in the range from -14 to 82.8 dB. The output of the AGC is further amplified by the post-amplifier, which elevates the signal to a level suitable for the comparator, offering a gain adjustable from 0 to 16.3 dB via the potentiometer, VR2. The comparator converts the analog signal from the post-amp into a digital format. The switching voltage of the comparator is managed by the VR3 potentiometer, which adjusts the reference voltage to the offset voltage of the input signal (half of the supply voltage). The width of the hysteresis window is calculated by $\frac{R19}{R19+R20}$ and is designed to be 32 mV. In the final stage, the MCU extracts the 1 bit digitalised signals from the receiver. Table 5.1 lists the specifications for the receiver AFE. The design incorporates readily available and cost-effective components.

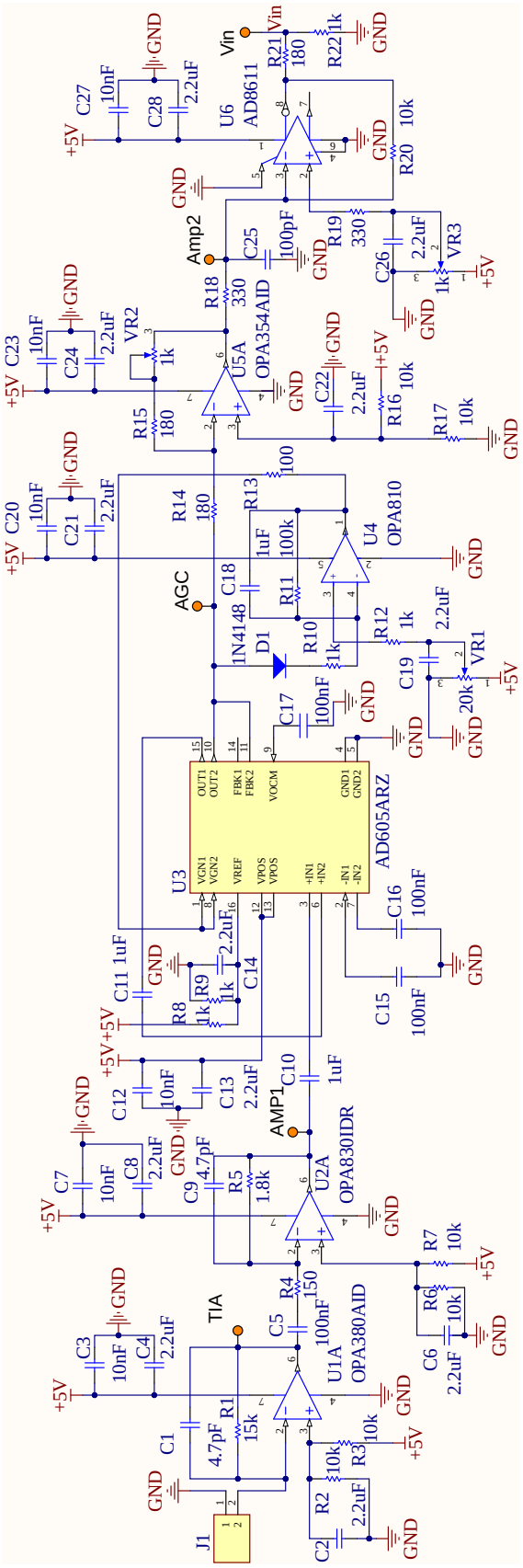

Figure 5.4: *Circuit design of the receiver in ADR user node.*

Table 5.1: *AFE Receiver specifications*

AFE Block	Gain	Bandwidth
TIA (OPA380)	15 kΩ	3.07 MHz
Passive HPF	-	1.06 kHz
Pre Amp (OPA830)	21.6 dB	5.09 MHz
Passive LPF	-	2.2 MHz
AGC (AD605)	-14 to +82.8 dB	8 MHz
Post Amp (OPA354)	1 to 6.6 dB	15.23 MHz to 100 MHz

5.2.2 Prototype Design

In accordance with the AFE design described in Section 5.2.1, printed circuit boards (PCBs) have been designed and fabricated for the AP and UN prototypes. Fig. 5.5 presents the UN prototype featuring two PCB layers, one for the AFE and another for mounting the ADR/IR LED. The ADR model retains the design specified in Section 4.3.2. The AFE PCB seamlessly connects to the MCU sockets, delivering 5 V to the receiver and 9 V to the transmitter. The MCU receives power from a 9 V DC adapter. Figs. 5.6a and 5.6b depict the prototypes of the AP processor and the AP AFE. The AP AFE is linked to the AP processor using SMA connectors and includes a white LED with a reflector and an IR PD aimed downward. The AP AFE manages the signals sent from the AP processor and those received from the ADR UN. The AP processor unit comprises sensor modules and a Wi-Fi module, the ESP32-CAM, which integrates a microSD card and a camera module (OV2640). This choice necessitates a UART interface for Wi-Fi module connectivity with the camera, precluding real-time video transmission via VLC. Data retrieval from the SD card is via the Wi-Fi module. The AP processor is connected to the AP AFE through SMA connectors and incorporates a white LED

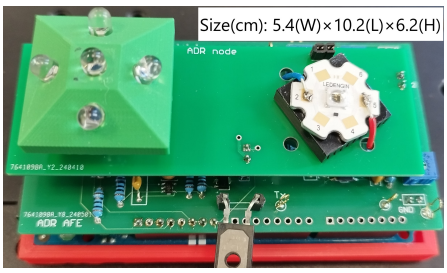

Figure 5.5: *ADR user node prototype.*

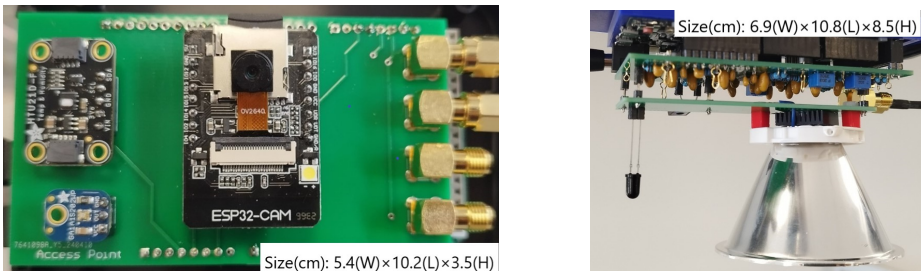

(a) *processor unit* **(b)** *AFE unit*

Figure 5.6: *Prototype of an AP.*

with a reflector and an IR PD. According to Table 5.2, the power consumption of the ADR, AP processor, and AP AFE is 1.47 W, 0.71 W, and 3.83 W, respectively, during idle states. During data transmission, power consumption is measured as the active state, but shows no substantial increase from idle levels due to the brief nature of the compact packet design under the UART protocol. The power consumption of the active-state AP processor rises by about 0.3 W with the inclusion of the Wi-Fi module. The overall power usage of the system depends mainly on the power allocated to the AFE, and for the AP, the power needed for the LED. In this setup, the LED remains on continuously during idle states. Consequently, the power consumed during typical operations does not differ markedly from that used in the particular scenarios examined in this experimental verification. A video demonstration of the prototype, including its mobile suitability as demonstrated by AGC, is available at [156].

Table 5.2: *Power consumption of the prototype in Watt.*

State	ADR	AP (Processor)	AP (AFE)
Idle	1.47	0.71	3.83
Active	1.45	1.04	3.79

5.2.2.1 RF related Design

This section details the RF functionality of the prototype system. For integration into a compact PCB layout compatible with the chosen MCU, the ESP32-CAM development board, illustrated in Fig. 5.6a, is employed. This board offers a cost-effective solution that supports Wi-Fi standards 802.11b/g/n, rendering it ideal for IoT applications. It combines a small form factor with versatile features such as camera and microSD capabilities. The AP processor unit interfaces with the board via a UART connection provided by the Wi-Fi module. The camera and mi-

croSD functions are managed by the AP through the ESP32-based board. In this study, the IoT service, ThingSpeak, is used to facilitate the collection of real-time data within the cloud. This service is employed for the storage, visualisation, and analysis of sensor data. Furthermore, ThingSpeak helps activate responses and distribute alerts to devices using a HTTP connection.

5.2.2.2 Delay Analysis

The performance of the prototype with respect to delay is evaluated in terms of VLC and RF, respectively. The IoT system, comprising an AP and UN, utilises interactive protocols to facilitate communication by sending back an acknowledgement (ACK) after receiving a request. In this framework, delay is defined as the interval from data transmission to reception and processing. This interval includes several types of delay: propagation delay, D_{prop}; transmission delay, D_{tran}; processing delay, D_{proc}; and network delay, D_{net}. Consequently, the delay in one-way packet transmission, denoted as $D_{\text{one-way}}$, is calculated as the aggregate of these individual delay components.

$$D_{\text{one-way}} = D_{\text{prop}} + D_{\text{tran}} + D_{\text{proc}} + D_{\text{net}} \tag{5.1}$$

D_{prop} is almost negligible (in nanoseconds) since both VLC and RF propagate at the speed of light in free space. The transmission delay, D_{tran}, represents the time required to send a single data packet, calculated by $\frac{\text{packet size}}{\text{data rate}}$. For example, sending a 256-byte packet over a 2 Mbps link yields a D_{tran} of nearly 1 ms. The processing delay, D_{proc}, refers to the time the hardware needs to handle the data packet, derived from the clock cycles needed for processing and the CPU clock frequency. This cycle count is determined by the number of instructions and cycles per instruction. Consider an MCU with an 84 MHz clock frequency (such as Arduino DUE) that executes 100 instructions with a 1.5 cycles per instruction; D_{proc} is thus roughly 1.8μs. The network delay, D_{net}, encompasses queuing and media access control (MAC) layer contention delays. The queue delay, or the time packets spend waiting in a buffer before transmission, is not considered in the VLC model discussed here. However, Wi-Fi queuing delay varies with network congestion and traffic, and MAC-layer contention delay, influenced by traffic and channel conditions, also impacts Wi-Fi. Using a MAC protocol known as carrier sense multiple access with collision avoidance, Wi-Fi allows multiple devices to access the wireless channel but, being a best-effort communication method, does not strictly guarantee quality of service (QoS).

RTT can be described as an extension of the one-way delay, representing the time needed to transmit a data packet and receive an ACK back. RTT is mathematically expressed as the sum of one-way transmission and reception delays, formulated as $\text{RTT} = D^{\text{TX}}_{\text{one-way}} + D^{\text{RX}}_{\text{one-way}}$. Notably, RTT encompasses additional delays originating from one-way delay when retransmissions occur, particularly significant in Wi-Fi contexts, where this factor substantially affects RTT. Furthermore, response time, defined as the interval from receiving a request to delivering a response, is crucial in IoT environments, where real-time capabilities are essential, due to its inclusion of application-level processing delays. This study aims to validate real-time performance by evaluating these delay metrics.

5.2.2.3 Security Analysis

This section examines the PLS characteristics of the designed prototype. The PLS in this study is based on the framework of the wiretap channel [55]. A scenario is considered with a transmitter (AP), a legitimate receiver (UN), and an eavesdropper (ED) node. A key performance indicator for evaluating the PLS of this set-up is instantaneous SeCap. Instantaneous SeCap (C_s) represents the highest information rate that can be reliably transmitted to the legitimate receiver without leakage to the ED, taking into account the conditions of the channel at a given moment. SeCap is the information-theoretically defined limit that guarantees perfect secrecy against an ED. This is determined using the Shannon capacities of the main channel (C_B) and that of the ED channel (C_E), as indicated by the equation below [157]:

$$C_s = \max(0, C_B - C_E) \tag{5.2}$$

where Shannon capacity, denoted as $C = B \log_2 (1 + \text{SNR})$, is determined using bandwidth, B and signal-to-noise ratio (SNR), and $\max(0, \cdot)$ guarantees that the result remains non-negative. At the moment when C_s equals zero, secure communication cannot be achieved.

Although the elements influencing secrecy performance vary between Wi-Fi and VLC, they do share common factors such as the SNR and the position of the ED. The secrecy performance of Wi-Fi is significantly affected by fading, which results from the propagation of multiple paths over time. Given that the RF system in this investigation adheres to the Wi-Fi protocol, its secrecy is based on the statistical characteristics of this fading. For VLC, secrecy performance is influenced by optical parameters including the LED's Lambertian order and the PD's field of view (FOV). Unlike RF, VLC possesses a natural security advantage, as light travels in straight

lines and cannot penetrate walls, thus offering strong confidentiality against external EDs [158]. Consequently, a VLC-RF hybrid usage can be designed to harness the complementary strengths of both technologies, resulting in a system with enhanced overall secrecy performance.

5.3 Experimental Results

The study examines the capabilities of the newly proposed integrated VLC-RF system utilising the ADR prototype, focussing on basic and system-level performance to evaluate its practical application potential. Key performance metrics, such as SNR, SeCap and BER coverage, are assessed and compared with a single PD receiver. Furthermore, real-time transmission of sensor data is presented within practical industrial IoT scenarios. The experiment involves transmitting data from the sensor module via the VLC DL, IR UL and the Wi-Fi cloud, with received sensor data cross-checked against those stored on a microSD card or the Wi-Fi cloud server. The transmission of image data and the integration of the system with a robot arm are demonstrated, underscoring the proposed IoT system's feasibility.

5.3.1 Fundamental ADR Performance

This section focusses on the fundamental performance of VLC. The SNR performance is examined in two different experimental settings: one involving a single AP and the other involving two APs. This serves as a basis for analysing the secrecy performance. The BER coverage performance is also evaluated compared to the findings presented in 4.4.3.2.

5.3.1.1 Received SNR Distribution

The SNR distribution is assessed using the same methodology and setup as shown in Fig. 4.14 in Chapter 4. As depicted in Fig. 5.1, the parameters include height h, the semi-half angle of the reflector $\Phi_{1/2}$ and the spacing between APs, d_{AP}, taking values of 1.6 m, 12.5° and 1 m, respectively. The received signal power is calculated from (4.8). The noise variance in the 1 AP and 2 APs scenarios is 3.89×10^{-5} and 3.47×10^{-5}/3.11×10^{-5} and 2.52×10^{-5} for the ADR and single PD receiver, respectively. Ambient light levels measured with a light metre on the grid range from 288 to 988 lux/261 to 712 lux, with average readings of 509.6 lux/477.6 lux for setups with 1 AP/2 APs, respectively, reflecting typical indoor room illuminance. Box

charts of the received SNR values are provided in Fig. 5.7, including mean and variance. For the 1 AP setup, the average SNR for ADR and a single PD measures at 12.96 dB and 8.20 dB, respectively. The ADR whisker spans from 7.86 dB to 17.28 dB, whereas the single PD ranges from 5.16 dB to 11.93 dB. The variance for ADR is 5.19, surpassing that of a single PD at 3.13. In 2 APs scenario, the mean SNR for ADR and the single PD is 15.32 dB and 10.44 dB, respectively. The ADR whisker spans from 11.79 dB to 17.99 dB, whilst the single PD extends from 7.33 dB to 13.08 dB. The variance in the 2 APs setup is reduced compared to the 1 AP scenario, at 2.58 for ADR and 2.28 for a single PD receiver.

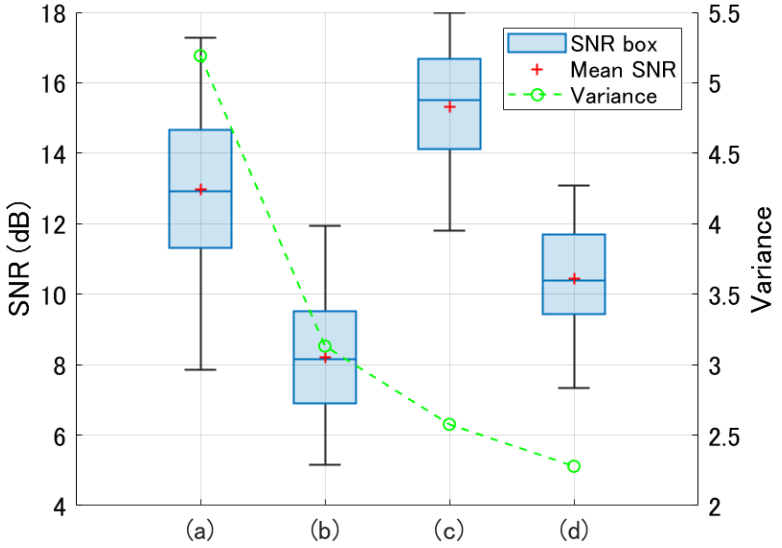

Figure 5.7: *Box chart of the SNR distribution over the coverage area: (a) ADR - 1 AP, (b) Single PD - 1 AP, (c) ADR - 2 APs and (d) Single PD - 2 APs.*

5.3.1.2 Secure Performance

The performance of VLC secrecy is evaluated by calculating the SeCap using the SNR values obtained in the previous section. An ED is assumed to be located at any point on an X-Y grid, following the same setup as in the SNR measurements. The scenario considers the ED employing a VLC receiver comparable to the single PD receiver to intercept the downlink transmission from the AP. The legitimate receiver, which can be either ADR or a single PD receiver, is placed directly below the AP. The SeCap is calculated by substituting the 1 MHz bandwidth and the SNR measured at each location on the grid in (5.2). Fig. 5.8 shows the SeCap distribution for both 1 AP and 2 APs scenarios, based on the ED's location on the indoor X-Y plane. In Fig. 5.8a, the distribution indicates that when an ED is located directly beneath

the AP, the SeCap drops to zero, meaning that secure communication is impossible. The SeCap increases towards the edge of the AP's coverage area, peaking at roughly 1.5 Mbps. Likewise, Fig. 5.8b reveals that no SeCap occurs when the ED is situated directly under either of the two APs. The SeCap is maximised at the edges of the coverage areas, attaining approximately 1.2 Mbps, although this secure rate is somewhat lower compared to the single AP scenario. The results indicate that the SeCap depends on the positions of the legitimate receiver and the ED. The receiver performance of the ED is also a key factor. When the ED uses the same receiver, ADR, as the legitimate receiver, the SeCap becomes limited and secrecy can only be achieved within a restricted area.

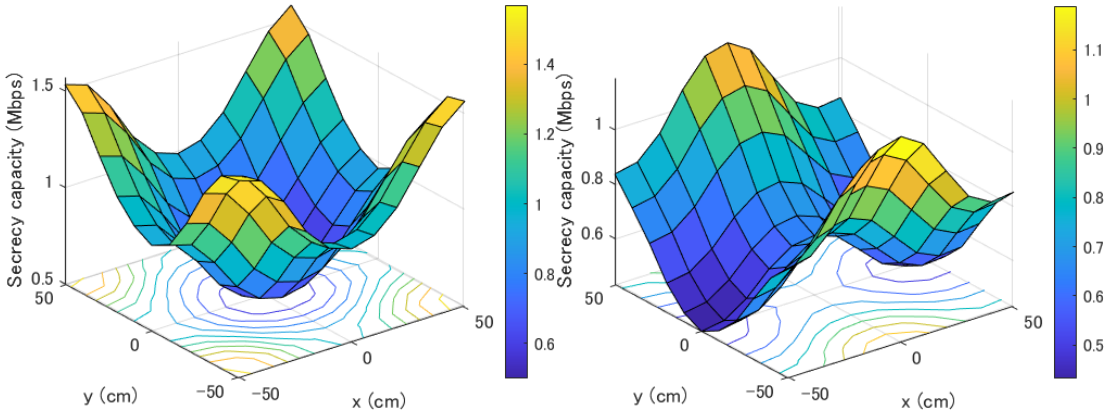

(a) *1 AP scenario* **(b)** *2 APs scenario*

Figure 5.8: *Secrecy capacity of the ADR situated under AP as a function of a ED's position.*

To compare the VLC secrecy performance of the proposed ADR prototype, the mean SeCap is determined for scenarios where the legitimate receiver uses the ADR or a single PD receiver. Table 5.3 shows the results, which are obtained by averaging the SeCap values calculated for each potential ED position on the grid. Throughout these assessments, the legitimate receiver remains stationary directly beneath an AP (or one of the APs in the two-AP case). The results clearly indicate that the ADR enhances the average SeCap by approximately two times compared to the single PD receiver. The average SeCap with the ADR is 1.02 Mbps in the one AP

Table 5.3: *Averaged secrecy capacity of two receivers in two scenarios.*

	1 AP scenario	2 APs scenario
ADR	1.02 Mbps	745 kbps
Single PD	518 kbps	313 kbps

scenario, whereas in the two AP scenario, it is 745 kbps. In contrast, the single PD receiver achieves SeCap values of 518 kbps and 313 kbps for one AP and two AP, respectively. The SeCap in the one AP scenario is higher, as the use of two APs results in a more pronounced improvement of the ED's SNR compared to the legitimate user's SNR, thereby diminishing overall system secrecy.

5.3.1.3 BER Distribution and Coverage Rate

The BER performance is evaluated at 2 Mbps and subsequently compared to that of the single PD receiver. BER is measured with the same setup as the SNR measurement. Using the equation (3.22) as previously detailed in 3.4.2.3, the BER coverage is determined. Table 5.4 presents the coverage rates for both ADR and single PD configurations in the two-AP scenario. The ADR prototype achieved a coverage rate of 50.41%, with 61 out of 121 points, effectively encompassing half of the area. This marks an enhancement exceeding 35% from the prior result of 37.19% as reported in Section 4.4.3.2. For the single PD receive, the coverage rate reached 26.45%, reflecting an expansion of about 52% compared to previous work, which reported a rate of 17.36%. These findings indicate that the proposed system extends the coverage area where effective communication is feasible.

Table 5.4: *Coverage rate (%) of ADR and the single PD.*

Receiver	Coverage rate (%)	
	This prototype	Prior work 4.4.3.2
ADR	50.41	37.19
Single PD	26.45	17.36

5.3.2 System Performance

The performance of the integrated VLC-RF system is illustrated with the ADR for IoT sensor networks. To demonstrate availability, sensor data transmission, image data transmission, and a practical application of robot arm system integration are presented.

5.3.2.1 Sensor Data Transmission

Sensor data transmission is a typical IoT application for sensor networks. Sensor data is captured by sensor modules and stored in IoT devices. The sensor data are gathered in AP by wireless links to understand the environment and status of the IoT devices.

To evaluate the IoT capability of the proposed system, sensor data transmission is assessed via the VLC and RF link. The system configuration used for this experiment is illustrated in Fig. 5.9. In the figure, three distinct pathways are evaluated. In Path1, the AP sends data from the microSD card upon request by the UN, which receives it through the VLC DL. For Path2, utilising both VLC and RF, after a UN request, the AP retrieves saved sensor data from the Wi-Fi cloud. In Path3, using a connection through IR, the UN sends data captured by its sensor to the AP, which then transfers it to the cloud using the RF link. Fig. 5.10 shows the sequence chart involved in accessing the SD card and the cloud through Path1 and Path2. The response time, defined as the interval from request reception to transmission start, is measured to evaluate latency performance. The DL data packet design allows a maximum packet size of 256 bytes, constrained by the UART protocol's serial buffer. The packet comprises a header

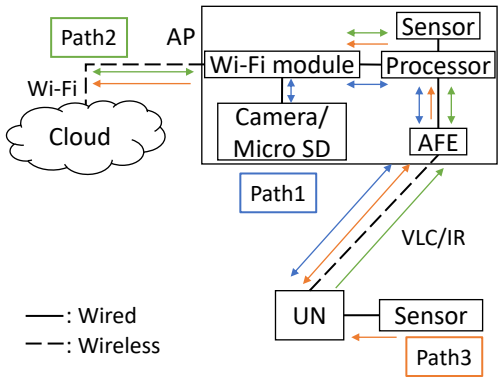

Figure 5.9: *Sensor data transmission System structure.*

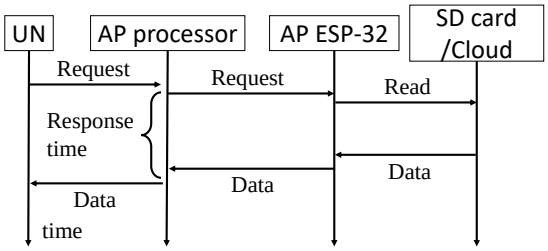

Figure 5.10: *Sequence chart of Path1 and Path2.*

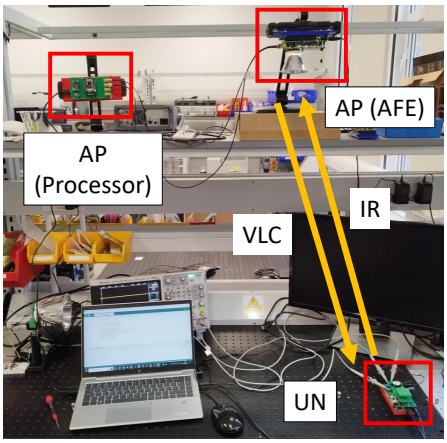

Figure 5.11: *Sensor data transmission experiment setup.*

(4 bytes), payload (max. 240 bytes), and trailer (3 bytes), improved from the prior 200-byte size as depicted in Fig.4.18 in Section 4.4.4. The sensor data transmission experiment setup is shown in Fig. 5.11. Fig. 5.12 shows the response times based on the varying numbers of data packets in Path1 and Path2. Three forms of sensor data are transmitted, including light intensity, temperature, and humidity. The response time in Path1 increases linearly from 5.5 ms to approximately 13 ms. In contrast, Path2 exhibits significantly higher latency, ranging from 1.3 to 2.7 seconds due to Wi-Fi connectivity delays. Fig. 5.13 shows an example of temperature data transmitted as a signal and received from the cloud at the UN via Wi-Fi and VLC.

In Path3, the AP acquires sensor data destined for cloud storage. Data transfer occurs from the UN through an IR uplink. Fig. 5.14 provides the sequence chart of Path3. Metrics such as RTT,

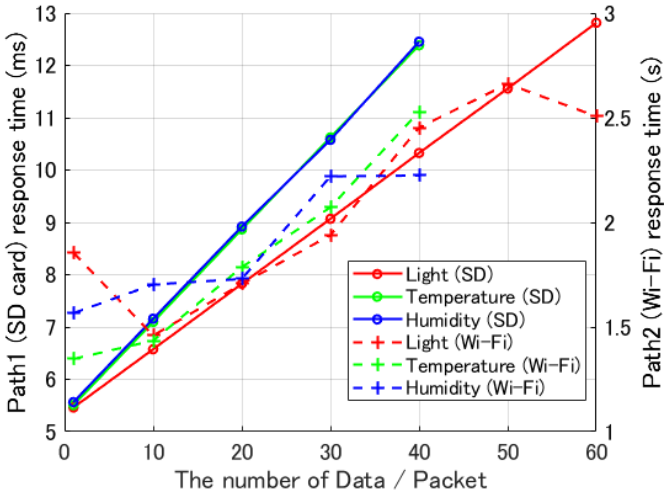

Figure 5.12: *Response time at Path1 (SD card) and Path2 (Wi-Fi).*

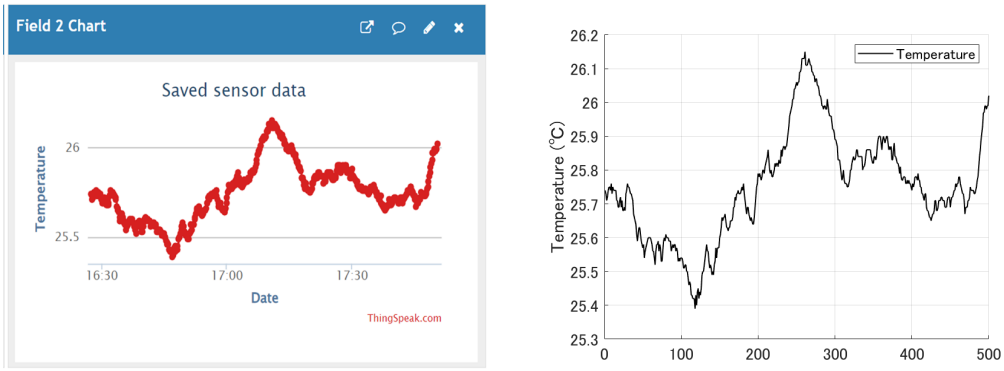

(a) *Cloud data* **(b)** *Received data*

Figure 5.13: *Temperature data transmitted via Path2.*

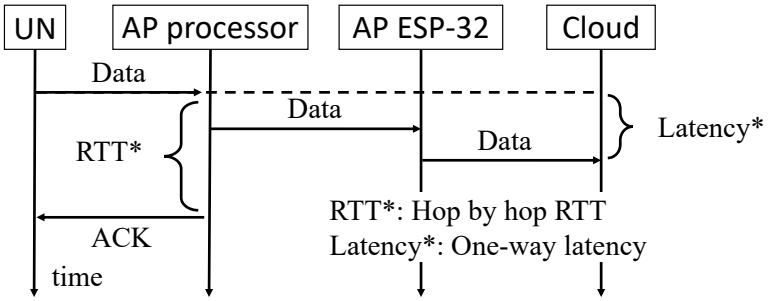

Figure 5.14: *Sequence chart of Path3.*

which involves the time for the UN to receive an ACK from the AP, alongside the one-way latency from the UN to the cloud, are measured to assess the time delay performance of the prototype. The elapsed time for Path3 is illustrated in Table 5.5. The average RTT over 10 iterations is 1.2 ms, with a variation between 0.45 and 4.69 ms. The average one-way latency for the UN to the cloud path over Wi-Fi is 0.27 s, ranging from 0.16 s to 1.17 s. Fig. 5.15 illustrates the cloud monitoring application that uses ThingSpeak functionality to show the UN status. The monitoring system includes a sensor value chart, the most recent value received,

Table 5.5: *The elapsed time of Path3.*

	Round trip time	One-way latency
10 times average	1.20 ms	0.27 s
Max	4.69 ms	1.17 s
Min	0.45 ms	0.16 s

and a status indicator light that changes based on the value. A green light is activated when the sensor value exceeds the cloud-defined threshold of 300 lx. In this setup, a value that falls below the threshold signals an abnormal condition at the UN, such as a low-light emergency. Consequently, the activation of the red light alerts the remote operator about the emergency through the cloud interface. The experiment demonstrates that incorporating VLC/IR and RF technologies facilitates remote monitoring applications for IoT sensor nodes.

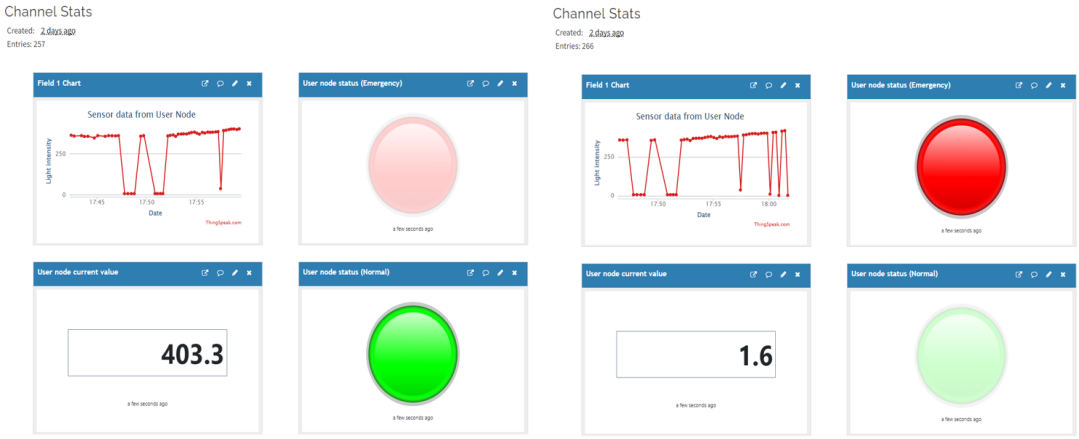

(a) *Status of green* **(b)** *Status of red*

Figure 5.15: *Cloud monitoring application.*

5.3.2.2 Image Transmission

In addition to sensor data transmission, image transmission is also considered typical IoT application for monitoring. Image data is captured by camera modules and stored in IoT devices. The image data received from UN is used to understand the surrounding environment of the IoT devices.

The process of transmitting images through a downlink is detailed. An image, once captured by the camera module, is stored on the SD card of the AP. Upon a request from the UN, the image is transmitted. After reception, the image data can be displayed on the laptop monitor connected to the UN. To process the image data into the UART based designed packet, it must be fragmented to fit within the payload. The transmission of images is non-continuous due to limitations intrinsic to UART, as provided by the camera module, supporting the JPEG image file format. A significant issue in image transmission is signal distortion, attributed to the high pass filter (HPF) in the receiver. A JPEG image comprises the start of image, segments,

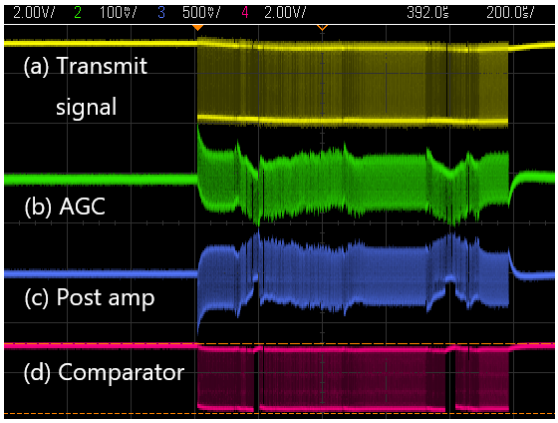

Figure 5.16: *Signal distortion of image data packet due to low frequency.*

image data, and end of image. The start and end of image are two-byte start and end markers, respectively. The segments contain crucial data necessary for image restoration. The received segments will suffer distortion due to low-frequency data being removed by the HPF in the UN receiver, as illustrated in Fig. 5.16. This figure presents the initial packet of the image as received during each transmission phase. Due to the distortion introduced by HPF, the UN receiver does not demodulate the OOK signal. HPF cannot be changed to ease the impact of distortion because HPF is set to optimise AGC in the following stage. Therefore, methods such as scrambling or bit insertion are needed to transmit image data using UART.

In this investigation, the scrambling technique known as Fisher-Yates shuffle [159] is applied, as outlined in the Algorithm 2 found in the appendix A. This choice is due to its straightforward implementation on a MCU, without the additional non-data-carrying bits, which are introduced by a bit insertion method. Although line encoding methods such as 64b/66b can be considered, they are not suitable in this case, because scrambling is performed on a bit basis rather than a byte basis, and line encoding methods require additional header bits as overhead. To illustrate the functioning of the scrambling method, two approaches are compared: the first (Scramble1) scrambles each packet divided from the image array, whereas the second (Scramble2) scrambles the entire image array before division into packets. The flow diagrams in Fig. 5.17 depict the application of the Fisher-Yates shuffle on (a) a divided payload and (b) the entire data array. Fig. 5.18 presents the successive number of the same symbols and the variance within the first packet payload. In this figure, the original packet shows more than 70 consecutive bits of the identical symbol with a variance close to 13, indicating a low frequency. In particular, Scramble2 reduces this count to fewer than 15 consecutive identical symbols, with a variance

of 2, whereas Scramble1 achieves a reduction to below 20, with a variance of 5. Both scrambling techniques feature comparable complexity and do not introduce redundancy into the data packets. Consequently, Scramble2 is employed in this experiment to demonstrate the image

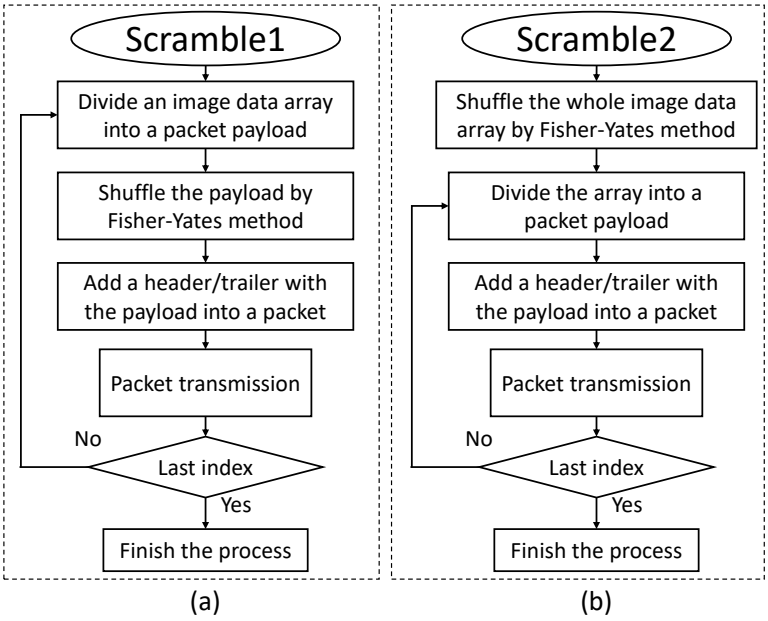

Figure 5.17: *Flowcharts of the shuffle method (a) each payload shuffle (b) the whole array shuffle.*

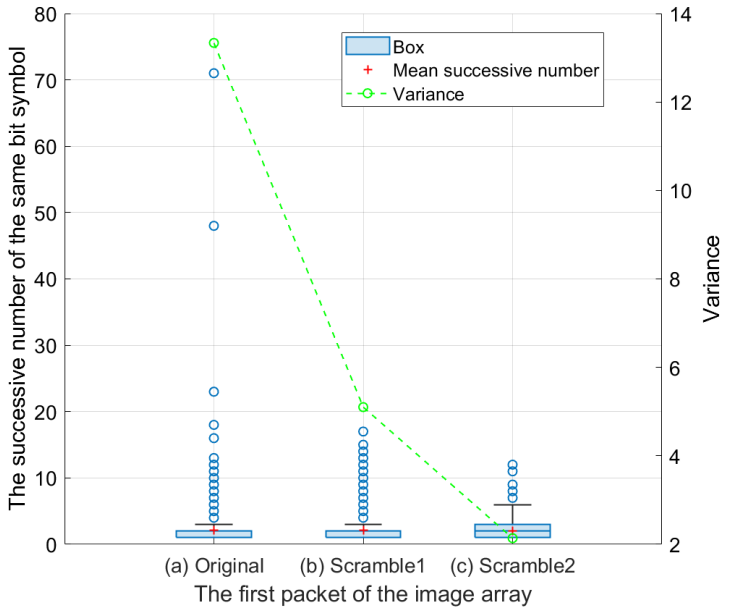

Figure 5.18: *Box charts of the first packet of Image.*

transmission capability. Fig. 5.19 displays images received via an VLC downlink, using the setup detailed in Fig. 5.11. The image data size is restricted to approximately 10,000 Bytes due to the limited memory capacity of the MCU. The received image contains no errors in critical segment information or data payload.

(a) *Image 1* **(b)** *Image 2*

Figure 5.19: *Received image via VLC.*

5.3.2.3 Robot Arm Integration

IoT applications require system cooperation with IoT devices by utilising sensor data for system functions. In industrial IoT scenarios, the cooperative function can be applied in manufacturing operation such as robot arm operations. The system integration with a robot arm can realise functions such as emergency reaction.

Integration of the system with a robot arm is exemplified in an industrial IoT context. As a practical instance of IoT applications, the designed system is implemented in conjunction with robot arm operations. Fig. 5.20 illustrates the configuration of the integrated VLC/RF system linked with the robot arm. Within this framework, the robot arm controller interfaces with the UN, primarily to manage the robot arm operations and to wait for instructions from the UN. Upon sensor data exceeding a predefined threshold, the UN issues a directive to the robot arm system. There exist two pathways: the VLC downlink (Path4) and the Wi-Fi cloud (Path5). In Path4, when the sensor module detects a value that reaches the threshold, the AP processor dispatches a command through the VLC downlink to the UN, which subsequently relays the trigger to the robot arm controller, causing the arm to stop operation. Meanwhile, in Path5, the triggered event occurs within the Wi-Fi cloud, initiated when sensor data uploaded to the cloud via Wi-Fi from the AP surpasses the threshold. The IoT cloud service, ThingSpeak, offers

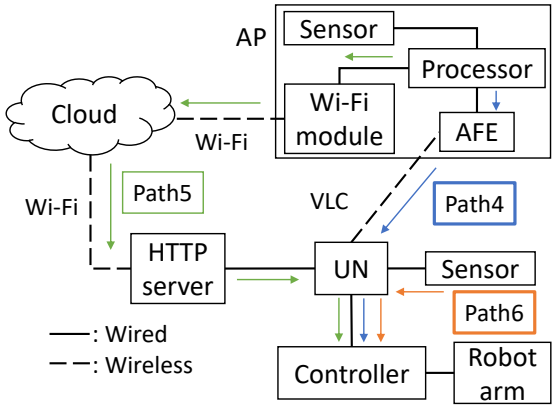

Figure 5.20: *System structure of the robot arm integration.*

functionalities to monitor stored data and facilitates HTTP connectivity for device communication. When the stored data satisfy specified criteria, a react app activates predetermined actions. Once an action is activated, the HTTP connection application forwards a trigger command to an HTTP server set up on a laptop PC connected to the UN, which then informs the UN of the trigger, prompting the UN to direct the robot arm through the controller. Fig. 5.21 illustrates the sequence diagrams corresponding to each pathway: (a) Path4, (b) Path5, and (c) Path6. To evaluate the performance metrics of each path, RTT or one-way latency is measured. For Path4, RTT measurement is conducted at AP with ACK from the robot arm. The latency in one direction for Path5 is measured via a Wi-Fi connection from the AP processor to the robot arm. A fully wired RTT measurement for Path6 is taken between the UN and the robot arm.

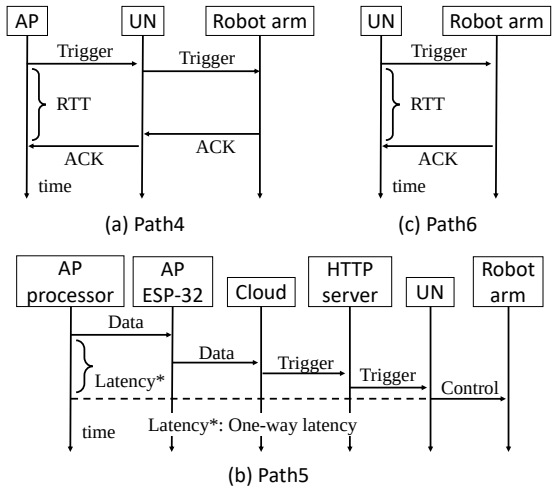

Figure 5.21: *Sequence charts of the robot arm system integration: (a) Path4, (b) Path5 and (c) Path6.*

Fig. 5.22 shows the setup of the system integration experiment with the robot arm. The elapsed times with measurements of 10 times are presented in Table 5.6. The average elapsed time for Path4 is 6.21 ms, with a variation between 1.41 ms and 10.12 ms. In particular, Path6, due to its fully wired configuration from the UN sensor to the robot arm, records the fastest average time of 4.12 ms. In contrast, the average one-way delay for Path5 is the longest at 10.11 s. The maximum delay reached 48.07 s due to the best-effort communication of the Wi-Fi connection, which does not ensure the delivery speed. This validates that incorporating hybrid VLC-RF techniques establishes a reliable IoT system by taking advantage of both methods.

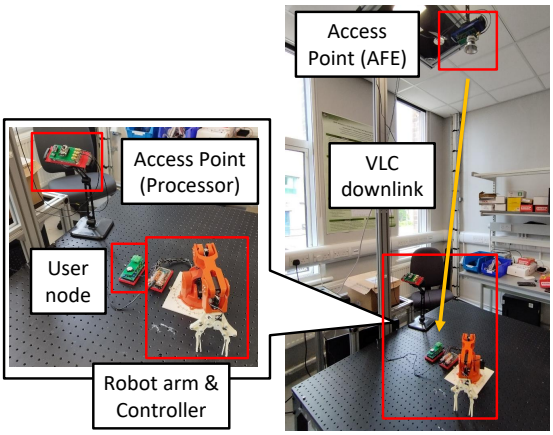

Figure 5.22: *Experiment setup of the system integration with the robot arm.*

Table 5.6: *The elapsed time of each path.*

	VLC (Path4)	WI-Fi (Path5)	Wired UN (Path6)
10 times average	6.21 ms	10.11 s	4.12 ms
Max	10.12 ms	48.07 s	8.52 ms
Min	1.51 ms	1.682 s	0.28 ms

5.4 Summary

In this chapter, the integrated VLC-RF system was proposed to demonstrate real-time IoT applications with enhanced coverage using the custom-built ADR. The prototype integrated an improved AFE from the previous chapter with an MCU, focussing on the IoT architecture from the nodes to the WAN via an AP. Extending previous work on a VLC prototype with an ADR, this chapter improved the system by incorporating RF connectivity to create a robust, integrated

VLC-RF system capable of supporting hybrid applications and demonstrating the comprehensive scope of VLC-IoT across WANs.

The chapter examined the performance of an integrated VLC-RF system using an ADR prototype, focussing on both the fundamental performance and the system performance to demonstrate its feasibility for application. Fundamental performance metrics included BER and SNR coverage, comparing current results with previous prototypes. Evaluating SNR in scenarios with one and AP, for a single AP, the ADR yielded an average SNR of 12.96 dB, surpassing the single PD's 8.20 dB but exhibiting more variance. In the dual AP configuration, ADR reached an average SNR of 15.32 dB, exceeding the single PD's 10.44 dB, and demonstrated less variability than in the single AP scenario. The PLS evaluation based on the measured SNR indicated that the designed ADR transceiver can support communication with double SeCap with 1.02 Mbps for the scenario of 1 AP and 518 kbps for 2 APs scenario. BER performance was assessed in a comparable manner, demonstrating that the ADR prototype enhances coverage. In the dual AP setup, the ADR achieved 50. 41% coverage, a notable increase compared to previous results, whilst a single PD reached 26. 45% coverage. This suggested that the proposed architecture provides more extensive communication coverage.

Furthermore, to demonstrate system performance, sensor data transmission, image data transmission, and integration of a robot arm system were all implemented and evaluated. In the result of the delay measurement, the minimum RTT was 0.45 ms (1.20 ms on average) and the AP response time was also on the order of milliseconds depending on the size of the packet. The results showed that the VLC path has lower latency than the Wi-Fi path due to network delays. Image transmission faced challenges such as signal distortion, addressed through a scrambling technique, with it being the most effective in reducing low-frequency data issues. The integration of the robot arm illustrated the application of the system in industrial IoT, using both VLC and Wi-Fi for command transmission. The latency performance varied, with millisecond order for VLC and longer latency by Wi-Fi. The hybrid VLC-RF framework enhanced the reliability of the system by leveraging the strengths of each communication method. The demonstration indicated the feasibility of reliable duplex connectivity with an integrated VLC-RF in IoT sensor networks.

Chapter 6

ADR Performance enhancement with Wavelength Division Multiplexing

6.1 Introduction

A promising technique for increasing the data transmission capacity of visible light communication (VLC) is the application of wavelength division multiplexing (WDM). Research in this area typically achieves WDM by using multi-colour light emitting diodes (LEDs) or laser diodes for transmission and photodiodes (PDs) for reception [105, 160–166]. In the receiver, optical components such as colour filters or dichroic mirrors are used to separate the light and direct each colour channel to its own dedicated PD. However, this approach presents challenges for implementation because the use of these optical components for colour separation increases the overall size of the receiver. Furthermore, the need for a separate PD for each channel often results in systems that are best suited for stationary fixed operation, limiting its application. To advance the performance and applicability of VLC, there is a clear need for compact, mobile-ready WDM-based VLC systems, particularly for Internet of Things (IoT) applications.

As the final technical chapter to demonstrate the potential for the development of VLC using angular diversity receiver (ADR), a WDM based ADR prototype is presented. To apply WDM, the PDs that constitute the ADR are red, green and blue (RGB) colour PDs. These RGB PDs enable WDM by detecting multiplexed signals through the RGB channels transmitted from the RGB LED transmitter. The ADR structure is designed for this RGB colour PD, including the 3D model. The shape of the ADR is the same square frustum (SF) type as in Chapter 5 and Chapter 6, and the ADR gets benefits from equal gain combining (EGC). The RGB LEDs that serve as transmitters become a single access point (AP) and transmit different data for each colour. At the receiver, the simultaneously transmitted signals, each with a different wavelength for the three colours, are detected by the RGB colour PD and subsequently demodulated. In the experiment, bit error rate (BER) and SINR are measured to evaluate the performance of WDM using the custom-built ADR and to analyse its feasibility. Furthermore, as a demonstration,

it is confirmed that different sensor information could be transmitted using each of the RGB channels and received without interference problems.

The remainder of this chapter is organised as follows; The model of the WDM based ADR system is discussed in Section 6.2; experimental results are presented in Section 6.3; and the conclusions are drawn in Section 6.4.

6.2 WDM based ADR System

The proposed WDM-based ADR system is described in this section. A block diagram of the proposed WDM-based ADR system is shown in Fig. 6.1. The figure shows that the system consists of transceivers for AP and user node (UN). The AP is primarily composed of an microcontroller unit (MCU), an analogue front end (AFE), a three-colour LED, and an infrared (IR) PD. Data from sensors connected to MCU, or from an SD card, is transmitted by WDM to downlink (DL) using the three-colour LED. The AP employs an interactive protocol, receiving requests from the UN uplink (UL) via the IR PD and responding accordingly. The UN, on the other hand, consists of an MCU, an AFE, an ADR that utilises a three-colour PD, and an IR LED. The UN uses its IR LED to make UL transmission requests and receives data from AP. Although the data streams are transmitted simultaneously, they are separated by different wavelengths at the receiver. This allows for the demodulation of the distinct data for each channel, even in the presence of interference from the other colours. The received data are then verified on a laptop PC connected to the UN's MCU. The AFEs in both the AP and the UN are designed to handle the transmission and reception of three-channel signals.

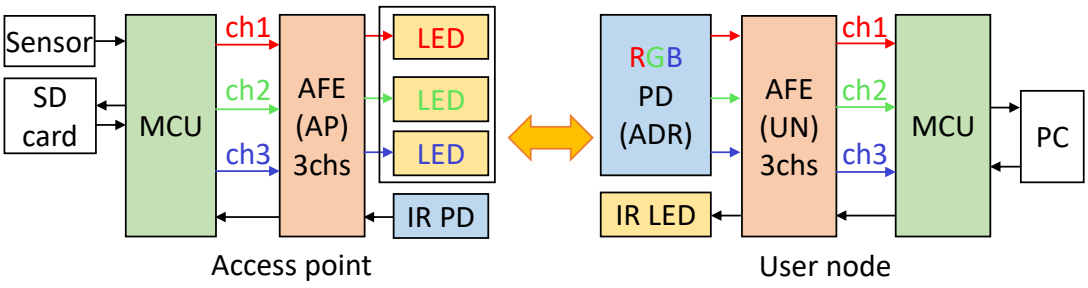

Figure 6.1: *Block diagram of the proposed WDM based ADR system.*

6.2.1 Analogue Front End Design

This section describes the design of AFE for AP and UN. The AP employs a RGB colour LED and therefore includes a three-channel transmission system as well as a reception system for the IR PD. To perform WDM transmission, UN has a three-channel receiving system for each wavelength. The design is optimised for the implementation of printed circuit board (PCB) operating with MCU.

6.2.1.1 Transmitter

The circuit design for channel 1 of the transmission system is shown in Fig. 6.2. The same transmitter design is included in the AP AFE for the other channels. The RGB LED selected from OSRAM LED (LZ4-00MD09) has dominant wavelengths of 630, 525, and 450 nm in red, green and blue, respectively [167]. Fig. 6.3 illustrates the spectrum emission from the datasheet of the RGB LED. The MCU universal asynchronous receiver/transmitter (UART) output is connected to Vout1 in the diagram. The transmitter consists of an operational amplifier (OPA810) and a transistor (2SK306ST100), which together form a constant current source circuit. The LED is connected to J101 and the current is drawn from the 9 V power supply line. The magnitude of this current is determined by the value of resistor R104, which is different for each colour channel. The current driving LED is calculated using the equation: $I_{\text{LED}} = \frac{V_{out1}}{R_{104}}$. The resistance values for channels 1 through 3 are 5.1, 10 and 6.8 Ω, assigned to green, blue, and red, respectively. The voltage across LED, V_{LED}, can be determined from the I-V curve on

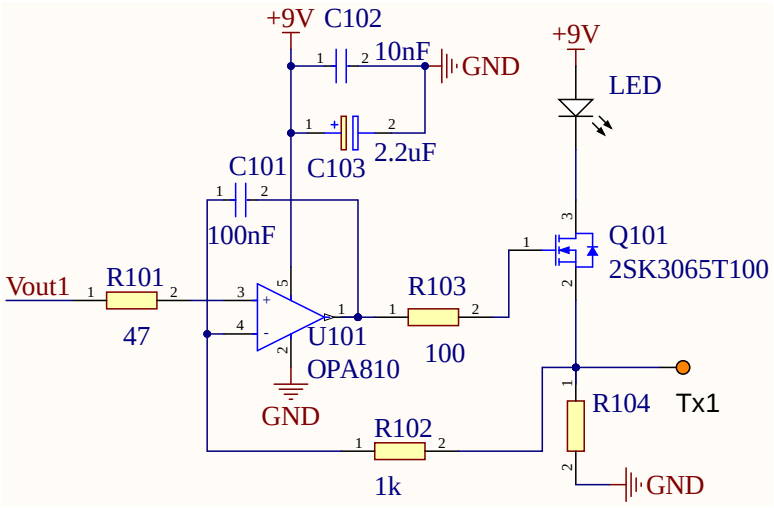

Figure 6.2: *The transmitter design of Channel 1.*

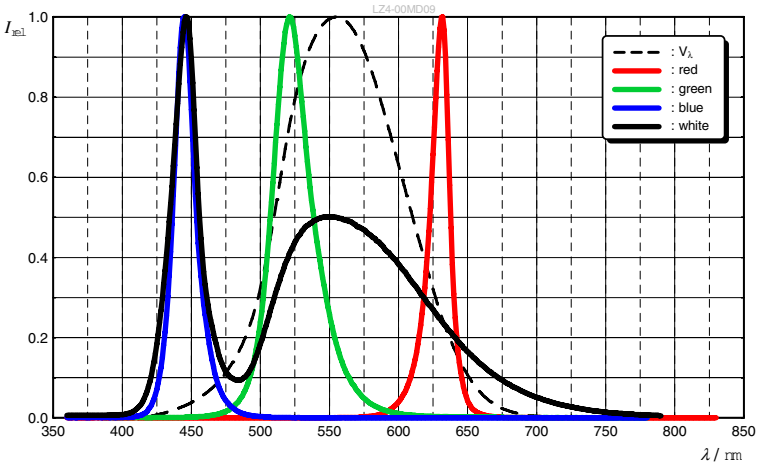

Figure 6.3: *Spectrum emission of the RGB LED (LZ4-00MD09) trimmed from the datasheet.*

its data sheet [167], which in turn allows calculation of its power consumption. Given that the voltage in R104 is 3.27 V (nearly identical to the Vout1 voltage), the driving currents, I_{LED}, for channels 1 to 3 are calculated as 0.641 A, 0.327 A and 0.481 A, respectively. From the I-V curve, the corresponding V_{LED} is 2.72 V, 2.84 V, and 2.24 V. This results in electrical power of LEDs of 1.74 W (green), 0.93 W (blue), and 1.08 W (red). The upper limit of the driving current is determined by the stable operating range of the transistor, whilst the total current for all three channels is constrained by the AC adapter's capacity. In this design, the total LED driving current is 1.45 A. The AC adapter can supply 2 A, providing sufficient headroom. However, the final current values are set according to safe operating area specified in the transistor data sheet [168]. The safe operating area indicates the maximum drain current allowed for a given drain-to-source voltage, V_{DS}. V_{DS} is found by subtracting the LED forward voltage and the voltage across R104 from the power supply voltage, V_{s}, as shown in the equation:

$$V_{\mathrm{DS}} = V_{\mathrm{s}} - V_{\mathrm{LED}} - V_{\mathrm{out1}} \tag{6.1}$$

Using (6.1), the V_{DS} for channels 1 to 3 is calculated as 3.01 V, 2.89 V, and 3.49 V. According to the data sheet, the maximum drain current must be below 0.7 A at 3 V and below 0.5 A at 4 V. Since the drain current is identical to the forward current of LED, I_{LED}, the circuit has been designed to ensure that all operating currents remain safely within these limits of safe operating area.

6.2.1.2 Receiver

The AFE of the UN is made up of a three-channel reception system and a transmission system that utilises an IR LED. The circuit design of the UN receiver is shown in Fig. 6.4. It features three reception lines, all implemented on a single-layer AFE. In the circuit design, the connectors of J101, J201, and J301 are connected to PDs for each respective colour. A single receiver channel consists of a transimpedance amplifier (TIA), voltage amplifier, and comparator, and low pass filters (LPFs) are used as appropriate to remove out-of-band noise components. The TIA converts the current signal from the PD into a voltage signal, which is then amplified by the subsequent amplifier stage. Finally, this amplified signal is converted into a 1 bit digital signal by the comparator and fed to the UART port of the MCU. The RGB colour PD used in this study is S9032-02 from HAMAMATSU [169]. As shown in Fig. 6.5, the spectral response range in nm is 400 to 540 for blue, 480 to 600 for green, and 590 to 720 for red with the peak sensitivity wavelength of 460, 540 and 620 nm, respectively. Some spectral range overlaps a spectral band of different colours PD, resulting in interference in the WDM application. The photosensitivity of blue, green, and red is typically 0.18, 0.23 and 0.16 A/W. The red PD has the weakest photosensitivity. The typical rise time is 0.2 μs with a maximum of 1.0 μs.

The TIA is configured in photoconductive mode, unlike the connection method described in the previous chapter, Chapters 4 and 5, called the photovoltaic mode. This approach is chosen to achieve a faster response speed and higher photosensitivity, which improves the PD characteristics by applying a reverse bias voltage across it. The applied reverse bias widens the PD's internal depletion region, which in turn reduces its junction capacitance. This decrease in

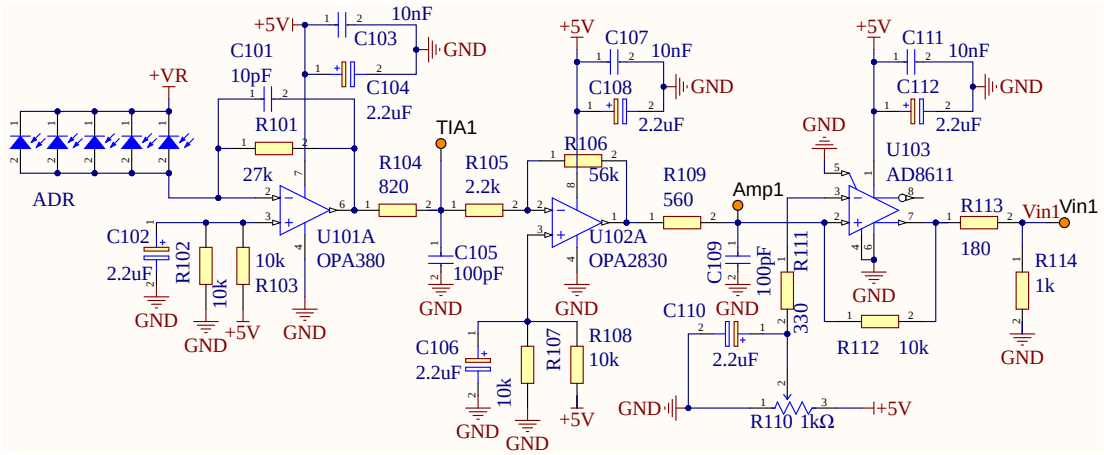

Figure 6.4: *Receiver circuit diagram for each channel of the WDM receiver.*

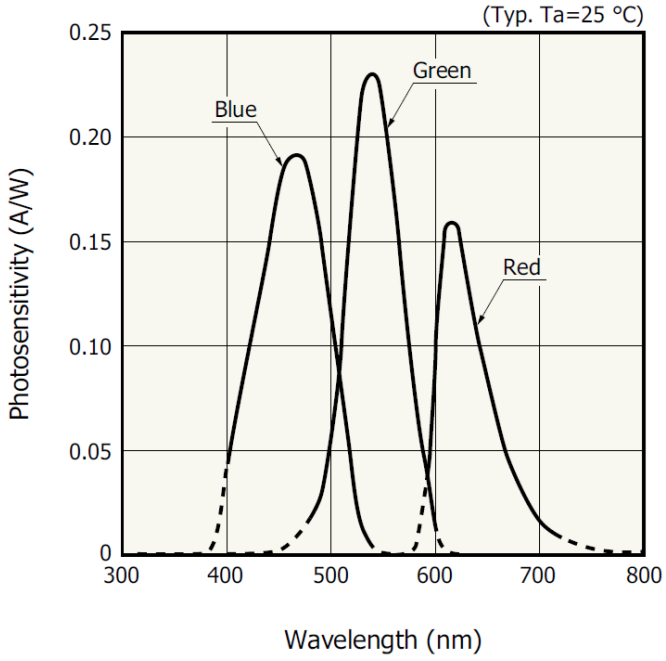

Figure 6.5: *Spectrum response of the RGB PD (S9032-02) trimmed from the datasheet.*

capacitance leads to a smaller RC time constant, which improves response speed. Additionally, the wider depletion region allows the generation of more photocurrent, resulting in increased sensitivity. The TIA in this mode is configured specifically because the chosen PD has relatively low photosensitivity with around 0.2 A/W and limited response speed with a rise time of up to 1.0 μs. However, it must be noted that applying a reverse bias also leads to an increase in dark current, which contributes to higher noise levels. The bandwidth of TIA on channel 1 can be calculated using the following equation, which was previously presented in Section 4.3.2:

$$f_{-3\text{dB}} = \sqrt{\frac{\text{GBP}}{2\pi(C_{\text{T}})R_{101}}} \qquad [\text{Hz}] \tag{4.5}$$

Using (4.5), the bandwidth is designed to achieve the maximum possible gain whilst still accommodating the UART baud rate of 1 Mbps. As a result, with a feedback resistor (R_{101}) of 27 kΩ, the bandwidth is designed to be 2.4 MHz. The gain of the subsequent inverting amplifier stage can be calculated for channel 1, using the formula $G = -\frac{R_{106}}{R_{105}}$. Using the component values shown in the circuit diagram, the gains for the first two channels are 28.1 dB, whilst the gain for channel 3 is 21.8 dB. Channel 3 is assigned to the red colour; its gain is set lower to avoid saturation, as its bias voltage tends to be higher than the other channels. This saturation is considered to be caused by ambient light, which contains more red-coloured elements com-

pared to others. LPFs are connected to the output of both the TIA and the amplifier stages in the three channels. The cut-off frequency, for example for LPF after channel 1 TIA, is calculated as $f_c = \frac{1}{2\pi R_{104} C_{105}}$. The resulting cut-off frequencies of LPF after TIA and the amplifier of channel 1 are 1.94 MHz and 2.84 MHz, respectively. The comparator design is the same as described in Section 5.2.1, with the hysteresis window set to 32 mV. All components used in this design, including resistors and capacitors, are surface mount device (SMD) type components for small-size implementation.

6.2.2 The ADR Design

The design of the engineered ADR is described here. The 3D model is shown in Fig. 6.6 (all dimensions are in mm). As shown in the side view, the side-mounted PDs have a tilt angle of 30°. This design expands the overall field of view (FOV) and creates an overlap between the individual fields, helping to improve reception sensitivity. The ADR measures 37.21 mm in length and width, with a height of 14.39 mm. The mounting slots for the PDs are custom-designed to match the dimensions of the specific PD used.

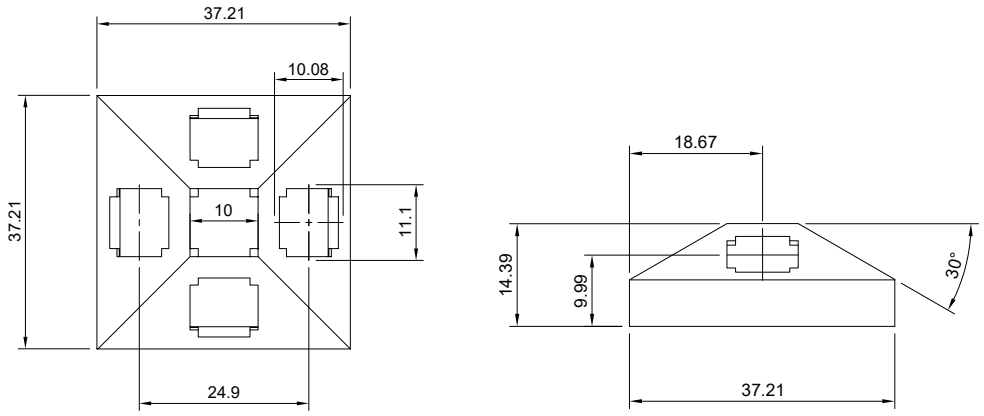

(a) *Top view* **(b)** *Side view*

Figure 6.6: *3D model of the designed ADR.*

6.2.2.1 FOV Evaluation

It is necessary to measure FOV experimentally because the data sheet for the RGB colour PD used in this study does not specify its FOV. Furthermore, as illustrated in Fig. 6.7, the photo-sensitive area of PD of 2 mm diameter is divided into three distinct segments. This physical

configuration results in a different FOV for each of the RGB channels. Therefore, FOV of a single PD and ADR needs to be measured and compared to analyse them. Fig. 6.8 shows the components that are manufactured using a 3D printer of the designed model. The evaluation setup of the single PD receiver consists of one PD fitted into the top slot of the ADR housing.

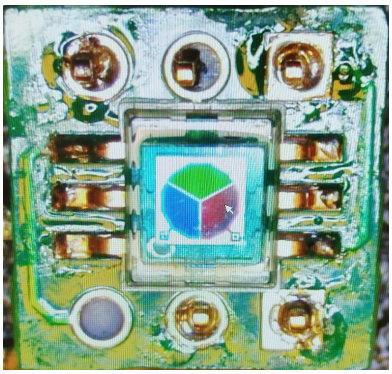

Figure 6.7: *Extended image of the RGB colour PD applied in this study.*

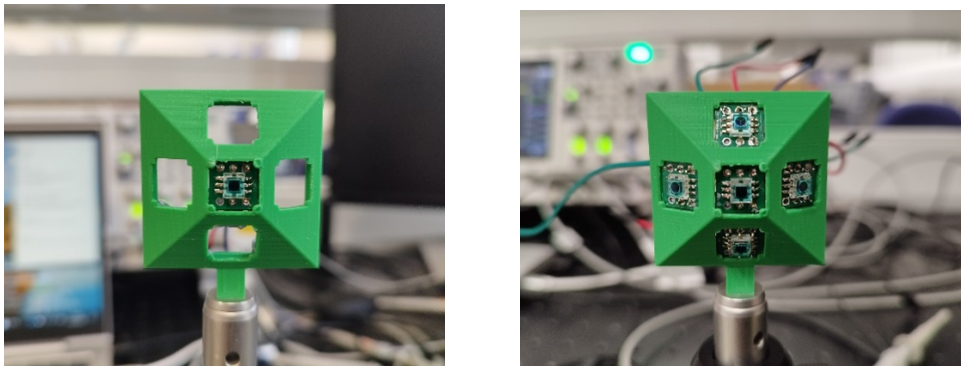

(a) *Single PD* **(b)** *ADR*

Figure 6.8: *ADR/Single PD receiver prototype.*

Fig. 6.9 shows the normalised received voltage versus the angle, which is measured to determine the FOV for each of the three colours. Fig. 6.9a presents the measurement results for a single PD. The maximum received voltages for RGB are 700 mV, 380 mV, and 860 mV, respectively. These values have been normalised by setting the maximum voltage for each colour to 1. Due to the fan-shaped photosensitive area of the PD shown in Fig. 6.7, the peak voltage of the blue colour is approximately -20°. Although the peak voltage of the red colour is at 0°, its overall distribution is shifted toward positive angles. The green photosensitive area extends laterally from the centre; resulting in a distribution that gradually decreases around the 0° axis. To determine the FOV from these results, the half-power beamwidth is considered.

The half-power beamwidth refers to the angular range in which the received power is half of its maximum. In terms of voltage, this is calculated where the voltage is $\frac{V_{\max}}{\sqrt{2}} \approx 0.707 \times V_{\max}$. Therefore, the FOV is the angular width between the points where the normalised voltage is 0.707. The resulting FOVs for the single PD are approximately $80°$, $90°$, and $98°$ for the RGB, respectively. The combined FOV of the ADR is obtained from Fig. 6.9b with approximately $110°$, $90°$, and $98°$ for RGB, respectively. With the exception of the red colour, the FOV itself does not change significantly. However, the maximum received voltage of the ADR is considerably improved, at more than 1 V for each channel (Red: 1.09 V, Green: 1.13 V, Blue: 1.33 V). This improvement occurs because the FOVs of the side-mounted PDs overlap, allowing the signals from each PD to be effectively combined. Furthermore, the FOV curve of the ADR is smoother than that of the single PD receiver, which has the rattling curve.

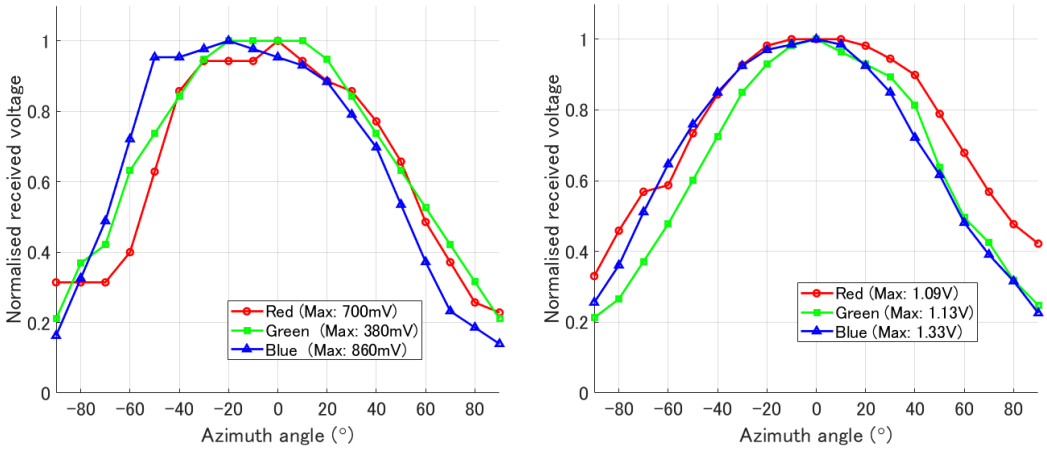

(a) *Single PD* **(b)** *ADR*

Figure 6.9: *Azimuth angle versus normalised received voltages of the single PD and ADR.*

6.3 Experimental Results

This section presents the experimental results using the designed WDM-based ADR system. The UN prototype, which is composed of PCBs manufactured according to the design described in Section 6.2, is shown in Fig. 6.10a. The UN PCB has a two-layer structure consisting of a AFE layer directly connected to MCU and a mounting layer with ADR and IR LEDs. The ADR has five PDs embedded, each with four pins for RGB and GND. A total of 20 wires from the ADR assembly are connected to the PCB's mounting layer. In Table 6.1, the steady-state power consumption for the ADR, AP processor, and AP AFE is recorded as 1.34 W, 0.50 W,

and 14.00 W, respectively. Active-state power usage, assessed during data transmission, remains comparable to idle levels due to the brief transmission intervals attributed to the compact UART protocol packet design. The AP AFE provides the power to drive three channels of RGB LED, resulting in increased consumption. Fig. 6.10b shows the experimental setup using the designed prototype. Using this configuration, the fundamental performances of BER, signal-to-noise ratio (SNR) versus distance, and signal-to-interference-plus-noise ratio (SINR) are evaluated. Furthermore, the results of transmitting and receiving data obtained from the prototype's onboard sensors via WDM are also presented as a demonstration. In these experiments, the data rate for each colour channel is set at 1 Mbps. This is due to the limit of rise time (maximum 1 µs) of the RGB colour PDs used.

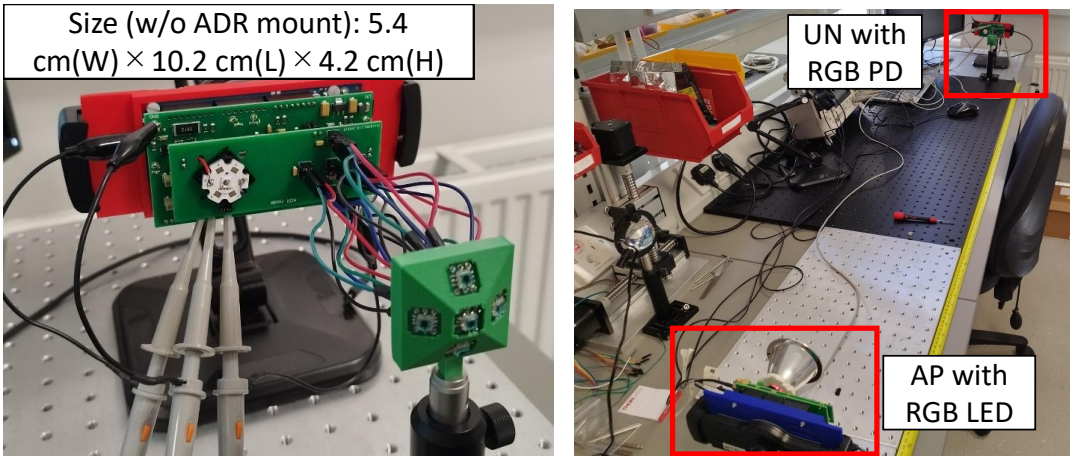

(a) *ADR user node prototype.* **(b)** *Experiment setup.*

Figure 6.10: *Prototype and experiment setup.*

Table 6.1: *Power consumption of the prototype in Watt.*

State	ADR	AP (Processor)	AP (AFE)
Idle	1.34	0.50	14.00
Active	1.34	0.51	13.80

6.3.1 The Fundamental Evaluation

In this section, the fundamental performances of the prototype, including its BER, SNR, and SINR, are measured for evaluation. These performances are compared to those of a single PD receiver to demonstrate the advantages of ADR. Furthermore, the measured SINR results are

presented in the presence of interference inherent in a WDM system.

6.3.1.1 BER and SNR against Distance

The measurement results for BER and SNR as a function of distance are shown in Fig. 6.11. Looking at SNR, all three colours are approximately 22 dB at 0.5 m for the single PD receiver. These SNR values for RGB with a single PD decrease with increasing distance, falling to around 12 dB at 1 m. For the ADR system, SNR at 1 m is 17 dB for red and around 23 dB for the other two colours. At a distance of 2.6 m, SNR decreased to 5 dB for red and 9 dB for the other two colours. The BER for the single PD receiver begins to degrade at distances beyond 0.9 m. The maximum transmission distance at the forward error correction (FEC) limit (3×10^{-3}) is 0.9 m (red), 0.92 m (green) and 1.1 m (blue), respectively. In contrast, with ADR, BER degradation begins at 1.8 m for red and 2.2 m for green and blue. The distances to the FEC limit are 1.85 m (red), 2.35 m (green), and 2.38 m (blue). From these results, it is indicated that for the single PD, BER degradation begins when SNR drops below 14 dB, whereas for the ADR it begins when SNR is below 12 dB. The lower SNR for the red channel is due to the lower gain described in Section 6.2.1, and the lowest photosensitivity, but also because for the same driving current, its I-V curve corresponds to a lower driving voltage. This results in a lower transmission power compared to the other colours. From the BER measurements, it is confirmed that the proposed ADR system can achieve error-free transmission on the three

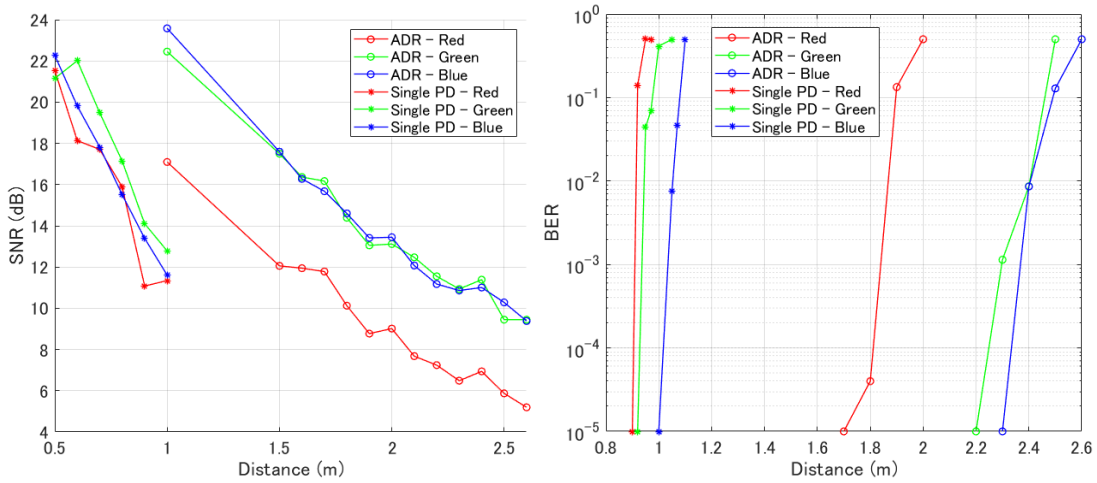

(a) *SNR vs distance.* **(b)** *BER vs distance..*

Figure 6.11: *The performance of the WDM system with single PD and designed ADR.*

channels up to a distance of 1.7 m.

6.3.1.2 SINR Evaluation

In a WDM transmission system, signals from other colour channels act as interference, which degrades SINR. Therefore, SINR is measured in the presence of interference from the other colours channels to confirm that reliable communication is still possible. Fig. 6.12 illustrates the measured signal waveforms with and without interference. In Fig. 6.12a, the signal transmitted when other channels are inactive is shown, and Fig. 6.12b shows the signal received at various stages of the receiver chain in this interference-free case. The waveform transmitted when other channels are active simultaneously is shown in Fig. 6.12c. These channels transmit square waves at the same baud rate, creating interference to the signals of channel 1. Fig. 6.12d shows the waveforms at each receiver stage with interference present. It is clear that the signals at the TIA and the subsequent amp are distorted by this interference. Despite this distortion, the comparator's output shows that the signal is still successfully demodulated into a 1-bit digital signal without any issues. This signal measurement result confirms the viability of

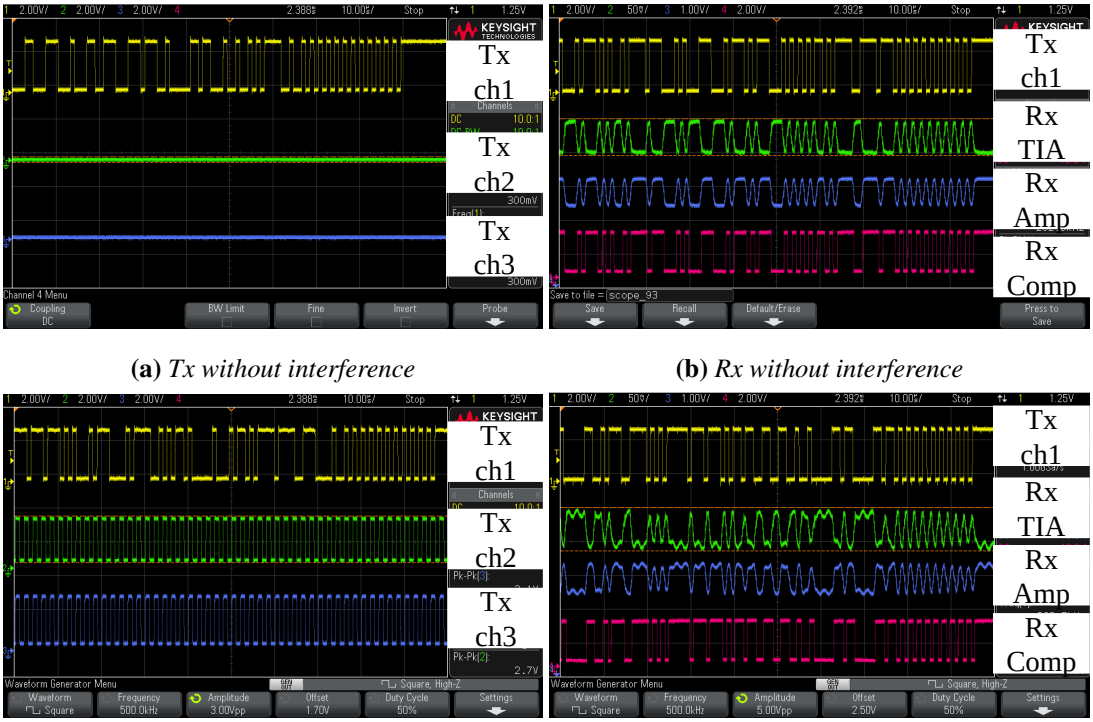

(a) *Tx without interference* **(b)** *Rx without interference*

(c) *Tx with interference* **(d)** *Rx with interference*

Figure 6.12: *Measured signals with / without interference.*

applying WDM. Fig. 6.13 shows the SINR and standard deviation of the received voltage induced by interference against the voltage of the transmitted interference signal for the ADR. These measurements are taken at a distance of 1.5 m for the ADR, where BER is error-free. In this figure, the horizontal axis represents the voltage of the transmitted interference signal (that is, the other two colours), which is varied from 0 V to 5 V using a signal generator. The peak-to-peak voltage, V_{pp}, of the desired signal is kept constant at 3.27 V. The left axis shows the result SINR in dB, and the right axis shows the standard deviation of the received voltage, σ_V, of the interference signal. As expected, SINR decreases as the transmitted interference voltage increases. This is a direct result of the increase in received interference σ_V. When the transmitted interference voltage is 0 V, SINR is identical to SNR. The SINR of the red channel remains almost constant regardless of the interference voltage. This is because the σ_V for red barely increases up to σ_V of 0.015 V. The reason for this is the excellent spectral separation between the red channel and the other two colours in both the RGB LED's emission and the PD's spectral response. In contrast, the blue and green channels have some spectral overlap, so as the interference between them increases, their received σ_V also increases, causing a decrease in SINR. Even at maximum interference voltage, the BER for all channels remained error-free. This result strongly confirms the practical applicability of WDM to the proposed system.

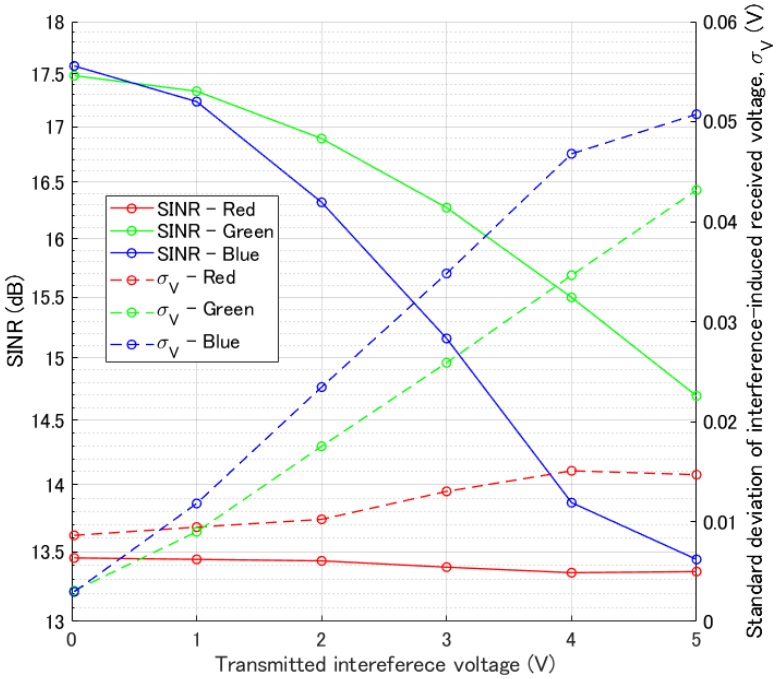

Figure 6.13: *SINR and standard deviation of interference-induced received voltage, σ_V with different interference voltages measured at 1.5 m for ADR.*

6.3.2 Sensor Transmission

In this section, WDM transmission of sensor data is demonstrated that can be successfully transmitted and received using the prototype's onboard sensors. The implemented sensors measure light, humidity, and temperature and each sensor data is assigned to a specific colour channel for multiplexed transmission. Fig. 6.14 shows the waveforms measured of each colour during WDM transmission. In Fig. 6.14a, the green, blue, and red channels are from top to bottom. Data from light intensity (Lux), humidity, and temperature sensors are placed into packets for transmission. The channel transmission does not start at the exact same moment; there is a delay of 12.2 μs between each channel. This is due to the sequential characteristic of the UART processing. However, once the last channel is active, all channels transmit simultaneously, resulting in interference with one another. Fig. 6.14b shows the signals received after they have been converted to digital signals by the receiver comparator. It is clear that each channel is demodulated successfully, even in the presence of interference from the other colour channels. This result demonstrates the practical viability of applying WDM to the system. Using WDM, a combined aggregate data rate of 3 Mbps is achieved, which is three times the rate possible on a single channel. Fig. 6.15 shows the serial monitors for the transmitter and receiver as displayed on a laptop. Fig. 6.15a shows the three values of the sensor data transmitted for light, temperature, and humidity, whilst Fig. 6.15b displays the data received. The matching values of the transmitted and received sensor data provide clear confirmation that the WDM transmission works correctly.

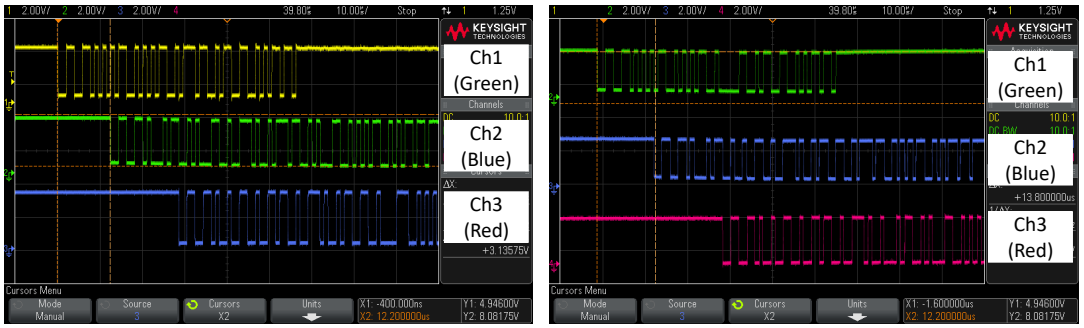

(a) *Signals at the transmitter side* **(b)** *Signals at the receiver side*

Figure 6.14: *Measured signals of WDM transmission.*

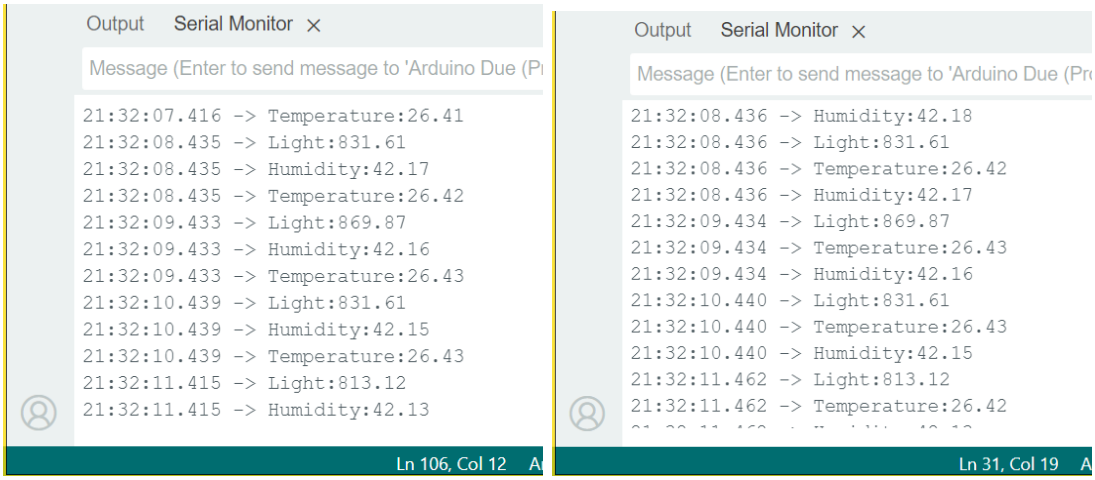

(a) *Tx* **(b)** *Rx*

Figure 6.15: *Excerpt of the Serial Monitor of Arduino IDE.*

6.4 Summary

In this chapter, experimental studies were conducted by designing and evaluating a prototype ADR that uses WDM. The ADR structure and AFE for a transceiver were designed, using a RGB LED and a RGB colour PD for WDM application. Using the fabricated prototype, its fundamental performance was measured and its data transmission capabilities confirmed. Performance evaluation included measurements of BER, SNR, and SINR in the presence of interference from signals of different wavelengths. The results showed that the system could maintain an error-free BER even with interference, demonstrating that an aggregate data rate of 3 Mbps across the three channels is achievable and that WDM is a viable approach. Furthermore, data from prototype onboard sensors were successfully transmitted via WDM and confirmed that the correct values were received. Therefore, it was shown that WDM transmission using an ADR with a RGB LED and colour PDs is feasible. By applying this technique, the data rate can be tripled compared to a non-WDM system with a single channel, demonstrating the significant potential for WDM to further advance the performance of ADR-based systems.

Chapter 7
Conclusion and Outlook

This chapter provides a comprehensive overview of the research discussed in this thesis, focussing on the main discoveries and the consequent conclusions. In addition, the chapter will articulate the constraints encountered in this research, paving the way for suggestions on prospective avenues for further investigation.

7.1 Summary of the Work

In response to the growing demand for the radio frequency (RF) spectrum, visible light communication (VLC) is emerging as a promising technology for replacing or complementing RF systems. It is particularly anticipated for use in RF-sensitive environments and for applications such as industry. This thesis focusses on theoretical research and experimental validation of VLC systems designed for Internet of Things (IoT) applications. The motivation and objectives of this research were introduced in chapter 1. Chapter 2 then provided a historical background of VLC, an overview of current research trends, and a summary of its key advantages and challenges. It also described the fundamental transmission model, outlined the components of a VLC transceiver, presented the derivation of the channel model and concluded with a review of recent literature.

In chapter 3, the performance of angular diversity receiver (ADR) configurations was first analysed. ADR types with different number of photodiodes (PDs) were focused on in downlink multi-cell scenarios. Through numerical analysis and simulation, the ADR performance with the derived optimal tilt angle was assessed using spatial multiplexing (SMP) and receive diversity techniques, including selection combining (SC), equal gain combining (EGC) and maximum ratio combining (MRC). The results in the application of SMP indicated that the hexagonal frustum (HF) ADR provides the widest coverage with approximately 87 $\%$ for multi-stream transmission due to its largest number of PDs. However, for receive diversity, the hexagonal ADR configurations with six-sided PDs did not outperform the square types with four-sided PDs in terms of bit error rate (BER) performance when using SC due to the

increase in noise. The SC scheme, with more than 90 % coverage rate for BER of 1×10^{-6}, is the most promising due to the lower impact of inter-cell interference (ICI), although EGC and MRC with the square frustum (SF) ADR have narrower coverage of about 50 % and 75 %, respectively.

Subsequently, in Chapter 4, the performance of ADR was analysed in single-cell environments, leading to the development of a novel ADR system designed for VLC applications within IoT sensor networks. The prototype, which features both the custom-built ADR and the designed analogue front end (AFE), was developed to improve communication performance with respect to coverage. The numerical analysis applying the combining techniques indicated that any combination of ADR types and diversity techniques can enhance performance without significant differences. Consequently, an SF ADR was implemented with the EGC due to its simplicity and sufficient performance. The newly proposed ADR system successfully ensured error-free communication at 1 Mbps up to a distance of 4.2 m, whilst also elevating the signal-to-noise ratio (SNR) and reducing the BER and extending the link coverage to more than twice that achieved by a single PD receiver. Furthermore, its practical benefits were confirmed through real-time sensor data transmission and a duplex VLC communication system, underscoring its efficacy in actual IoT scenarios.

In Chapter 5, the integrated VLC and RF (VLC-RF) system using ADR was presented for secure industrial IoT systems. The ADR based VLC prototype was designed to connect to the backbone network such as a wireless cloud server. As the fundamental performance of VLC, the SNR and BER coverage was improved, and the link coverage was drastically expanded compared to the initial design in Chapter 4. For scenarios with a single access point (AP), the average SNR for the ADR was 12.96 dB, which is higher than 8.20 dB for a single PD. In a dual AP setup, the ADR achieved an average SNR of 15.32 dB, surpassing the single PD's 10.44 dB, and showed less variance than the single AP setup. The physical layer security (PLS) analysis based on the SNR results indicated that the designed ADR can support secure communication with the double secrecy capacity (SeCap) compared to that of the single PD receiver. SeCap of the proposed ADR was 1.02 Mbps/745 kbps for 1 AP/2 APs scenarios. BER analysis was conducted similarly, indicating that the ADR prototype enhances coverage. In the dual AP configuration, the ADR covered 50.41%, a significant improvement over the previous results, whereas the single PD coverage reached 26.45%. Furthermore, to evaluate the feasibility of the IoT application, real-time sensor network applications using the proposed integrated VLC-RF

ADR system were demonstrated. These experiments, including real-time sensor transmission, image transmission, and integration of the robot arm system, indicated the benefits in a practical scenario by showing low latency. The delay measurements revealed a minimum round-trip time (RTT) of 0.45 ms and an average of 1.20 ms, with AP response time generally around milliseconds, depending on the size of the packet. The findings indicated that the VLC path experiences less latency than the wireless fidelity (Wi-Fi) path due to network-induced delays. Signal scrambling effectively addressed challenges like image transmission distortion and reduces low-frequency data problems. The integration of the robot arm demonstrated the applicability of the system in industrial IoT, using both VLC and Wi-Fi for command transmission. Latency varied; VLC maintained millisecond order, whilst Wi-Fi incurred greater delays. The hybrid VLC-RF architecture bolsters system reliability by capitalising on the strengths of each communication method.

Finally, in Chapter 6, the wavelength division multiplexing (WDM)-based VLC prototype was implemented. This was an additional experimental study to show the method for an ADR based multiplexing system using colour PDs. The BER performance of three different wavelength channels (red, green, blue) was shown in comparison with the single PD receiver. The results indicated that the system preserved an error-free BER despite interference, confirming that a combined data rate of 3 Mbps over three channels is achievable, thereby validating WDM's effectiveness. Furthermore, sensor data from the prototype was accurately sent through WDM, demonstrating the receipt of correct values. Thus, WDM transmission employing an ADR with red, green and blue (RGB) light emitting diodes (LEDs) and colour PDs is viable. This method allows for a three-fold increase in data rate compared to single-channel systems, highlighting WDM's capability to enhance ADR system performance.

7.2 Limitations and Future Work in the Area

This research has encompassed both theoretical studies and experimental validation to address the research gaps identified in Chapter 2. However, it is important to acknowledge that this work has certain constraints related to the assumed system models, the applied technologies, the specific hardware implemented, and the experimental environments. This final section, therefore, will outline the specific limitations of each chapter and suggest directions for future work.

The analysis study in Chapter3 was carried out using a single specific system model. Future work should therefore explore different system models. For instance, further technical insights could be obtained by varying the distance between LED transmitters or by increasing the number of transmitters to analyse multi-cell or multi-stream environments. The techniques, SMP and receive diversity, applied in this analysis were fundamental. Performance is anticipated to be further enhanced by the investigation of more advanced derivative technologies. Finally, this study was limited to four typical ADR shapes identified in the literature. A valuable area for future investigations would be to model different ADRs with a larger number of PDs and compare their performance under the same conditions.

The study in Chapter 4 used the same system model as in the previous chapter; therefore, more profound insights could be gained by investigating different models of a single-cell scenario. In single-cell analysis, whilst increasing the number of LED transmitters improves SNR and consequently enhances BER and coverage, the optimal number of transmitters depends on the system model. This trade-off warrants further investigation. The experimental validation is limited by the resources of the microcontroller unit (MCU) used as the base hardware platform. In this research, an Arduino DUE was used for signal processing and to supply power to the AFE. Although the AFE was optimised for this hardware, the use of a more advanced hardware platform could lead to further performance improvements. The key specifications of the Arduino DUE include an operating voltage of 3.3 V, a clock speed of 84 MHz, a main memory of 96 kB, and a power output of 800 mA from the 3.3 V/5.0 V DC pins. Although an external power source is an option, designs that rely on the MCU's power rails must keep the AFE's required current within this 800 mA limit. Furthermore, memory capacity can restrict the complexity of the operational code, though the programmes used in this chapter did not face such limitations. Future research could include applying combining techniques other than EGC or implementing SMP for multi-stream transmission. However, these more advanced techniques would be difficult to implement on an MCU with limited analogue-to-digital converter (ADC) performance. Therefore, exploring them would constitute a significant new research topic, likely requiring a more capable hardware platform.

The experiments in Chapter 5 were conducted using the same hardware resources as in Chapter 4 and are therefore subject to the same MCU performance constraints. A key difference in this chapter's prototype design is the implementation of a Wi-Fi module (ESP32-CAM) in the AP to support a wireless connection to a cloud service. As this module also has a camera, it

allows a demonstration of image-based applications. As part of the system demonstration, an image transmission was performed. This verification was constrained by the limited memory of the MCU, and as a result, the transmission of images with small size and low resolution could be confirmed. The scrambling technique proposed for image transmission over universal asynchronous receiver/transmitter (UART) requires a separate memory array for the scrambled data in addition to the array for the original image. To execute the programme, the image data size had to be carefully adjusted to fit within the MCU's available memory. Looking ahead, there are several areas for further consideration. With regard to RF module selection, there are numerous alternatives to Wi-Fi. Investigating which RF technology is most suitable would provide deeper insight into integrated VLC-RF systems. Furthermore, the IoT cloud service used in the experiments was the ThingSpeak free plan. The optimal cloud service would depend on the specific application being demonstrated, leaving significant room for future exploration in this area. Furthermore, larger-scale validation using multiple nodes in harsher industrial IoT environments, such as those with high levels of ambient light and aerosols. Power consumption in long-term operation should also be evaluated. Finally, to assess system robustness, there is scope to implement the remaining useful life prediction.

In Chapter 6, a WDM-based VLC system was developed using the same hardware resources as in Chapters 4 and 5. A primary hardware constraint of this study was the need to integrate a three-channel transmitter in a AP or receiver in an user node (UN) system into a single AFE. For the transmitter, it was challenging to find a balanced design that provided sufficient and equal transmission power for each of the three LED colour channels. Because each LED has a unique I-V curve, its final transmission power is determined by the current set in its constant current source circuit. However, balancing the power was difficult because the driving current is constrained by the main power supply limit (2 A) and the transistor's safe operating area. A key future task is to design a new transmitter that fully considers these issues in its hardware selection, power supply design, and component choice, which would enable more practical and robust validation. On the receiver side, due to size constraints, a simplified three-channel circuit was integrated, consisting of a transimpedance amplifier (TIA), amplifier, and comparator onto a single AFE. As a result, the automatic gain control (AGC) circuit and post-amplifier used in previous chapters were omitted. Performance could be improved by optimising the receiver circuit for each individual channel. The prototype of the ADR mount also has limitations. With 20 wires required to connect the ADR to the AFE, the resulting prototype was complicated and must be static, making it difficult to validate in mobile application scenarios. In future work, a

new ADR mount design is needed to solve the complex connectivity issue between the internal RGB PDs and the AFE. This would enable demonstrations in more practical and mobile environments. Furthermore, it was found that because of differences in photosensitivity and elements of ambient light, the red channel was prone to saturation. This forced the amplifier gain to be reduced, resulting in an unbalanced SNR across the channels. A future study should investigate solutions for the red channel's saturation problem. An improved prototype could then be demonstrated with a revised circuit design that achieves a comparable SNR on all channels. Finally, whilst experiments were conducted to measure WDM performance with interference and demonstrated sensor data transmission, there is still significant scope for future work, including transmission tests with various media, such as images and videos, extending this research to a multi-user experimental setup to demonstrate a multi-access network by applying wavelength division multiple access (WDMA).

Appendix A
Scramble Function

This appendix describes the scrambling function, which is a reference in Section 5.3.2.2

Algorithm 2 Scramble Function

```
1:  procedure SCRAMBLE(input, output, size, seed)
2:      randomSeed(seed)
3:      indices ← malloc(size * sizeof(int))
4:      if indices == NULL then
5:          while (1);
6:      end if
7:      for i ← 0 to size − 1 do
8:          indices[i] ← i
9:      end for
10:     for i ← size − 1 down to 1 do
11:         j ← random(0, i + 1)
12:         temp ← indices[i]
13:         indices[i] ← indices[j]
14:         indices[j] ← temp
15:     end for
16:     for i ← 0 to size − 1 do
17:         output[i] ← input[indices[i]]
18:     end for
19:     free(indices)
20: end procedure
```

Appendix B
Receiver circuit of the WDM-based VLC system

This appendix describes the overall receiver design of three channels for WDM, which is a reference in Section 6.2.1.2

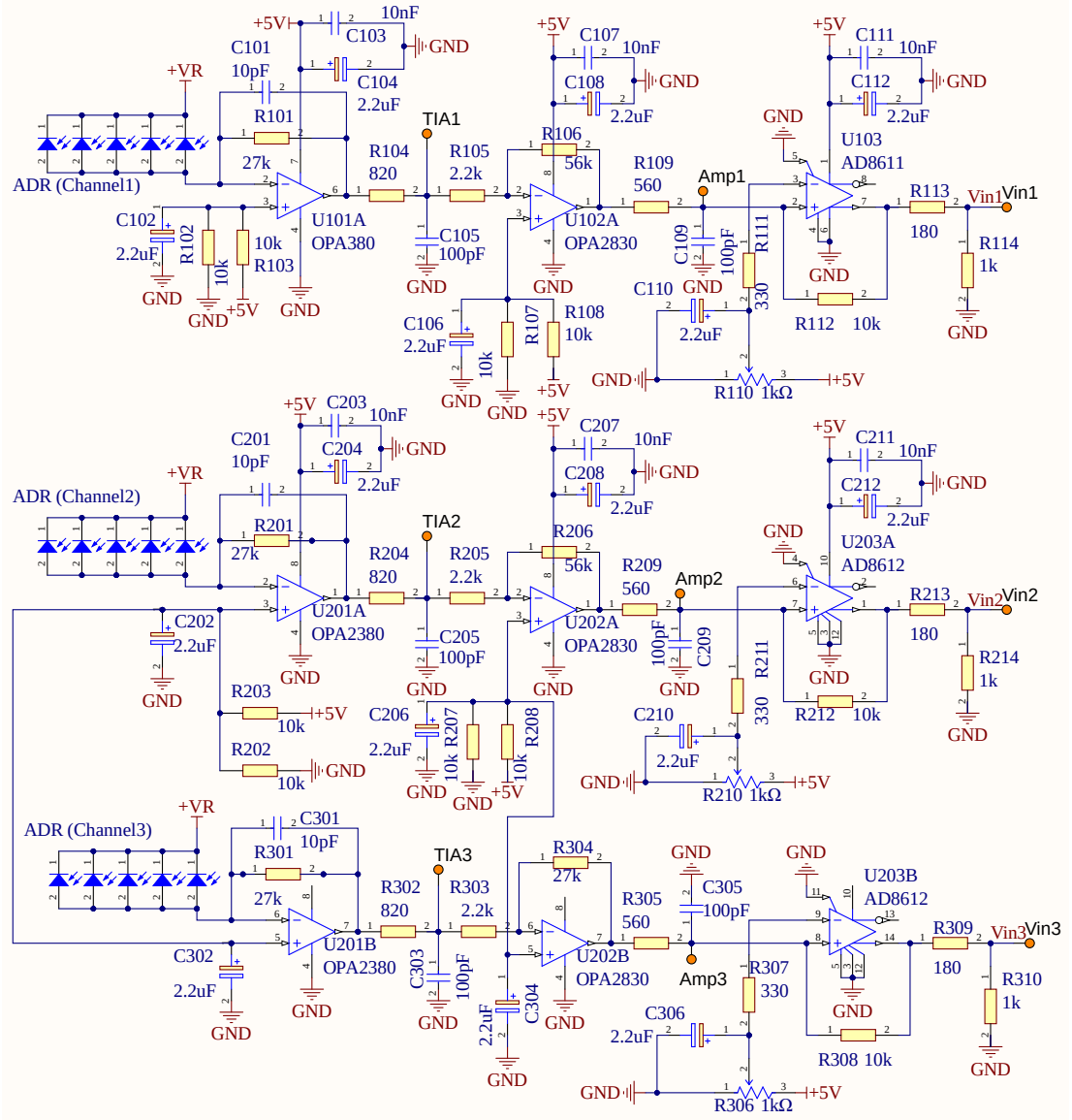

Figure B.1: *The receiver design of three channels.*

References

[1] Cisco, "Internet of Things At a Glance." Available at: https://www.audentia-gestion.fr/cisco/pdf/at-a-glance-c45-731471.pdf, 2016. Technical report, Accessed 09-Mar-2025.

[2] S. Alfattani, "Review of LiFi technology and its future applications," *Journal of Optical Communications*, vol. 42, no. 1, pp. 121–132, 2021.

[3] M. Katz and I. Ahmed, "Opportunities and Challenges for Visible Light Communications in 6G," in *2020 2nd 6G wireless summit (6G SUMMIT)*, pp. 1–5, IEEE, 2020.

[4] S. De Lausnay, L. De Strycker, J.-P. Goemaere, B. Nauwelaers, and N. Stevens, "A survey on Multiple Access Visible Light Positioning," in *2016 IEEE International Conference on Emerging Technologies and Innovative Business Practices for the Transformation of Societies (EmergiTech)*, pp. 38–42, IEEE, 2016.

[5] E. Illi, M. Qaraqe, S. Althunibat, A. Alhasanat, M. Alsafasfeh, M. De Ree, G. Mantas, J. Rodriguez, W. Aman, and S. Al-Kuwari, "Physical Layer Security for Authentication, Confidentiality, and Malicious Node Detection: A Paradigm Shift in Securing IoT Networks," *IEEE Communications Surveys & Tutorials*, vol. 26, no. 1, pp. 347–388, 2023.

[6] Cisco, "Cisco Industrial IoT Portfolio." Available at: https://www.cisco.com/c/dam/en/us/solutions/collateral/internet-of-things/industrial-iot-portfolio-brochure.pdf, 2024. Technical report, Accessed 09-Mar-2025.

[7] Y. Almadani, D. Plets, S. Bastiaens, W. Joseph, M. Ijaz, Z. Ghassemlooy, and S. Rajbhandari, "Visible light communications for industrial applications—Challenges and potentials," *Electronics*, vol. 9, no. 12, p. 2157, 2020.

[8] M. Ayyash, H. Elgala, A. Khreishah, V. Jungnickel, T. Little, S. Shao, M. Rahaim, D. Schulz, J. Hilt, and R. Freund, "Coexistence of WiFi and LiFi toward 5G: concepts, opportunities, and challenges," *IEEE Communications Magazine*, vol. 54, no. 2, pp. 64–71, 2016.

[9] A. Makvandi, Y. S. Kavian, and E. Namjoo, "VLCIoT: design and implementation of a visible light communication system for indoor Internet of Things applications," *Applied Optics*, vol. 60, no. 36, pp. 11094–11103, 2021.

[10] H. Zhou, M. Zhang, and X. Ren, "Design and implementation of wireless optical access system for VLC-IoT networks," *Journal of Lightwave Technology*, vol. 41, no. 8, pp. 2369–2380, 2023.

[11] M. A. S. Sejan and W.-Y. Chung, "Performance Analysis of a Long-Range MIMO VLC System for Indoor IoT," *IEEE Internet of Things Journal*, vol. 10, no. 8, pp. 6999–7010, 2022.

[12] C. Lalani, H. Meena, L. Goyal, A. Mathur, and N. Bhatia, "Experimental Demonstration of Text and Audio Transmission over Single Channel and Relay Assisted VLC Systems," in *2024 14th International Symposium on Communication Systems, Networks and Digital Signal Processing (CSNDSP)*, pp. 137–141, IEEE, 2024.

[13] B. Turan, K. A. Demir, B. Soner, and S. C. Ergen, "Visible light communications in industrial internet of things (IIOT)," *The Internet of Things in the Industrial Sector: Security and Device Connectivity, Smart Environments, and Industry 4.0*, pp. 163–191, 2019.

[14] W. Zhang, L. Chen, X. Chen, Z. Yu, Z. Li, and W. Wang, "Design and realization of indoor VLC-Wi-Fi hybrid network," *Journal of Communications and Information Networks*, vol. 2, no. 4, pp. 75–87, 2017.

[15] P. Kamsula, "Design and implementation of a bi-directional visible light communication testbed," Master's thesis, P. Kamsula, 2015.

[16] S. Yin, N. Smaoui, M. Heydariaan, and O. Gnawali, "Purple VLC: Accelerating Visible Light Communication in Room-Area through PRU Offloading," in *EWSN*, pp. 67–78, 2018.

[17] Y. Liu, X. Liu, X. Mu, T. Hou, J. Xu, M. Di Renzo, and N. Al-Dhahir, "Reconfigurable intelligent surfaces: Principles and opportunities," *IEEE communications surveys & tutorials*, vol. 23, no. 3, pp. 1546–1577, 2021.

[18] P. Fahamuel, J. Thompson, and H. Haas, "Improved Indoor VLC MIMO Channel Capacity Using Mobile Receiver with Angular Diversity Detectors," in *2014 IEEE Global Communications Conference*, pp. 2060–2065, IEEE, 2014.

[19] H. B. Eldeeb, H. A. Selmy, H. M. Elsayed, and R. I. Badr, "Interference mitigation and capacity enhancement using constraint field of view ADR in downlink VLC channel," *IET Communications*, vol. 12, no. 16, pp. 1968–1978, 2018.

[20] M. Román Cañizares, P. Palacios Játiva, C. A. Azurdia-Meza, S. Montejo-Sánchez, and S. Céspedes, "Impact of diversity combining schemes in a multi-cell VLC system with angle diversity receivers," *Photonic Network Communications*, vol. 43, no. 1, pp. 13–22, 2022.

[21] M. Hosney, H. A. Selmy, A. Srivastava, and K. M. Elsayed, "Interference Mitigation Using Angular Diversity Receiver With Efficient Channel Estimation in MIMO VLC," *IEEE Access*, vol. 8, pp. 54060–54073, 2020.

[22] C. Chen, W.-D. Zhong, H. Yang, S. Zhang, and P. Du, "Reduction of SINR Fluctuation in Indoor Multi-Cell VLC Systems Using Optimized Angle Diversity Receiver," *Journal of Lightwave Technology*, vol. 36, no. 17, pp. 3603–3610, 2018.

[23] A. Nuwanpriya, S.-W. Ho, and C. S. Chen, "Indoor MIMO Visible Light Communications: Novel Angle Diversity Receivers for Mobile Users," *IEEE Journal on selected areas in communications*, vol. 33, no. 9, pp. 1780–1792, 2015.

[24] V. Dixit and A. Kumar, "Performance analysis of angular diversity receiver based MIMO–VLC system for imperfect CSI," *Journal of Optics*, vol. 23, no. 8, p. 085701, 2021.

[25] S. Chatterjee and B. Roy, "Multi-parameter optimization of a hemispheric angle diversity receiver to reduce SINR fluctuation for an indoor MIMO-VLC system," in *2021 4th Biennial International Conference on Nascent Technologies in Engineering (ICNTE)*, pp. 1–6, IEEE, 2021.

[26] J. A. Simpson, B. L. Hughes, and J. F. Muth, "Smart Transmitters and Receivers for Underwater Free-Space Optical Communication," *IEEE Journal on selected areas in communications*, vol. 30, no. 5, pp. 964–974, 2012.

[27] M. Yuksel, J. Akella, S. Kalyanaraman, and P. Dutta, "Free-space-optical mobile ad hoc networks: Auto-configurable building blocks," *Wireless Networks*, vol. 15, pp. 295–312, 2009.

[28] Ericsson, "Ericsson Mobility Report November 2024." Available at: `https://www.ericsson.com/4adb7e/assets/local/reports-papers/mobility-report/documents/2024/ericsson-mobility-report-november-2024.pdf`, 2024. Technical report, Accessed 17-April-2025.

[29] Cisco, "5G Security Innovation with Cisco." Available at: `https://www.cisco.com/c/dam/en/us/solutions/collateral/service-provider/service-provider-security-solutions/5g-security-innovation-with-cisco-wp.pdf`, 2018. Technical report, Accessed 17-April-2025.

[30] Ericsson, "Quantifying the future impact of GenAI, June 2025." Available at: `https://www.ericsson.com/49d8ce/assets/local/reports-papers/mobility-report/documents/2025/emr-june-2025-genai-future-article.pdf`, 2025. Technical report, Accessed 26-August-2025.

[31] NTT, "White Paper 5G Evolution and 6G." Available at: `https://www.docomo.ne.jp/english/binary/pdf/corporate/technology/whitepaper_6g/DOCOMO_6G_White_PaperEN_v5.0.pdf`, 2023. Technical report, Accessed 17-April-2025.

[32] L. U. Khan, "Visible light communication: Applications, architecture, standardization and research challenges," *Digital Communications and Networks*, vol. 3, no. 2, pp. 78–88, 2017.

[33] S. U. Rehman, S. Ullah, P. H. J. Chong, S. Yongchareon, and D. Komosny, "Visible Light Communication: A System Perspective—Overview and Challenges," *Sensors*, vol. 19, no. 5, p. 1153, 2019.

[34] A. G. Bell, "The photophone," *Science*, no. 11, pp. 130–134, 1880.

[35] Y. Tanaka, S. Haruyama, and M. Nakagawa, "Wireless optical transmissions with white colored LED for wireless home links," in *11th IEEE International Symposium on Personal Indoor and Mobile Radio Communications. PIMRC 2000. Proceedings (Cat. No. 00TH8525)*, vol. 2, pp. 1325–1329, IEEE, 2000.

[36] T. Komine, "Basic study on visible-light communication using light emitting diode illumination," in *Proc. 8th Int. Symp. on Microwave and Optical Technology (ISMOT 2001), Montreal, Canada*, pp. 45–48, 2001.

[37] Y. Tanaka, "A basic study of optical ofdm system for indoor visible communication utilizing plural white leds as lighting," *ISMOT-2001 Montreal, Canada, June 19-23*, pp. 303–306, 2001.

[38] D. Tsonev, S. Videv, and H. Haas, "Light fidelity (Li-Fi): towards all-optical networking," in *Broadband Access Communication Technologies VIII*, vol. 9007, p. 900702, SPIE, 2014.

[39] IrDA, "Infrared Data Association (IrDA)." Available at: `https://www.irda.org/`, 1997. Accessed 7-May-2025.

[40] T. Yamazato, "Overview of visible light communications with emphasis on image sensor communications," in *2017 23rd Asia-Pacific Conference on Communications (APCC)*, pp. 1–6, IEEE, 2017.

[41] G. A. Mapunda, R. Ramogomana, L. Marata, B. Basutli, A. S. Khan, and J. M. Chuma, "Indoor Visible Light Communication: A Tutorial and Survey," *Wireless Communications and Mobile Computing*, vol. 2020, no. 1, p. 8881305, 2020.

[42] "IEEE Standard for Local and metropolitan area networks–Part 15.7: Short-Range Optical Wireless Communications," *IEEE Std 802.15.7-2018 (Revision of IEEE Std 802.15.7-2011)*, pp. 1–407, 2019.

[43] International Telecommunication Union, "ITU-T G.9991: High-speed indoor visible light communication transceiver - System architecture, physical layer and data link layer specification." Available at: `https://handle.itu.int/11.1002/1000/13781`, 2019. Accessed 8-May-2025.

[44] Institute of Electrical and Electronics Engineers, "IEEE 802.15.13-2023: IEEE Standard for Multi-Gigabit per Second Optical Wireless Communications." Available at: `https://standards.ieee.org/ieee/802.15.13/10269/`, 2023. Accessed 8-May-2025.

[45] pureLiFi, "Global LiFi Firms Welcome the Release of IEEE 802.11bb Global Light Communications Standard," 2023. Accessed 8-May-2025.

[46] L. Bravo Alvarez, S. Montejo-Sánchez, L. Rodríguez-López, C. Azurdia-Meza, and G. Saavedra, "A Review of Hybrid VLC/RF Networks: Features, Applications, and Future Directions," *Sensors*, vol. 23, no. 17, p. 7545, 2023.

[47] S. S. Oyewobi, K. Djouani, and A. M. Kurien, "Visible Light Communications for Internet of Things: Prospects and Approaches, Challenges, Solutions and Future Directions," *Technologies*, vol. 10, no. 1, p. 28, 2022.

[48] P. Wen, Y. Li, S. Chen, and S. Zhao, "Remaining Useful Life Prediction of IIoT-Enabled Complex Industrial Systems with Hybrid Fusion of Multiple Information Sources," *IEEE Internet of Things Journal*, vol. 8, no. 11, pp. 9045–9058, 2021.

[49] J. Li, K. Wang, X. Hou, D. Lan, Y. Wu, H. Wang, L. Liu, and S. Mumtaz, "A Dual-Scale Transformer-Based Remaining Useful Life Prediction Model in Industrial Internet of Things," *IEEE Internet of Things Journal*, vol. 11, no. 16, pp. 26656–26667, 2024.

[50] R. De Luca, A. Ferraro, A. Galli, M. Gallo, V. Moscato, and G. Sperli, "A deep attention based approach for predictive maintenance applications in iot scenarios," *Journal of Manufacturing Technology Management*, vol. 34, no. 4, pp. 535–556, 2023.

[51] J. H. Anajemba, C. Iwendi, I. Razzak, J. A. Ansere, and I. M. Okpalaoguchi, "A counter-eavesdropping technique for optimized privacy of wireless industrial iot communications," *IEEE Transactions on Industrial Informatics*, vol. 18, no. 9, pp. 6445–6454, 2022.

[52] A. Farraj, "Coordinated Security Measures for Industrial IoT Against Eavesdropping," in *2023 IEEE Texas Power and Energy Conference (TPEC)*, pp. 1–5, IEEE, 2023.

[53] M. Li, H. Yuan, C. Maple, Y. Li, and O. Alluhaibi, "Security Outage Probability Analysis of Cognitive Networks with Multiple Eavesdroppers for Industrial Internet of Things," *IEEE Transactions on Cognitive Communications and Networking*, vol. 8, no. 3, pp. 1422–1433, 2022.

[54] X. Zhao, Y. Zhao, J. Huang, W. Zhao, and J. Sun, "Physical-Layer Security for Indoor Hybrid PLC/VLC Networks With NOMA," *IEEE Open Journal of the Communications Society*, vol. 5, pp. 872–884, 2024.

[55] X. Liu, F. Xu, L. Ning, C. Zhao, and H. Xia, "A Novel Approach for the Enhancement of Security through Defining the Spatial Secrecy Outage Probability in the Industrial Internet of Things," *Electronics*, vol. 13, no. 12, p. 2356, 2024.

[56] H. Sadat, M. Abaza, A. Mansour, and A. Alfalou, "A Survey of NOMA for VLC Systems: Research Challenges and Future Trends," *Sensors*, vol. 22, no. 4, p. 1395, 2022.

[57] S. N. Ismail and M. H. Salih, "A Review of Visible Light Communication (VLC) Technology," in *AIP Conference Proceedings*, vol. 2213, AIP Publishing, 2020.

[58] S. Louvros and D. Fuschelberger, "VLC technology for indoor LTE planning," in *System-Level Design Methodologies for Telecommunication*, pp. 21–41, Springer, 2013.

[59] R. Wang, G. Niu, Q. Cao, C. S. Chen, and S.-W. Ho, "A Survey of Visible-Light-Communication-Based Indoor Positioning Systems," *Sensors*, vol. 24, no. 16, p. 5197, 2024.

[60] J. F. Gutiérrez and J. M. Quintero, "Visible Light Communication: A Short Review," *Revista Ontare*, vol. 10, 2022.

[61] Y. Almadani, M. Ijaz, S. Rajbhandari, B. Adebisi, and U. Raza, "Application of Visible Light Communication in an Industrial Environment," in *2018 11th International Symposium on Communication Systems, Networks & Digital Signal Processing (CSNDSP)*, pp. 1–6, IEEE, 2018.

[62] N. Farr, A. Bowen, J. Ware, C. Pontbriand, and M. Tivey, "An integrated, underwater optical/acoustic communications system," in *OCEANS'10 IEEE SYDNEY*, pp. 1–6, IEEE, 2010.

[63] R. Al Hasnawi and I. Marghescu, "A Survey of Vehicular VLC Methodologies," *Sensors*, vol. 24, no. 2, p. 598, 2024.

[64] A. Memedi and F. Dressler, "Vehicular Visible Light Communications: A Survey," *IEEE Communications Surveys & Tutorials*, vol. 23, no. 1, pp. 161–181, 2020.

[65] R. Murai, T. Sakai, H. Kawano, Y. Matsukawa, Y. Kitano, Y. Honda, and K. C. Campbell, "A novel visible light communication system for enhanced control of autonomous delivery robots in a hospital," in *2012 IEEE/SICE International Symposium on System Integration (SII)*, pp. 510–516, IEEE, 2012.

[66] H. Kurunathan, R. Indhumathi, M. G. Gaitán, C. Taramasco, and E. Tovar, "Vlc-enabled monitoring in a healthcare setting: Overview and challenges," in *2023 South American Conference On Visible Light Communications (SACVLC)*, pp. 135–140, IEEE, 2023.

[67] M. P. Bhadoria, G. Pandey, and A. Dixit, "Performance Evaluation of Visible Light Communication for DCO and ACO Optical OFDM Techniques," in *2019 National conference on communications (NCC)*, pp. 1–6, IEEE, 2019.

[68] F. Zafar, D. Karunatilaka, and R. Parthiban, "Dimming Schemes for Visible Light Communication: The State of Research," *IEEE Wireless Communications*, vol. 22, no. 2, pp. 29–35, 2015.

[69] F. Zafar, M. Bakaul, and R. Parthiban, "Laser-Diode-Based Visible Light Communication: Toward Gigabit Class Communication," *IEEE Communications Magazine*, vol. 55, no. 2, pp. 144–151, 2017.

[70] H. Zimmermann, "APD and SPAD receivers," in *2019 15th International Conference on Telecommunications (ConTEL)*, pp. 1–5, IEEE, 2019.

[71] Z. Ghassemlooy, W. Popoola, and S. Rajbhandari, *Optical wireless communications: system and channel modelling with Matlab®*. CRC press, 2019.

[72] T. Z. Gutema, H. Haas, and W. O. Popoola, "Bias Point Optimisation in LiFi for Capacity Enhancement," *Journal of Lightwave Technology*, vol. 39, no. 15, pp. 5021–5027, 2021.

[73] L. Zeng, D. C. O'Brien, H. Le Minh, G. E. Faulkner, K. Lee, D. Jung, Y. Oh, and E. T. Won, "High data rate multiple input multiple output (MIMO) optical wireless communications using white LED lighting," *IEEE Journal on Selected Areas in Communications*, vol. 27, no. 9, pp. 1654–1662, 2009.

[74] S. Chatterjee, D. Sabui, G. S. Khan, and B. Roy, "Signal to interference plus noise ratio improvement of a multi-cell indoor visible light communication system through optimal parameter selection complying lighting constraints," *Transactions on Emerging Telecommunications Technologies*, vol. 32, no. 10, p. e4291, 2021.

[75] T. Komine and M. Nakagawa, "Fundamental Analysis for Visible-Light Communication System using LED lights," *IEEE transactions on Consumer Electronics*, vol. 50, no. 1, pp. 100–107, 2004.

[76] T. Fath and H. Haas, "Performance Comparison of MIMO Techniques for Optical Wireless Communications in Indoor Environments," *IEEE Transactions on Communications*, vol. 61, no. 2, pp. 733–742, 2012.

[77] A. Burton, Z. Ghassemlooy, S. Rajbhandari, and S.-K. Liaw, "Design and analysis of an angular-segmented full-mobility visible light communications receiver," *Transactions on Emerging Telecommunications Technologies*, vol. 25, no. 6, pp. 591–599, 2014.

[78] A. Burton, H. Le Minh, Z. Ghassemlooy, S. Rajbhandari, and P. A. Haigh, "Performance Analysis for 180 Receiver in Visible Light Communications," in *2012 Fourth International Conference on Communications and Electronics (ICCE)*, pp. 48–53, IEEE, 2012.

[79] A. Burton, H. Le Minh, Z. Ghassemlooy, S. Rajbhandari, and P. A. Haigh, "Smart Receiver for Visible Light Communications: Design and Analysis," in *2012 8th International Symposium on Communication Systems, Networks & Digital Signal Processing (CSNDSP)*, pp. 1–5, IEEE, 2012.

[80] L. Rodrigues, M. Figueiredo, L. N. Alves, and Z. Ghassemlooy, "VLC frontends for IoT applications," in *2022 4th West Asian Symposium on Optical and Millimeter-wave Wireless Communications (WASOWC)*, pp. 1–6, IEEE, 2022.

[81] M. A. S. Sejan and W.-Y. Chung, "Indoor Fine Particulate Matter Monitoring in a Large Area Using Bidirectional Multihop VLC," *IEEE Internet of Things Journal*, vol. 8, no. 9, pp. 7214–7228, 2020.

[82] M. A. S. Sejan and W.-Y. Chung, "Secure VLC for Wide-Area Indoor IoT Connectivity," *IEEE Internet of Things Journal*, vol. 10, no. 1, pp. 180–193, 2022.

[83] P. Namonta and P. Cherntanomwong, "The improvement of Repeater System for Visible Light Communication," in *2016 13th International Conference on Electrical Engineering/Electronics, Computer, Telecommunications and Information Technology (ECTICON)*, pp. 1–6, IEEE, 2016.

[84] A. Gupta, V. Singh, M. Gautam, and A. Dixit, "Design and implementation for a duplex visible light communication link," in *2022 14th International Conference on COMmunication Systems & NETworkS (COMSNETS)*, pp. 190–193, IEEE, 2022.

[85] B. G. Guzman, M. S. Mir, D. F. Fonseca, A. Galisteo, Q. Wang, and D. Giustiniano, "Prototyping Visible Light Communication for the Internet of Things Using OpenVLC," *IEEE Communications Magazine*, vol. 61, no. 5, pp. 122–128, 2023.

[86] L. Klaver and M. Zuniga, "Shine: A step towards distributed multi-hop visible light communication," in *2015 IEEE 12th International Conference on Mobile Ad Hoc and Sensor Systems*, pp. 235–243, IEEE, 2015.

[87] A. Pradana, N. Ahmadi, T. Adiono, W. A. Cahyadi, and Y.-H. Chung, "VLC Physical Layer Design based on Pulse Position Modulation (PPM) for Stable Illumination," in

2015 international symposium on intelligent signal processing and communication systems (ISPACS), pp. 368–373, IEEE, 2015.

[88] A. Tahmasi, H. Hematkhah, and Y. S. Kavian, "Visible Light Communication Based Optical Link for Data Transmission in Wireless Sensor Networks," in *2016 10th international symposium on communication systems, networks and digital signal processing (CSNDSP)*, pp. 1–6, IEEE, 2016.

[89] C.-W. Chen, W.-C. Wang, J.-T. Wu, H.-Y. Chen, K. Liang, L.-Y. Wei, Y. Hsu, C.-W. Hsu, C.-W. Chow, C.-H. Yeh, *et al.*, "Visible light communications for the implementation of internet-of-things," *Optical Engineering*, vol. 55, no. 6, pp. 060501–060501, 2016.

[90] D. K. Tettey, M. Elamassie, and M. Uysal, "Experimental Investigation of Angle Diversity Receiver for Vehicular VLC," in *Proceedings of the 29th Annual International Conference on Mobile Computing and Networking*, pp. 1–3, 2023.

[91] I. Soto, R. Nilson Rodrigues, G. Massuyama, F. Seguel, P. Palacios Jativa, C. A. Azurdia-Meza, and N. Krommenacker, "A hybrid VLC-RF portable phasor measurement unit for deep tunnels," *Sensors*, vol. 20, no. 3, p. 790, 2020.

[92] A. Madahian, P. A. Ardakani, J. Abouei, A. Mirvakili, A. Mohammadi, and V. Koomson, "A Hybrid VLC/RF Parking Automation System," *IEEE Access*, 2023.

[93] Y. S. M. Pratama and K. W. Choi, "Bandwidth aggregation protocol and throughput-optimal scheduler for hybrid RF and visible light communication systems," *IEEE Access*, vol. 6, pp. 32173–32187, 2018.

[94] Z. Li, S. Shao, A. Khreishah, M. Ayyash, I. Abdalla, H. Elgala, M. Rahaim, and T. Little, "Design and implementation of a hybrid RF-VLC system with bandwidth aggregation," in *2018 14th International Wireless Communications & Mobile Computing Conference (IWCMC)*, pp. 194–200, IEEE, 2018.

[95] A. Tang, C. Xu, B. Zhai, and X. Wang, "Design and implementation of an integrated visible light communication and wifi system," in *2018 IEEE 15th International Conference on Mobile Ad Hoc and Sensor Systems (MASS)*, pp. 157–165, IEEE, 2018.

[96] A. Scheianu, G. Suciu, A. Drosu, I. Petre, and D. Miu, "Hybrid VLC Communications system for increased security based on Raspberry Pi microcomputer," *Annals of Disaster Risk Sciences: ADRS*, vol. 3, no. 1, pp. 0–0, 2020.

[97] S. Naribole, S. Chen, E. Heng, and E. Knightly, "LiRa: A WLAN architecture for visible light communication with a Wi-Fi uplink," in *2017 14th Annual IEEE International Conference on Sensing, Communication, and Networking (SECON)*, pp. 1–9, IEEE, 2017.

[98] E. Zadobrischi, "System prototype proposed for vehicle communications based on VLC-RF technologies adaptable on infrastructure," in *2020 International Conference on Development and Application Systems (DAS)*, pp. 78–83, IEEE, 2020.

[99] K. T. Ngo, S. Mangione, and I. Tinnirello, "Ai-enhanced vlc/rf hybrid for smart iot: A revolution," in *2024 International Conference on Advanced Technologies for Communications (ATC)*, pp. 986–991, IEEE, 2024.

[100] P. Du, S. Zhang, A. Alphones, and C. Chen, "Faster Deployment for Indoor Visible Light Positioning Using Xgboost Algorithms in Industrial Internet-of-Things," in *IECON 2021–47th Annual Conference of the IEEE Industrial Electronics Society*, pp. 1–7, IEEE, 2021.

[101] C. Beguni, A. Done, A.-M. Căilean, S.-A. Avătămăniței, and E. Zadobrischi, "Experimental Demonstration of a Visible Light Communications System Based on Binary Frequency-Shift Keying Modulation: A New Step toward Improved Noise Resilience," *Sensors*, vol. 23, no. 11, p. 5001, 2023.

[102] S. Caputo, L. Mucchi, M. A. Umair, M. Meucci, M. Seminara, and J. Catani, "The Role of Bidirectional VLC Systems in Low-Latency 6G Vehicular Networks and Comparison with IEEE802. 11p and LTE/5G C-V2X," *Sensors*, vol. 22, no. 22, p. 8618, 2022.

[103] L. Shi, W. Li, X. Zhang, Y. Zhang, G. Chen, and A. Vladimirescu, "Experimental 5G new radio integration with VLC," in *2018 25th IEEE International Conference on Electronics, Circuits and Systems (ICECS)*, pp. 61–64, IEEE, 2018.

[104] Y. Hong, T. Wu, and L.-K. Chen, "On the Performance of Adaptive MIMO-OFDM Indoor Visible Light Communications," *IEEE Photonics Technology Letters*, vol. 28, no. 8, pp. 907–910, 2016.

[105] J. An, Q. N. Pham, and W.-Y. Chung, "Single cell three-channel wavelength division multiplexing in visible light communication," *Optics Express*, vol. 25, no. 21, pp. 25477–25485, 2017.

[106] H. Sifaou, K.-H. Park, A. Kammoun, and M.-S. Alouini, "Optimal linear precoding for indoor visible light communication system," in *2017 IEEE International Conference on Communications (ICC)*, pp. 1–5, IEEE, 2017.

[107] P. Palacios Játiva, M. Román Canizares, C. A. Azurdia-Meza, D. Zabala-Blanco, A. Dehghan Firoozabadi, F. Seguel, S. Montejo-Sánchez, and I. Soto, "Interference Mitigation for Visible Light Communications in Underground Mines Using Angle Diversity Receivers," *Sensors*, vol. 20, no. 2, p. 367, 2020.

[108] D. Sabui, S. Chatterjee, and G. S. Khan, "Multi-cell VLC System and Reconfigurable Intelligent Surfaces: Connecting the dots," in *2024 IEEE 3rd International Conference on Control, Instrumentation, Energy & Communication (CIEC)*, pp. 135–140, IEEE, 2024.

[109] C. Chen, D. Tsonev, and H. Haas, "Joint transmission in indoor visible light communication downlink cellular networks," in *2013 IEEE Globecom Workshops (GC Wkshps)*, pp. 1127–1132, IEEE, 2013.

[110] C. Chen, S. Videv, D. Tsonev, and H. Haas, "Fractional Frequency Reuse in DCO-OFDM-Based Optical Attocell Networks," *Journal of Lightwave Technology*, vol. 33, no. 19, pp. 3986–4000, 2015.

[111] S.-Y. Jung, D.-H. Kwon, S.-H. Yang, and S.-K. Han, "Inter-cell interference mitigation in multi-cellular visible light communications," *Optics Express*, vol. 24, no. 8, pp. 8512–8526, 2016.

[112] K. Bera and N. Karmakar, "Interference Mitigation in VLC Systems using a Variable Focus Liquid Lens," in *Photonics*, vol. 11, p. 506, MDPI, 2024.

[113] C. Chen, P. Du, H. Yang, W.-D. Zhong, X. Deng, and Y. Yang, "Demonstration of Inter-cell Interference Mitigation in Multi-cell VLC Systems Using Optimized Angle Diversity Receiver," in *2019 IEEE 4th Optoelectronics Global Conference (OGC)*, pp. 36–39, IEEE, 2019.

[114] M. Obeed, H. Dahrouj, A. M. Salhab, A. Chaaban, S. A. Zummo, and M.-S. Alouini, "Power Allocation and Link Selection for Multicell Cooperative NOMA Hybrid VLC/RF Systems," *IEEE Communications Letters*, vol. 25, no. 2, pp. 560–564, 2020.

[115] M. S. Demir, F. Miramirkhani, and M. Uysal, "Handover in VLC networks with coordinated multipoint transmission," in *2017 IEEE International Black Sea Conference on Communications and Networking (BlackSeaCom)*, pp. 1–5, IEEE, 2017.

[116] K. W. Palitharathna, A. M. Vegni, P. D. Diamantoulakis, H. A. Suraweera, and I. Krikidis, "Handover Management through Reconfigurable Intelligent Surfaces for VLC under Blockage Conditions," in *2024 IEEE International Symposium on Circuits and Systems (ISCAS)*, pp. 1–5, IEEE, 2024.

[117] M. Morales-Céspedes, M. Biagi, and A. G. Armada, "On the Need for Angular Diversity Receivers in Spatial MIMO Visible Light Communications," in *GLOBECOM 2024-2024 IEEE Global Communications Conference*, pp. 331–336, IEEE, 2024.

[118] A. G. A. Al-Sakkaf and M. Morales-Céspedes, "Interference Management for VLC Indoor Systems based on Overlapping Field-of-View Angle Diversity Receivers," *IEEE Access*, 2024.

[119] K. Mekonnen and G. Gelinck, "Modified angle diversity receiver with wide field-of-view for short-range high-speed optical wireless communication," in *ECOC 2024; 50th European Conference on Optical Communication*, pp. 471–474, VDE, 2024.

[120] B. G. Guzman, M. Morales-Cespedes, A. G. Armada, and M. Brandt-Pearce, "Angle diversity receiver as a key enabler for reliable ORIS-based Visible Light Communication," *arXiv preprint arXiv:2505.10129*, 2025.

[121] Z. Zeng, C. Chen, X. Wu, S. Savović, M. D. Soltani, M. Safari, and H. Haas, "Interference mitigation using optimised angle diversity receiver in LiFi cellular network," *Optics Communications*, vol. 574, p. 131125, 2025.

[122] P. Deng and M. Kavehrad, "Adaptive Real-Time Software Defined MIMO Visible Light Communications using Spatial Multiplexing and Spatial Diversity," in *2016 IEEE International Conference on Wireless for Space and Extreme Environments (WiSEE)*, pp. 111–116, IEEE, 2016.

[123] E. S. Hassan, A. Jabbari, and A. A. Alharbi, "Evaluating MIMO-VLC System Performance: Modulation Techniques and Ambient Light Interference Effects," in *Photonics*, vol. 12, p. 649, MDPI, 2025.

[124] J. Lian and M. Brandt-Pearce, "Multiuser MIMO Indoor Visible Light Communication System Using Spatial Multiplexing," *Journal of Lightwave Technology*, vol. 35, no. 23, pp. 5024–5033, 2017.

[125] C. Chen, I. Tavakkolnia, M. D. Soltani, M. Safari, and H. Haas, "Hybrid multiplexing in OFDM-based VLC systems," in *2020 IEEE Wireless Communications and Networking Conference (WCNC)*, pp. 1–6, IEEE, 2020.

[126] C. Chen, Y. Wei, H. Zhang, Z. Zhuang, Z. Li, C. Shen, J. Zhang, H. Cai, N. Chi, and J. Shi, "Spatial Multiplexing Holography for Multi-User Visible Light Communication," in *Photonics*, vol. 12, p. 160, MDPI, 2025.

[127] L. Deng and Y. Fan, "Analysis of channel correlation and channel capacity for indoor MIMO visible light communication systems," *Applied Optics*, vol. 59, no. 15, pp. 4672–4684, 2020.

[128] R. Wang, Q. Gao, J. You, E. Liu, P. Wang, Z. Xu, and Y. Hua, "Linear Transceiver Designs for MIMO Indoor Visible Light Communications Under Lighting Constraints," *IEEE Transactions on Communications*, vol. 65, no. 6, pp. 2494–2508, 2017.

[129] S. H. Younus, A. A. Al-Hameed, A. T. Hussein, M. T. Alresheedi, and J. M. Elmirghani, "Parallel Data Transmission in Indoor Visible Light Communication Systems," *IEEE Access*, vol. 7, pp. 1126–1138, 2018.

[130] Y. S. Hussein, M. Y. Alias, and A. A. Abdulkafi, "On Performance Analysis of LS and MMSE for Channel Estimation in VLC systems," in *2016 IEEE 12th International Colloquium on Signal Processing & Its Applications (CSPA)*, pp. 204–209, IEEE, 2016.

[131] T. Brown, P. Kyritsi, and E. De Carvalho, *Practical guide to MIMO radio channel: With MATLAB examples*. John Wiley & Sons, 2012.

[132] Y. S. Cho, J. Kim, W. Y. Yang, and C. G. Kang, *MIMO-OFDM wireless communications with MATLAB*. John Wiley & Sons, 2010.

[133] Y. Celik and A. Akan, "Subcarrier intensity modulation for MIMO visible light communications," *Optics Communications*, vol. 412, pp. 90–101, 2018.

[134] P. P. Játiva, C. A. Azurdia-Meza, M. R. Cañizares, S. Céspedes, and S. Montejo-Sánchez, "Performance enhancement of VLC-based systems using diversity combining schemes in the receiver," in *2019 IEEE Latin-American Conference on Communications (LATINCOM)*, pp. 1–6, IEEE, 2019.

[135] M. Román Cañizares, C. Azurdia-Meza, P. Palacios Játiva, D. Zabala-Blanco, and I. Sánchez, "Intelligent Reflective Surface-Assisted Visible Light Communication with Angle Diversity Receivers and RNN: Optimizing Non-Line-of-Sight Indoor Environments," *Applied Sciences*, vol. 15, no. 3, p. 1617, 2025.

[136] A. Gupta and P. Garg, "Statistics of SNR for an Indoor VLC system and Its Applications in System Performance," *IEEE Communications Letters*, vol. 22, no. 9, pp. 1898–1901, 2018.

[137] J. Liu, F. Yang, N. An, J. Song, and Z. Han, "VLC-enabled UAV Network for IoT with Co-channel Interference: Joint Spatial Deployment and Resource Allocation," *IEEE Internet of Things Journal*, 2025.

[138] Q. Zhao, J. Fan, B. Lin, and C. Chen, "A Quantized CSI Acquisition Strategy Based on Position Information Feedback for Indoor VLC-Based IoT Systems," *IEEE Internet of Things Journal*, 2025.

[139] V. Dixit, A. Kumar, N. Sharan, S. Pandey, A. Kumar, and R. S. Singh, "Optimizing intelligent reflecting surface assisted visible light communication networks under blockage and practical constraints using TLBO for IoT applications," *Scientific Reports*, vol. 15, no. 1, p. 27400, 2025.

[140] A. A. Batista, T. D. Amorim, R. M. Ribeiro, A. P. Barbero, R. B. Di Renna, F. C. Peixoto, and V. N. Silva, "Enhanced Photodetector Field of View for IoT-Driven VLC Systems Using Fluorescent Optical Antennas," *IEEE Access*, 2025.

[141] C. G. Gavrincea, J. Baranda, and P. Henarejos, "Rapid Prototyping of Standard Compliant Visible Light Communications System," *IEEE Communications Magazine*, vol. 52, no. 7, pp. 80–87, 2014.

[142] N. Ashokkumar, P. V. Haritha, P. Eswar, P. V. S. K. Kumar, S. B. Prakash, and M. Raghunath, "IOT-Enabled VLC Industry Automation System: Harnessing Node MCU Microcontroller for Streamlined Control and Communication," in *2024 International Conference on Intelligent Systems for Cybersecurity (ISCS)*, pp. 1–6, IEEE, 2024.

[143] P. Nabavi and M. Yuksel, "Comprehensive Design and Prototype of VLC Receivers With Large Detection Areas," *Journal of Lightwave Technology*, vol. 38, no. 16, pp. 4187–4204, 2020.

[144] P. Nabavi and M. Yuksel, "Conformal VLC Receivers with Photodetector Arrays: Design, Analysis and Prototype," in *ICC 2019-2019 IEEE International Conference on Communications (ICC)*, pp. 1–7, IEEE, 2019.

[145] R. Harada, "Supplementary materials for Study, Design and Implementation of VLC with Angular Diversity Receiver for IoT Systems." Available at: `https://dx.doi.org/10.21227/gsmd-x105`, 2024.

[146] A. H. F. Raouf, C. K. Anjinappa, and I. Guvenc, "Designing Hybrid VLC-RF Networks with Random Receiver Orientation and Energy Harvesting," *Authorea Preprints*, 2023.

[147] D. A. Basnayaka and H. Haas, "Hybrid RF and VLC systems: Improving user data rate performance of VLC systems," in *2015 IEEE 81st vehicular technology conference (VTC Spring)*, pp. 1–5, IEEE, 2015.

[148] A. Khreishah, S. Shao, A. Gharaibeh, M. Ayyash, H. Elgala, and N. Ansari, "A Hybrid RF-VLC System for Energy Efficient Wireless Access," *IEEE Transactions on Green Communications and Networking*, vol. 2, no. 4, pp. 932–944, 2018.

[149] I.-P. Hong, G. N. Tran, *et al.*, "SLIPT-Assisted Dual-Hop VLC/RF With Relay Selection: Outage Probability Analysis and Optimization," *IEEE Access*, vol. 13, pp. 41854–41864, 2025.

[150] A. M. El-Eraki, N. Alshaer, M. Fouad, A. A. Hamdi, and T. Ismail, "Integrated VLC/RF With Adaptive Power Control for Reliable Cluster-Based VANET Communications," *IEEE Access*, 2025.

[151] F. Wang, F. Yang, C. Pan, J. Song, and Z. Han, "Hybrid VLC-RF systems with multi-users for achievable rate and energy efficiency maximization," *IEEE Transactions on Wireless Communications*, vol. 22, no. 9, pp. 6157–6170, 2023.

[152] M. Khadmaoui-Bichouna, A. M. Escolar, J. M. Alcaraz-Calero, and Q. Wang, "Design and implementation of an integrated OWC and RF network slicing-based architecture over hybrid LiFi and 5G networks," *Wireless Networks*, vol. 31, no. 2, pp. 1541–1559, 2025.

[153] F. Delgado-Rajo, A. Melian-Segura, V. Guerra, R. Perez-Jimenez, and D. Sanchez-Rodriguez, "Hybrid RF/VLC Network Architecture for the Internet of Things," *Sensors*, vol. 20, no. 2, p. 478, 2020.

[154] T. P. V. Andrade, C. H. d. S. Lopes, L. Carneiro de Souza, and A. C. Sodré Junior, "Demonstration of a Hybrid B5G System Integrating VLC and RF-Based Technologies with Access Networks," *Applied Sciences*, vol. 15, no. 2, p. 955, 2025.

[155] D. Iturralde, J. Guaña-Moya, P. P. Játiva, I. Sánchez, M. Ijaz, A. Dehghan Firoozabadi, and D. Zabala-Blanco, "A New Internet of Things Hybrid VLC/RF System for m-Health in an Underground Mining Industry," *Sensors*, vol. 24, no. 1, p. 31, 2023.

[156] R. Harada, "Supplementary materials for Integrated VLC-RF System with Angular Diversity Receiver for Robust Industrial IoT Applications." Available at: `https://dx.doi.org/10.21227/fg8r-fd09`, 2024.

[157] Ö. Cepheli and G. K. Kurt, "Physical layer security in wireless communication networks," in *Security, Privacy, Trust, and Resource Management in Mobile and Wireless Communications*, pp. 61–81, IGI Global Scientific Publishing, 2014.

[158] A. Sanenga, G. A. Mapunda, T. M. L. Jacob, L. Marata, B. Basutli, and J. M. Chuma, "An overview of key technologies in physical layer security," *Entropy*, vol. 22, no. 11, p. 1261, 2020.

[159] R. A. Fisher and F. Yates, *Statistical tables for biological, agricultural and medical research*. Hafner Publishing Company, 1953.

[160] R. Bian, I. Tavakkolnia, and H. Haas, "15.73 Gb/s Visible Light Communication with off-the-shelf LEDs," *Journal of Lightwave Technology*, vol. 37, no. 10, pp. 2418–2424, 2019.

[161] T. Lu, Y. Dai, T.-Y. Lee, S. Wang, W. Guo, S. Lai, Z. Chen, H.-C. Kuo, and T. Wu, "Experimental investigation of high-speed WDM-visible light communication using blue, green, and red InGaN μLEDs," *Optics Letters*, vol. 49, no. 16, pp. 4697–4700, 2024.

[162] C. He, Y. Tang, C. Chen, and H. Fu, "Wavelength Division Multiplexing in Visible Light Communications Using Fluorescent Fiber Antennas," *Journal of Lightwave Technology*, vol. 42, no. 10, pp. 3725–3735, 2024.

[163] L. Cui, Y. Tang, H. Jia, J. Luo, and B. Gnade, "Analysis of the Multichannel WDM-VLC Communication System," *Journal of lightwave Technology*, vol. 34, no. 24, pp. 5627–5634, 2016.

[164] S. H. Younus and J. M. Elmirghani, "WDM for High-Speed Indoor Visible Light Communication System," in *2017 19th International Conference on Transparent Optical Networks (ICTON)*, pp. 1–6, IEEE, 2017.

[165] O. Z. Aletri, T. El-Gorashi, and J. M. Elmirghani, "Resource Allocation in 6G Optical Wireless Systems," in *6G Mobile Wireless Networks*, pp. 187–206, Springer, 2021.

[166] J. H. T. Sia, M. C. C. Kho, K. U. Hii, and L. Yong, "Design and Investigation of RGB-type LED Visible Light Communication System," *International Journal of Integrated Engineering*, vol. 13, no. 2, pp. 136–145, 2021.

[167] OSRAM, "LED LZ4-00MD09 Datasheet." Available at: `https://look.ams-osram.com/m/2e0d290230c68ad4/original/LZ4-00MD09.pdf`. Accessed 01-June-2025.

[168] Rohm, "MOSFET N-CH 60V 2A 2SK3065 Datasheet." Available at: `https://mm.digikey.com/Volume0/opasdata/d220001/medias/docus/859/2sk3065.pdf`. Accessed 08-August-2025.

[169] HAMAMATSU, "Si photodiode S9032-02 RGB color sensor Datasheet." Available at: `https://www.hamamatsu.com/content/dam/hamamatsu-photonics/sites/documents/99_SALES_LIBRARY/ssd/s9032-02_kspd1067e.pdf`. Accessed 01-June-2025.